



2003

ANALYSIS OF HYDRODYNAMIC EFFECTS OF MICROASPERITY SHAPES ON THRUST BEARING SURFACES

Ravinder Babu Siripuram
University of Kentucky, ravi@engr.uky.edu

[Right click to open a feedback form in a new tab to let us know how this document benefits you.](#)

Recommended Citation

Siripuram, Ravinder Babu, "ANALYSIS OF HYDRODYNAMIC EFFECTS OF MICROASPERITY SHAPES ON THRUST BEARING SURFACES" (2003). *University of Kentucky Master's Theses*. 309.
https://uknowledge.uky.edu/gradschool_theses/309

This Thesis is brought to you for free and open access by the Graduate School at UKnowledge. It has been accepted for inclusion in University of Kentucky Master's Theses by an authorized administrator of UKnowledge. For more information, please contact UKnowledge@lsv.uky.edu.

ABSTRACT OF THESIS

ANALYSIS OF HYDRODYNAMIC EFFECTS OF MICROASPERITY SHAPES ON THRUST BEARING SURFACES

The present thesis is a comparative study of the hydrodynamic effects of a few deterministic microasperity shapes in a thrust slider application. Numerical study based on finite difference methods is used to find the trend of important tribological properties such as friction and leakage. Also, this work utilizes a distinctive and practical approach for comparison by considering constant load conditions, instead of constant film thickness, as is expected in an operating thrust bearing.

The results are encouraging and clearly reveal the existence of a transition point for asperity area fraction where a reversal in trends for both the coefficient of friction and leakage is observed. The shapes of asperities affect leakage but, have a negligible effect on coefficient of friction; however, the size and the type of asperity (positive or negative) do influence it. The effects of orientation, on the other hand, are found both on the coefficient of friction and leakage. Triangular asperities exhibit an advantage over the other shapes in terms of leakage. In general, the impact of shapes is distinguishable, more at higher asperity area fractions in accordance with the geometrical differences.

KEYWORDS: Microasperity, Lubrication, Hydrodynamics, Tribology, Thrust bearing

Ravinder Babu Siripuram

August 6, 2003

ANALYSIS OF HYDRODYNAMIC EFFECTS OF MICROASPERITY SHAPES ON
THRUST BEARING SURFACES

By

Ravinder Babu Siripuram

Dr. L.S.Stephens

Director of Thesis

Dr.George Huang

Director of Graduate Studies

August 6, 2003

RULES FOR THE USE OF THESES

Unpublished theses submitted for the Master's degree and deposited in the University of Kentucky Library are a rule open for inspection, but are to be used only with due regard to the rights of the authors. Bibliographical references may be noted, but quotations or summaries of parts may be published only with the permission of the author, and with the usual scholarly acknowledgements.

Extensive copying or publication of the theses in whole or in part also requires the consent of the Dean of the Graduate School of the University of Kentucky.

A library that borrows this thesis for use by its patrons is expected to secure the signature of each user.

Name

Date

THESIS

Ravinder Babu Siripuram

The Graduate School

University of Kentucky

2003

ANALYSIS OF HYDRODYNAMIC EFFECTS OF MICROASPERITY SHAPES ON
THRUST BEARING SURFACES

THESIS

A thesis submitted in partial fulfillment of the
requirements for the degree of Master of Science in Mechanical Engineering in the
College of Engineering at the University of Kentucky

By

Ravinder Babu Siripuram

Lexington, Kentucky

Director: Dr. L.S. Stephens, Associate Professor of Mechanical Engineering

Lexington, Kentucky

2003

MASTER'S THESIS RELEASE

I authorize the University of Kentucky
Libraries to reproduce this thesis in
whole or in part for purposes of research.

Signed: Ravinder Babu Siripuram

Date: August 6, 2003

ACKNOWLEDGEMENTS

At the outset, I would like to thank DARPA (Defense Advanced Research Projects Agency) and NSF (National Science Foundation) Surface Engineering and Materials Design Program, Award No.CMS-0201445, for sponsoring electro fabrication project and my present research work respectively. Also, I thank University of Kentucky for providing an excellent and conducive environment for my work and for my stay.

This study would not have been possible without the invaluable freedom given to me by Dr. Lyndon S. Stephens, the Director of this thesis. Also, I sincerely thank him for placing confidence in me while assigning this analytical work, following the successful setting up of micro fabrication lab in our Department of Mechanical Engineering. In addition, his active interest and encouragement in exploring alternative solution methods has always been rewarding and helpful in finding the advantages and limitations of such methods and software used for microasperity lubrication. His presentation skills are commendable and exacting. They served as guiding factors in writing my thesis.

Dr. Keith E. Rouch with his exceptional knowledge and expertise, particularly in ANSYS[®], was an ever accessible in-house resource for me. I am also extremely thankful to him for his magnanimity in letting me use his computing resources unconditionally. I am indebted to Dr. James M. McDonough for providing me insights whenever I experienced computational difficulties, even at the cost of his own valuable time. I am glad that both of them have agreed to be on my thesis committee.

I am fortunate to have encouraging parents and a wonderful wife, Manjula Siripuram, for their unwavering support through out the thesis period. Finally, I thank all my lab mates and the office staff in the Mechanical Engineering Department for their cooperation. It would sure be gratifying to me if new researchers at Bearings and Seals lab refer to my thesis, for obtaining an overview of the lab work, without having to scramble for information.

Table of Contents

ACKNOWLEDGEMENTS	III
LIST OF TABLES	VIII
LIST OF FIGURES	IX
LIST OF FILES	XI
CHAPTER I: INTRODUCTION	1
1.1 BACKGROUND	1
1.2 RELATED AND EARLIER RESEARCH	2
1.3 THESIS OVERVIEW	5
1.4 TARGET APPLICATION.....	8
CHAPTER II: BASIC CONCEPTS.....	10
2.1 SURFACE TOPOGRAPHY	10
2.2 ACTUAL AND MODEL SURFACES.....	11
2.3 FRICTION.....	12
2.4 WEAR	14
2.4.1 ADHESION	14
2.4.2 ABRASION	15
2.5 CONTACT MECHANICS.....	15
2.6 SURFACE CONTAMINANTS	15
2.7 TRANSFER LAYERS.....	16
2.8 LUBRICATION	16
CHAPTER III: MICROFABRICATION	19
3.1 DETERMINISTIC ASPERITIES.....	19
3.2 MICROFABRICATION PROCESSES.....	19
3.2.1 PHOTOETCHING	19

3.2.2 LIGA (MODIFIED)	20
3.2.3 LASER ABLATION.....	21
3.2.4 UV PHOTOLITHOGRAPHY.....	21
3.3 SURFACE FINISHING	22
3.3.1 LAPPING.....	22
3.3.2 POLISHING.....	22
3.4 METROLOGY.....	22
3.4.1 OPTICAL MICROSCOPE	22
3.4.2 ELECTRON MICROSCOPE.....	23
3.4.3 OPTICAL INTERFEROMETER.....	23
CHAPTER IV: MODELING	24
4.1 INTRODUCTION.....	24
4.1.1 HYDRODYNAMIC THEORY.....	24
4.1.2 VELOCITY DISTRIBUTION.....	25
4.1.3 STEADY STATE REYNOLDS EQUATION.....	26
4.1.4 MICROASPERITY LUBRICATION.....	27
4.1.5 CAVITATION.....	28
4.1.6 MECHANISMS OF HYDRODYNAMIC LOAD SUPPORT	29
4.1.6.1 Smooth Surfaces	29
4.1.6.2 Rough Surfaces.....	29
4.1.6.3 Spiral Grooves.....	30
4.1.6.4 Radial Grooves.....	31
4.1.6.6 Macro Roughness.....	31
4.1.6.7 Temperature effects.....	31
4.1.6.8 Miscellaneous Effects.....	31
4.2 ANALYTICAL SOLUTIONS	31
4.2.1 ONE DIMENSIONAL STEP SLIDER SOLUTION	32
4.2.1.1 Positive Step Slider.....	32
4.2.1.2 Negative Step Slider	33
4.2.2 BOUNDARY CONDITIONS.....	34
4.2.2.1 Full Sommerfeld.....	34
4.2.2.2 Half Sommerfeld.....	35
4.2.2.3 Reynolds Condition	36
4.2.3 TWO DIMENSIONAL MODELS	37
4.2.4 ARRAYS, GEOMETRIES AND ORIENTATION	37
4.2.5 SOLUTION TO A TWO DIMENSIONAL MODEL.....	38
4.2.6 COEFFICIENT OF FRICTION	41
4.2.7 LEAKAGE (BASED ON POISEUILLE FLOW).....	42
4.3 NUMERICAL SOLUTIONS	43
4.3.1 FINITE DIFFERENCE EQUATIONS	43
4.3.2 SOLUTION METHOD	45

4.3.3 REYNOLDS CAVITATION CONDITION	47
4.3.4 NEGATIVE ASPERITY MODEL.....	47
4.3.5 FLOW CHART FOR A NUMERICAL SOLUTION.....	48
4.3.6 RADIAL DISTRIBUTION MODEL.....	50
4.3.7 MODEL MATRIX.....	51
CHAPTER V: RESULTS AND DISCUSSION.....	53
5.1 VARIABLES AFFECTING LOAD SUPPORT	53
5.1.1 SPEED.....	53
5.1.2 NUMBER OF ASPERITIES.....	54
5.1.3 ASPERITY RADIUS.....	55
5.1.4 ASPERITY AREA FRACTION.....	55
5.1.5 ASPERITY HEIGHT.....	56
5.1.6 FILM THICKNESS.....	57
5.2 ANALYSIS WITH ANSYS®.....	58
5.3 EVEN AND STAGGERED GRIDS IN F.D. METHOD.....	59
5.4 BENCHMARKING	61
5.5 RESULTS FROM THE RADIAL MODEL.....	63
5.6 BASIS FOR COMPARING DIFFERENT SHAPES	65
5.7 RESULTS	66
5.7.1 PRESSURE DISTRIBUTION	66
5.7.2 COEFFICIENT OF FRICTION.....	69
5.7.2.1 <i>Square Asperity</i>	70
5.7.2.2 <i>Different Geometries</i>	71
5.7.2.3 <i>Orientation effects</i>	73
5.7.3 FILM THICKNESS	75
5.7.3.1 <i>Square asperity</i>	75
5.7.3.2 <i>All cases</i>	76
5.7.4 LEAKAGE (POISEUILLE FLOW).....	77
5.7.4.1 <i>Square Asperity</i>	77
5.7.4.2 <i>Different Geometries</i>	78
5.7.4.3 <i>Orientation Effects</i>	79
5.8 RESULTS (WITH HYDROSTATIC PRESSURE B/C):.....	81
5.9 CONTINUITY OF FLOW.....	84
CHAPTER VI: SUMMARY, CONCLUSION AND FUTURE WORK	86
6.1 SUMMARY.....	86
6.2 CONCLUSION	87

6.3 FUTURE WORK.....	88
APPENDIX.....	89
A.1 NOMENCLATURE.....	89
A.2 MATLAB® SCRIPT FILES.....	90
A.2.1 FILM THICKNESS MODELS.....	90
<i>A.2.1.1 Hexagonal Model.....</i>	<i>90</i>
<i>A.2.1.2 Triangular Model.....</i>	<i>91</i>
<i>A.2.1.3 Radial Model.....</i>	<i>92</i>
A.2.2 ANALYTICAL 1-D STEP SLIDER SOLUTION.....	93
A.2.3 NUMERICAL 1-D POSITIVE STEP SLIDER SOLUTION.....	94
A.2.4 ANALYTICAL 2-D HEX LAYOUT SOLUTION.....	95
A.2.5 NUMERICAL 2-D SQUARE ASPERITY SOLUTION.....	96
A.3 REYNOLDS EQUATION (IN 2-D).....	99
A.3.1 CONTINUITY EQUATION.....	99
A.3.2 FORCE EQUILIBRIUM ON A FLUID ELEMENT.....	100
REFERENCES.....	102
VITA.....	104

List of Tables

Table 1: Parameter values used in Etsion's paper	4
Table 2: Parameter values used in Stephens' paper.....	6
Table 3: Parameter values used in present thesis.....	8
Table 4: Coefficients of friction.....	13
Table 5: Applications of structured surfaces [10].....	19
Table 6: Geometries used in this thesis.....	52
Table 7: Comparison of ANSYS and analytical solution	59
Table 8: Convergence values	60
Table 9: Comparative results for even and staggered grids	61
Table 10: Sample results for a radial distribution.....	64
Table 11: Peak pressures for different shapes.....	68
Table 12: Peak Pressures for constant film thickness.....	69
Table 13: Coefficients of friction for the 2-D analytical model	72
Table 14: Comparative values of c.o.f. for a positive square asperity	83
Table 15: Comparative leakage values for a positive square asperity	83
Table 16: Continuity of flow with the first approach	84
Table 17: Comparison of continuity of flow.....	84
Table 18: Critical data from the results.....	86

List of Figures

Figure 1: Patterns used in Walowitt's paper [5]	3
Figure 2: Nickel-plated hexagonal microasperities [1].....	6
Figure 3: Mechanical seal with microstructures	8
Figure 4: Surface roughness [22].....	10
Figure 5: Interaction of surface irregularities [22].....	12
Figure 6: Stages of wear [28].....	14
Figure 7: Topography of a polished specimen [22].....	15
Figure 8: Transfer layers.....	16
Figure 9: Shear force on a fluid element.....	17
Figure 10: Striebek curve [22].....	18
Figure 11: Modified LIGA process [1].....	20
Figure 12: PMMA template [1]	20
Figure 13: Electroplated microstructures [1]	21
Figure 14: SEM details of an asperity groove [1].....	23
Figure 15: Convergent wedge [25]	24
Figure 16: Velocity distribution [22].....	25
Figure 17: Couette flow over idealized asperity [5]	27
Figure 18: Cavitation with rolling [22].....	28
Figure 19: Squeeze effects [22]	29
Figure 20: Directional roughness [22].....	29
Figure 21: Elastohydrodynamic effects [22].....	30
Figure 22: Rayleigh step bearing	32
Figure 23: Negative step slider	34
Figure 24: Full Sommerfeld pressure distribution.....	35
Figure 25: Half Sommerfeld pressure distribution [29].....	36
Figure 26: Reynolds pressure distribution [25]	37
Figure 27: Types of arrays	38
Figure 28: Types of asperity geometries.....	38
Figure 29: Orientations of asperities.....	38
Figure 30: Hexagonal asperity layout.....	39
Figure 31: Unit cell sliding system.....	39
Figure 32: A 2-D full Sommerfeld pressure distribution.....	40
Figure 33: Shear flow on a unit cell.....	41
Figure 34: Leakage paths for a positive asperity	42
Figure 35: A finite difference mesh [33]	44
Figure 36: A hexagonal asperity in a square mesh	46
Figure 37: Negative asperity model.....	47
Figure 38: Flow chart for a numerical scheme	49
Figure 39: Microasperities on a thrust bearing (not to scale)	50
Figure 40: Load support curves for sealing pressures	53
Figure 41: Load support for number of asperities	54
Figure 42: Load support for asperity radius.....	55

Figure 43: Load support for asperity area fractions.....	56
Figure 44: Load support for asperity heights.....	57
Figure 45: Load support for film thickness.....	58
Figure 46: Even, staggered grid and analytical results.....	60
Figure 47: Benchmarking for a 2-D model.....	62
Figure 48: Radial pressure distribution for smaller pores.....	63
Figure 49: Radial pressure distribution for larger pores.....	64
Figure 50: Interasperity pressures in a radial layout.....	65
Figure 51: Reynolds pressure distribution for a positive hexagon.....	66
Figure 52: Reynolds pressure distribution for a negative hexagon.....	67
Figure 53: Reynolds pressure distribution for a positive triangle.....	67
Figure 54: Reynolds pressure distribution for a negative triangle.....	68
Figure 55: Leading edge shapes of different geometries.....	69
Figure 56: Coefficient of friction for a square positive and negative asperity.....	70
Figure 57: Comparison of coefficient of friction for all the cases.....	71
Figure 58: Coefficient of friction for a square and a diamond.....	73
Figure 59: Coefficient of friction for a triangle and its orientation.....	73
Figure 60: Coefficient of friction for a hexagon and its orientation.....	74
Figure 61: Film thickness of a positive and negative square asperity.....	75
Figure 62: Film thickness results for all the cases.....	76
Figure 63: Film thickness and leakage for a square asperity.....	77
Figure 64: Leakage comparison for different shapes for Poiseuille flow.....	78
Figure 65: Leakage for all the cases due to Poiseuille flow.....	79
Figure 66: Leakage comparison for square and diagonal asperities.....	80
Figure 67: Comparison of leakage for a triangle and its oriented shape.....	81
Figure 68: Negative square asperity model.....	82
Figure 69: Pressure distribution with hydrostatic pressure b/c	82

List of Files

Filename	File size
1. Sirithes.pdf.....	986 KB

Chapter I: INTRODUCTION

1.1 BACKGROUND

The field of tribology encompasses the study of friction, lubrication, wear and contact mechanics of engineering surfaces with a view to understanding surface interactions in detail and then suggesting solutions to underlying problems. The impact of these problems is of great economic significance since they are concerned with reliability, maintenance and wear of equipment and machinery in a host of applications including biology, industrial machinery, automotive, computers and spacecraft.

Various single and multi tool metal cutting manufacturing operations such as turning, planing, milling, broaching, boring, tapping, and other production processes like stamping, extrusion, forming, rolling, and injection molding, all have tribological aspects associated with them. In metal machining operations, friction is generated between the tool, the chip and the work piece. Shear and normal stresses originate at the interface of the tool and the flowing chip. Due to high stresses, high temperatures are formed at the tip of the tool that affect both the rate of the wear and the friction. Tool wear is caused both by mechanical and temperature factors. Cutting fluids serving as lubricants and coolants help in reducing the effects of dry friction. Hobbing, broaching, gear cutting and similar low speed cutting operations use oils for enhanced lubrication, rather than cooling.

Common automotive components such as tires, brakes and engines experience both sliding and rolling friction. If tires are smooth and the road conditions are dry and clean, high adhesive friction is induced and coefficient of friction reaches as high a value of 5. On the other hand, wet conditions inhibit adhesive friction and consequently low coefficients of friction of 0.1 or less are experienced. In narrowing down such wide differences in friction coefficients, tires are treaded (grooved) to reduce adhesive area and to channel out entrapped water.

To increase the recording density of hard disks in computers, the read/write head ideally needs to be in contact with the disk. As this condition causes high friction and wear, the tribological problem a design engineer is faced with, is to find an optimal gap that is usually in the range of nanometers.

Components such as mechanical seals, brakes and clutches develop surface damages that appear as dark patches over their frictional surfaces. These are sometimes referred to as hot spots and are formed due to intense local heating. They cause thermal expansion in those local areas leading to the formation of higher pressures. Consequently, higher temperatures are generated that further aggravate thermal expansion. This cyclical chain of events continues till failure occurs. This phenomenon called as thermoelastic instability, is yet another challenge to tribology engineers.

The magnitude of the problem of friction, for example, can be understood by the estimate that nearly a third of world's energy utilized appears as friction in one form or another. Conserving such high losses assumes paramount importance due to ever growing demand for energy. Efforts have therefore been, to reduce friction at every level of technology with exceptions where it is desirable such as, anti skid surfaces, brakes and similar applications.

The expanding range of tribological applications, traditionally from industrial machinery to computer hard disks and micro/nano applications lately, has not only demonstrated its importance, but also revived interest in this field. The origination of a range of microfabrication techniques (Lithographie Galvanoformung Abformung, Laser Machining) coupled with developments in microscopy (Optical, Scanning Electron and Atomic Force Microscopes) has had a profound effect on the resurgence of tribological applications at the microscopic levels. With the help of this new technology, it is now possible to produce positive and also negative microstructures on thrust bearing surfaces to improve the overall tribological performance including reduction in friction, wear and interfacial temperatures, improvement in reliability, increase in severity conditions, lowering energy consumption and minimizing maintenance costs.

1.2 RELATED AND EARLIER RESEARCH

One of the earliest works in the field of microasperity lubrication was based on the experimental evidence found at Battelle Memorial Institute by Hamilton, D.B., et. al. [5]. A lapped carbon graphite stator with $5\mu\text{in}$ (RMS) surface roughness was run against an optically flat transparent rotor. Mineral oil with a kinematic viscosity of 400cst (*centistokes*), was used as an interfacial film. Narrow, long discontinuous cavitation streamers were observed. The interruptions in streamers corresponded with the surface roughness of the carbon graphite stator.

Subsequent experiments were carried out to find the effect of surface roughness on cavitation. A smooth, nickel-plated steel stator was run against a pyrex rotor. Initially it produced high torque but later, with the appearance of a broad band of cavitation near the inner radius, the torque dropped sharply. Cavitation streamers soon appeared almost over the entire interface.

The next set of experiments was conducted using a flat, but rough stator surface. Roughening was done in one case by lapping with 600-grit compound and in the other by light vapor blasting. Numerous cavitation streamers were found in both these cases. An attempt to relate the topography of lapped carbon graphite to seal performance was infeasible because of the difficulty in mathematically representing the surface that is composed of many irregular microscopic pits and asperities of varying sizes and shapes. Hence, regular patterns were generated on a flat metallic stator surface to facilitate modeling. With photoetching cylindrical micropost heights up to 100microinches and flatness on the grooves to within $\pm 8\text{microinches}$ were achieved. The photoetched copper ring was soft soldered to a steel substrate and run against smooth pyrex and steel rotors in different experiments. Three different patterns, one varying in asperity diameter and the other in asperity height, were used in this study. Load carrying capacity was found to vary linearly with speed in all these cases. However, the magnitudes were different. Further experiments conducted on an identical pattern but with varying heights showed an inverse relationship between load capacity and asperity height.

The characterization of microasperity lubrication by the combined effect of asperity dimensions and the association of cavities with each asperity, as pointed out earlier, have thus formed a basis for theoretical models.

At first, a simple one-dimensional model was used to show the association of cavities and asperities. Two-dimensional analytical models, with approximations in boundary conditions, were later used to study the combined effects of asperity geometry and cavitation. The experimental critical speeds, below which no cavitation occurs and hence load support is zero, agreed with the theoretical data, within a given experimental error. However, the model could not reproduce the pattern of cavity representation. In addition, the experimental values of load support were higher, 14.2 psi (0.1 N/mm^2) instead of 7.2 psi (0.05 N/mm^2). The reason attributed

for this difference partially, was the assumption of the type of cavities used in theoretical analysis, in which streamers of cavitation are not accounted for. In conclusion, the authors have claimed that their investigation has shown a qualitative agreement of theory with experiments.

In an attempt to explain the difference in load support values, the authors have assumed small tilts on asperity tops in subsequent paper by Anno, J.N., et. al.,[6]. The tilt was 0.86 *microinches* (34.4 *micrometers*) in a diameter of 12 *mils* (0.3048 *mm*). The theoretical model was simplified by approximating the solution as a summation of infinite series and then by truncating the resulting series. The justification of these assumptions was based on the use of small inclination for the tilt. A good correlation between the experimental and theoretical results, both for film thickness and for friction coefficient, was observed. The standard deviation of the experimental data for film thickness, from the fitted curve was 1.25×10^{-6} *inches* (50 *micrometers*). Since Talysurf measurements could not detect the small tilts, the authors were unable to demonstrate their claim on the tilt theory. Instead, indirect evidence was shown by increased load support values based on increased tilts.

In a third paper in 1969 [7], authors Anno, J.N., et. al., have compared the load support and leakage performances of positive and negative asperities using the previously mentioned small tilt theory of asperity tops. They have compared positive square asperities with negative circular asperities, both distributed in a square array. Different arrays (patterns) for microasperities were also used in this study such as, positive circular asperities in a hexagonal array.

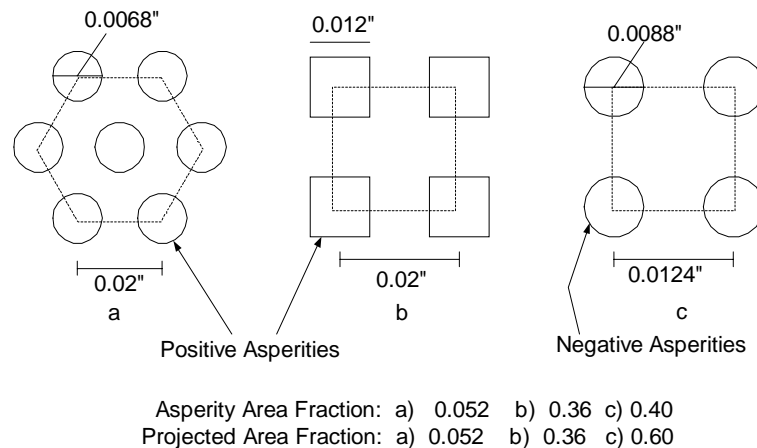


Figure 1: Patterns used in Walowitt's paper [5]

Figure (1) shows the arrays considered in this study. For all the cases, the protruding area, other than the asperity area, was taken as the effective area while comparing positive and negative asperities. The authors have found similar load support with all the above shapes. However, experimental leakage rates for negative asperities were very less when compared to positive ones.

These findings on negative asperities have lately revived interest among researchers, partly due to the developments in microfabrication techniques such as laser ablation. The studies are also influenced by increasingly stricter environmental controls on permissible emissions. Most noticeable contribution on analysis and experimental work on laser-textured surfaces is by Etsion, I. and his group.

In one of their earlier papers in 1996 [8], Etsion and Burstein developed a mathematical model for hemispherical pores arranged in a rectangular array. Numerical methods using finite differences were employed to solve Reynolds Equation with Half Sommerfeld condition. The range of pore diameters and pore ratios used were $5\mu\text{m}$ to $200\mu\text{m}$ and 2.5% to 20% respectively. They have found that pore size and pore ratio influenced the seal performance significantly only in a certain range. An optimum value for a pore size was found to be dependent upon sealed pressure, viscosity and pore ratio. It decreased with lower viscosities, higher sealed pressures and lower pore ratios. Subsequently, in 1997, Etsion, I., Halperin, G., and Greenberg, Y. have presented experimental results on laser textured seal faces [4]. The experimental variables are listed in table (1).

Table 1: Parameter values used in Etsion's paper

<i>Parameter</i>	<i>Specifications</i>
4340 Steel Rings O.D. & I.D.	38 mm/ 26 mm
Thickness of ring	10 mm
Surface Roughness	0.01-0.02 μm
Pore Diameter	90 μm
Pore Depth	2 μm – 26 μm
Pore ratio	25%
Speed	500-3000 RPM
Load	60 N – 300 N
Viscosity of Oil	0.136 Pas at 40 ⁰ C.
Maximum PV value	2.5 MPa.m/s

A comparative study of super polished plain and textured seals revealed that textured seals withstood higher PV (Pressure Velocity) values, indicating their preference in selection for better seal performance. Further, textured seals carried more axial load and possessed higher film stiffness. The results for film thickness were estimated from torque measurements and by using the mathematical definition of dynamic viscosity, $\tau = \mu \frac{du}{dy} \approx \mu \frac{U}{h_0}$

As the film thickness decreased, textured seals carried more axial load, indicating increased film stiffness. In contrast, a converse relation was observed with a plain seal. The best performance was observed when optimum pore depth was 7 μm .

These two papers were followed by another paper [3] in 1998, dealing with both experimental and theoretical aspects of spherical shaped laser textured seal faces. In this paper, the authors used improved models by considering pores in a radial direction instead of a rectangular array. Also, the widely accepted Reynolds cavitation was used instead of Half Sommerfeld condition. Numerical simulations showed that the area density of pores and the radius ratio (*I.D.* / *O.D.*) of the seal had little effect on the generation of average pressure. In addition, numerous simulations yielded an optimum value of depth to diameter ratio of 0.05.

Hemispherical shapes with a depth over diameter ratio of 0.5 were shown to have the least performance. As expected, models also showed that a textured seal can perform as ineffectively as a plain seal if hydrodynamic effects are reduced by using low non dimensional seal parameter.

A non dimensional seal parameter was given as, $\Lambda = \frac{6\mu U r_p}{P_a b^2}$, where r_p is the radius of the pore.

Experiments were conducted on a *SiC* laser textured seal operating with water as a lubricant and run at 4000 RPM. The pores had an average diameter of $95\mu m$ and a depth of $6\mu m$, with a pore density of 20%. Experimental results showed a good correlation with the theoretical predictions of average pressures for different seal clearance values. The average pressure increased with decreasing seal clearance (film thickness).

Application of laser textured seal faces on a circumferential gas seal is found in reference [22]. Analysis is done with FEM method using Reynolds Equation for compressible viscous gas in a laminar flow. Micro pores in gas seals generated enough hydrodynamic pressures to maintain small film thicknesses between rotating shaft and sleeve so that friction and wear are reduced. Numerous simulations also revealed that maximum opening force was observed when area density of the pores varied between a ratio of 0.1 to 0.5 and when the aspect ratio of pores was between 0.01 and 0.03. The average pressures generated were 50% more than the ambient pressure level. In addition, for any given area density of the pores, there exists an optimum value of aspect ratio that produces maximum average pressure.

Application of laser textured seal faces in automotive engines is given in reference (2) in which it is estimated that 40% of total energy produced is wasted as friction. Piston rings and cylinder liner losses account for 50-60% of the entire frictional losses. A numerical approach using finite difference method was used to solve time dependent Reynolds equation. In addition to the expected wedge effects, squeeze film effects are also considered in this application. The instantaneous pressure distribution curve for a strip of pores showed that asperity interactions were significant. Area density changes in the range of 5-20% produced a variation of friction force less than 7%. For all values of depth over diameter ratios, the average friction force diminished as number of asperities was increased. However, the rate of decrease was significantly less beyond a critical number of asperities. When compared with depth over diameter ratio, average friction force exhibits an optimum value for different bearing numbers (similar to compressibility numbers or seal parameters) and also for different values in external forces. The optimum pore depth to diameter values for all the cases varied in the range of 0.1 to 0.18. It was estimated that due to hydrodynamic effects, friction reduction up to 30% could be achieved with laser-textured surfaces.

1.3 THESIS OVERVIEW

As an alternative to laser textured pores, positive asperities of deterministic pattern can also be used to enhance hydrodynamic effects of thrust surfaces, as shown in earlier studies [5]. Bearings and Seals laboratory at the University of Kentucky has set up two types of microfabrication processes, LIGA and UV Photolithography, in their modified forms. While the first process, used for fabricating positive asperities, offers an advantage of achieving higher aspect ratios, the latter is used for producing either positive or negative asperities, but with smaller aspect ratios. Further, these techniques can be used to fabricate any prescribed cross section. Fabricated at University of Kentucky, figure (2) shows a thrust surface consisting of an array of hexagonal asperities made of nickel.

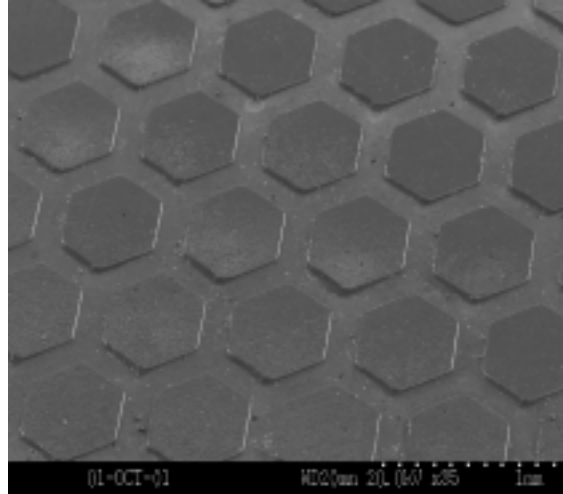


Figure 2: Nickel-plated hexagonal microasperities [1]

SEM and optical interferometer pictures of microstructures have demonstrated the accuracy of producing microstructures, with 13nm Ra surface roughness on asperity tops and a flatness of $3.9\mu\text{m}/\text{mm}$ in the grooves. The process of pattern generation on photoresists through UV photolithography is presently being developed by UK Bearings and Seals laboratory [32]. Photoresists developed through X-ray radiation are alternatively available from Louisiana State University with which UK Bearings and Seals laboratory has collaborations on application of High Aspect Ratio Microstructures (HARMs) in mechanical seals to act as heat sinks [1]. Photoresists developed through UV photolithography are predominantly used in silicon wafer industry. Its limitation of producing only small aspect ratios is serving to be useful for applications in microasperity lubrication, where asperities of a few microns in height are required.

The UK Bearings and Seals Laboratory conducted a few experiments with nickel based hexagonal asperity seals run against carbon graphite in an SAE30 oil bath. The details of specimen are furnished below in table (2) and taken from [1].

Table 2: Parameter values used in Stephens' paper

<i>Parameter</i>	<i>Specifications</i>
Steel Ring with nickel top, O.D. & I.D.	28.6 mm/ 25.4 mm
Thickness of ring	12.5 mm
Surface Roughness	$0.013\mu\text{m}$
Asperity Diameter	$550\mu\text{m}$
Asperity Height	$3\mu\text{m} - 100\mu\text{m}$
Asperity Area Fraction	59%
Speed	2500 RPM
Load	$0.1\text{ N}/\text{mm}^2$
Viscosity of Oil	42-110 cP
Asperity Density	$2.5\text{ asp}/\text{mm}^2$

An analytical model from reference [5] was used to compare the test results. The experimental results followed the theoretical predictions in the generation of hydrodynamic lubrication for $3\mu\text{m}$, $7\mu\text{m}$ and $14\mu\text{m}$ tall asperity heights. The experimental values for coefficients of friction were 15- 38% lesser than the theoretical values, but the trends agreed with each other. As expected, an increase in the average film thickness was noticed with a decrease in friction coefficient. The optimum value of asperity height for minimum coefficient of friction is found to be $7\mu\text{m}$. The value of coefficient of friction rapidly increased from 0.32 to 0.65 when asperity height was increased from $14\mu\text{m}$ to $100\mu\text{m}$, demonstrating the transition from hydrodynamic lubrication to mixed lubrication. The experimental results for asperity-based surfaces revealed a substantial gain in friction reduction of 14-22% over plain-faced surface having a coefficient of friction of 0.39. Further, theoretical models showed a potential in additional reduction of friction coefficient up to 60%, from 0.39 to 0.15, by decreasing the number of asperities from $0.53\text{asp}/\text{mm}^2$ to $0.10\text{asp}/\text{mm}^2$. A number of other factors including asperity layout and asperity area fraction also affect coefficient of friction, the information regarding which was beyond the scope of the paper.

This present thesis is an effort to bridge such gaps in theoretical studies by finding the effect of the rest of the parameters on important tribological factors such as coefficient of friction and leakage. Since most of the available literature on microasperities is focused on pores (negative asperities), this work, based on both positive and negative asperities, extends the range of the existing literature to cover a variety of deterministic microasperities consisting of hexagonal, triangular, square and circular geometries in their entire range of asperity area fractions. It utilizes a distinctive and practical approach for comparison by considering constant load conditions as is expected in an operating thrust bearing (figure 3). This approach is a significant departure from the existing practice of constant film condition that is widely used in the literature, [2], [3] and [4]. In addition, the present study not only eliminates the inconsistencies observed in earlier work [7] as described before and shown in figure (1), but also presents the results for an entire range of asperity area fraction that is not undertaken earlier. The common variables used for comparison are narrowed down, and results are presented by using an identical layout, by considering equal dimensions and by consistently defining asperity area fraction in both the cases of positive and negative asperities. Consequently, the results are expected to provide us a better understanding of the role of asperity area fraction alone on hydrodynamic properties, as it is one of the most influencing factors in generation of load support. The values of parameters used in our paper are given in the following table (3).

Table 3: Parameter values used in the present thesis

<i>S.No</i>	<i>Parameter Symbol</i>	<i>Units</i>	<i>Parameter Value</i>
1	N	Asp/mm^2	1.34
2	L	μm	864
3	U	m/s	2.66
4	r_o	mm	11.21
5	r_l	mm	15.69
6	a	μm	5
7	Δp	N/mm^2	0.07
8	μ	cP	42

1.4 TARGET APPLICATION

Some rotating shafts with high axial load carrying components such as thrust bearing surfaces are potential tribological applications of deterministic microasperities. The bearing surface is perpendicular to the axis of the shaft and generates a lot of frictional heat. Reduction in frictional losses increases the life of the thrust bearings and saves energy losses. High aspect ratio (HARMs) microstructures may be used for heat sink applications [1].

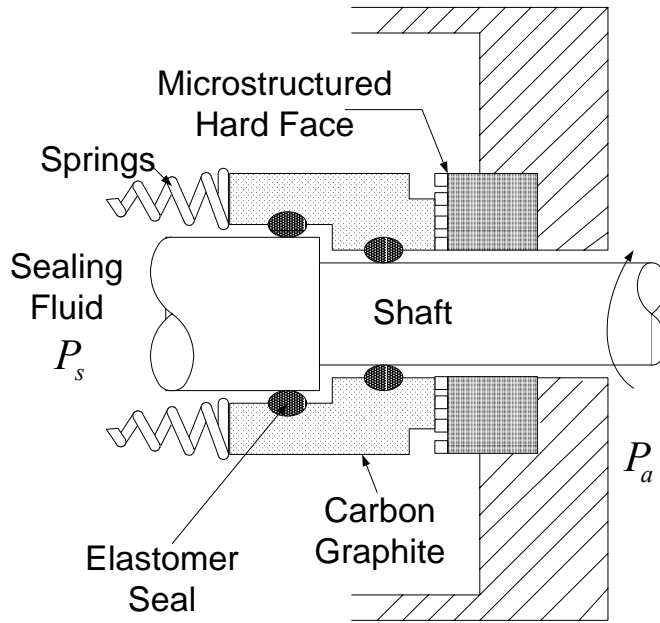


Figure 3: Mechanical seal with microstructures

Mechanical seals offer high prospects for potential application of microstructured seal face to improve the seal performance (figure 3). In contrast to heat sink applications, the microstructures for lubrication are required to be of very low aspect ratios. Each asperity acts as a hydrodynamic bearing in the presence of a lubricant and a sliding surface. The composite effect of all such asperities provides the load carrying capacity and thus, separates the faces of the seal to prevent wear and friction. However, leakage may be increased. By a proper design of microasperities, desired seal performance can still be achieved.

Chapter II: BASIC CONCEPTS

2.1 SURFACE TOPOGRAPHY

Friction is related to the surface topography of interacting surfaces. All real surfaces are composed of texture and structure at both macroscopic and microscopic levels. Texture is related to roughness, waviness and lay of a surface, excluding form error, whereas structure is related to its geometric features. While roughness constitutes shorter wavelength components of a surface profile, form represents longer wavelengths. Waviness lies somewhere in between, on this scale. Lay relates to the directionality in the texture. Surface texture of all manufactured surfaces (also called as engineered surfaces), is determined by the machining operation that it underwent before. Essentially, it is the result of a combined effect of the geometry of the tool and its kinematics during machining. Surface texture can be produced and also measured. Measurements are done by a variety of methods including profilometry, cartography, optical interference and field emission microscopy.

When an apparently smooth machined surface is viewed under a microscope, a number of randomly distributed peaks and valleys of varying heights are observed. Each such element is termed as an asperity. Generally the peaks contribute to the friction whereas the valleys serve as reservoirs for lubricant that is used to reduce friction.

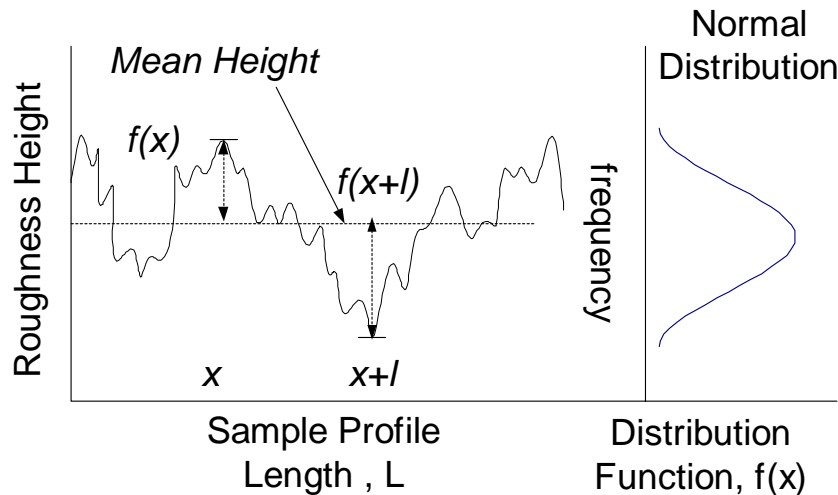


Figure 4: Surface roughness [22]

As shown in figure (4), statistical quantities are used to express surface texture. Profiles of machined surfaces are expressed in terms of

- a) The Arithmetic Average and the Standard Deviation (RMS),

$$R_a = \frac{1}{L} \int_0^L |f(x)| dx \quad (1)$$

$$R_q = \sqrt{\frac{1}{L} \int_0^L f^2(x) dx} \quad (2)$$

b) Auto correlation function and

$$R(l) = \frac{1}{L} \int_0^L f(x)f(x+l)dx \quad (3)$$

Auto correlation function gives the expected value of the product of a random variable with a delayed version of itself. When applied to surface roughness, it can give a measure of non randomness in the surface profile. An auto correlation coefficient (defined as $R(l)/R_q^2$) of '1' means a predictable value of surface roughness and a value of '0' means a total randomness. When the delay, l , is zero, it is equivalent to R_q^2 . Surface classification may be based on the shaped of the correlation function and the magnitude of correlation length $\lambda_{0.5}$, defined by $R(\lambda_{0.5}) = 0.5$ [24].

c) Power spectral density is the Fourier cosine transform of the auto correlation function and is given as;

$$P(\omega) = \frac{2}{\pi} \int_0^{\infty} R(l) \cos(l\omega) dl \quad (4)$$

It is suitable for the study of machined surfaces as it identifies surface periodicities that may result from waviness of machining processes [24].

All the above statistical quantities correlate the surface texture and the intended function of the surface. For a normally distributed peaks and valleys as in the case of most engineering surfaces, the mean and auto correlation function completely characterize the profile. In case of an elastomer/ rigid surface contact, a single profile is needed whereas for a metal on metal application, a pair of profiles is required for characterization.

2.2 ACTUAL AND MODEL SURFACES

The geometry of an engineered surface is truly random. To represent it deterministically, it is customary to consider the actual random asperities as a selection of different sizes of ideal shapes such as cubes, cones and spheres. A linear profile idealizes saw tooth and sinusoidal asperity models.

Since the idealized shapes bear little resemblance to the actual surface, a few techniques could be used to improve the model. One of them is to represent all the three basic shapes in one model with uniform height. A second method is to consider one basic shape but, with different heights. And a third method is to maintain the same height but use randomness of shape and spacing. Though the actual surface is truly random, the following simplifications are necessary for modeling purposes.

- Instead of an entire length, a representative portion is considered, based on the assumption that there is repeatability in profile.
- This profile is assumed to be isotropic.
- The size, spacing and shape of an asperity are also assumed to be the same all over the sample.

These techniques, though used for random surfaces, are particularly well suited for our patterns of repeated features.

2.3 FRICTION

Friction is a dissipation mechanism in which energy gets converted to heat and cannot be utilized. It occurs at the interface of any two contacting bodies when sliding, rolling or separation takes place between them and tends to oppose the very force that causes the relative motion. Friction is usually accompanied by wear, which is a material removal process. Similar to wear, friction is aggravated by contamination, corrosion or environmental degradation. Both friction and wear are minimized by lubrication.

Based on the nature of contact between two surfaces, two broad distinctions of friction can be made when hardness of the two contacting surfaces differs widely or slightly. These are the metal-on-metal and elastomer-on-rigid surface contacts respectively.

Historically, there are few theories explaining the phenomenon on friction, based on its physical nature. However, in recent years, research on MEMS and Nano Technology has revealed its chemical origins too and hence it is now considered to be a combination of physical and chemical processes. Some of the latest literature is focused on chemical aspects of friction, dealing with it at a molecular level [9]. According to this, friction can exist between two surfaces at nano level separation, even before a normal load is applied, because of the development of adhesive bonds between molecules of opposing faces. The famous Amonton's law, friction is proportional to the normal load, cannot explain such molecular origins of friction, in the absence of application of any external force. Friction at this molecular level can be measured with the use of Atomic Force Microscopes (AFM).

But, the theory proposed by Bowden in 1950, called as the welding, shearing and ploughing theory, is a widely accepted physical explanation for metal friction (including our system of tungsten/silicon carbide and carbon graphite) at a microscopic level for simplifying the understanding of friction. According to this theory, physical interactions of the surface irregularities at different heights are considered as shown in figure (5).

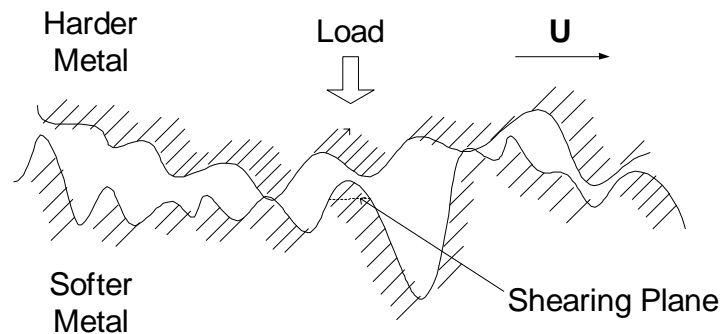


Figure 5: Interaction of surface irregularities [22]

When two surfaces are subjected to a compressive load, contact initially starts at least at three peak points of zero contact area. Since the pressure generated at such points is very high, plasticity point is reached and deformation takes place. Plasticity still continues such that the total contact area increases but, the average area of a contact junction remains constant. The actual contact area is a small fraction of the geometric area. Local welding of asperities, also called a cold welding, easily occurs at the contact spots, if the surfaces are clean. If contaminants or oxide films exist, a smaller size and lesser number of junctions are formed. The strength of

these junctions is as good as the base metal. Due to a relative motion between the surfaces or due to an increased load, these junctions grow and keep increasing the frictional resistance. When sufficient shear load is reached, the junctions shear off near their weakest planes and this is when maximum resistance is experienced. This phenomenon contributes to the adhesive type of friction. Additionally, certain other harder asperities cut or plough through the softer metal surface during the course of relative motion. Hard asperities are either due to a sufficiently harder material or due to work hardening process that is generally observed in most metals as result of plastic flow. This deformation of the softer material gives rise to the ploughing component of friction. The presence of an abrasive third body such as sand, wear particles and dirt also has a similar effect. Non-abrasive contaminants, oxide films and lubricants on the other hand, decrease friction by reducing the above effects. Temperature generated due to frictional resistance has two opposing effects on friction. It increases ductility leading to junction growth and ultimately seizure. However, it also helps in the formation of oxide films that tend to inhibit friction.

For metals, coefficient of friction, f is obtained when friction force is divided by the normal force and is expressed as:

$$f = \frac{F}{W} = \frac{As}{Ap} = \frac{s}{p} = \frac{\text{ShearStrength}}{\text{YieldStrength}} \quad (5)$$

where F is the frictional force, W is the applied load, A is the total shear area.

Typically, yield pressure; p is approximately equal to 5τ where τ is the critical shear stress of a metal. And in metals that are not work hardened appreciably, s is approximately equal to τ . Given this data, one can estimate the value of f approximately as 0.2. However in practice, most metals give a value of f equal to 1.0 in air. This discrepancy is explained by the unaccounted factors of junction growth and work hardening that occur in a metallic contact. A few frictional values are given in table (4) below.

Table 4: Coefficients of friction

Material Pair	Dynamic Friction Coefficient	
	Dry¹	Lubricated²
Mild Steel on Mild Steel	0.57	0.19
Nickel on Nickel	0.53	0.14
Nickel on Mild Steel	0.64	0.18
Carbon Graphite on Silicon Carbide	-	0.15
Very Rough Surfaces	1.5	
Synovial Joints in Humans	N.A.	0.003*

1 Unlubricated - 2. Boundary/Mixed lubrication except for *

2.4 WEAR

Wear is generally associated with friction and takes place in both metals and elastomers. Metallic wear is affected by the factors of work hardening, oxide films, metal transfer and phase changes in metallurgical composition.

Wear is defined as a progressive loss of a solid material from the surface either under some dynamic conditions such as, sliding, erosion, fretting or due to impact or temperature effects. With the exception of certain machining processes such as grinding and polishing, wear is obviously an undesirable but, unavoidable process, as it gives rise to greater tolerances between moving components, higher machining loadings and even fatigue failures.

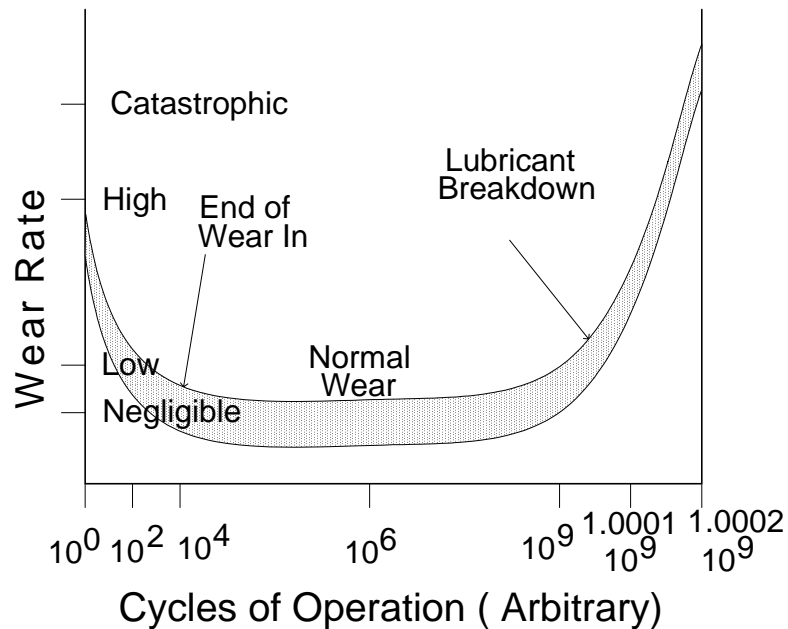


Figure 6: Stages of wear [28]

Figure (6) shows various stages of wear before a failure occurs. It may be observed that high cycles of operation are detrimental to the rubbing components. Reducing and predicting all kinds of failures is important in improving the reliability of industrial machinery. Wear debris collected through oil analysis is useful in predicting such failures. An understanding of various types of wear helps in identifying them. Following are two of the most relevant categories.

2.4.1 Adhesion

This type of wear occurs due to the generation of small particles from the rubbing surfaces as a result of shearing of mechanically interlocked asperities or due to localized adhesion at contact spots. The lubricant usually removes the wear debris without resulting in gross surface damage. However, in the case of high loads, due to increased contact area, the wear particles remain within the rubbing surface and cause abrasive action, thus accelerating wear.

2.4.2 Abrasion

Abrasive wear constitutes for 50-60% of the wear of industrial components. Abrasive wear process as compared to pitting is relatively uniform and continuous. When a hard material damages the surface of a softer material, it leads to abrasion. It could be a two body wear as in a ploughing action, a three body wear as found in the presence of abrasive contaminants or as observed with an erosive action due to the impingement of hard particles at a higher velocity. Erosion caused by cavitation is not included in this type of wear. Scratching, gouging and grinding are also the causes of this type of wear. Scratching, as found in sand slingers or chutes, is a low stress abrasive wear caused due to repeated scouring action of abrasives moving across metal surfaces at varying velocities. High stress grinding is also called as third body abrasion in which abrasive particles under compressive loads are crushed in between two metallic surfaces leading to scoring or surface cracking. This is found in brake drums and rollers. When either a low stress or a high stress abrasion occurs under the influence of impact of weight, gouging or grooving takes place. Power shovel buckets and rock crushers form examples of this kind. The formation of grooves (scoring) in hydrodynamic bearings also is an example of abrasive wear caused due to particles of wear debris larger than the maximum film thickness.

2.5 CONTACT MECHANICS

The integrity of machinery components with interacting surfaces such as gears, bearings or cams is of paramount importance for productive plant operations. On such surfaces, loads are often supported on very small areas resulting in high stresses and contact pressures. Ignoring to design the components for high stresses or deformation can lead to component failure either by overloading (plastic yielding or fracture from excessive contact loading), wear, seizure (welding of surfaces by high temperatures created by high stresses), fatigue (failure due to cyclical contact stresses that usually starts with a crack initiation) or loss of tolerance (due to deformation or wear). Lubrication generally helps in preventing wear and seizures. Analysis of contact stress can be done by closed form solutions or by numerical methods.

2.6 SURFACE CONTAMINANTS

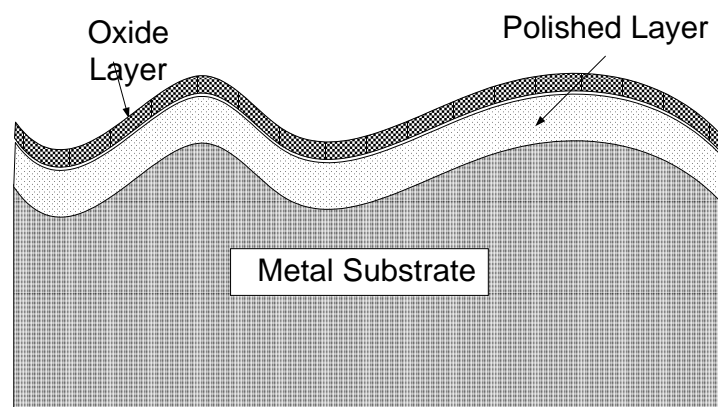


Figure 7: Topography of a polished specimen [22]

Figure (7) shows the topography of a polished metallic specimen. Oxide films readily form on metal surfaces when exposed to air. This layer is generally 0.01 to 0.1 microns thick. Below this is a 0.1micrometer thick polished layer, over the metal substrate. The existence of oxide layer not only affects the adhesion of metals but also contaminates the lubricants.

2.7 TRANSFER LAYERS

The transfer of metal from one sliding surface to the other is linked with the welding-shearing- ploughing theory of friction mechanism. Due to the process of shear of the weaker metal in a plane other than the junction plane, metal transfer takes place to the harder metal.

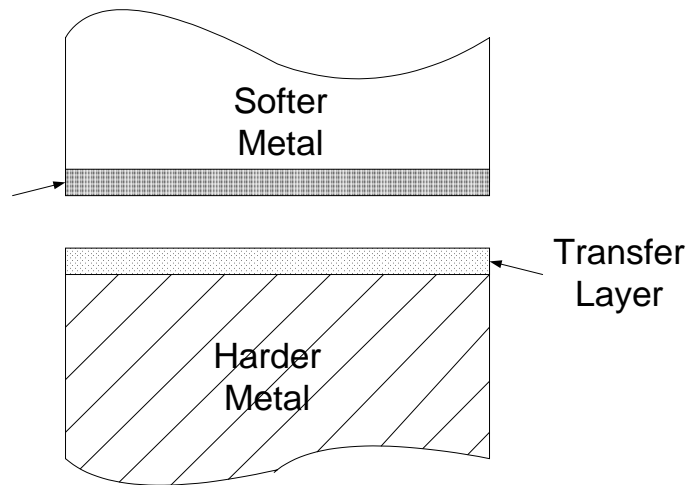


Figure 8: Transfer layers

During initial sliding of the two solid bodies over each other, there is an increase in friction force and temperature. No material transfer takes place in this phase until maximum friction value is reached. Once the transfer begins from soft to hard metal, the friction force starts reducing till it stabilizes. This transfer film need not be homogeneous with all types of softer materials and is amply exemplified by the formation of deposits rather than a layer when graphite is used as a soft material. During the sliding process, another layer called as frictional layer is formed on the surface of soft material (figure 8). As the name suggests, this frictional layer governs the properties of coefficient of friction, wear rate and others. Once the run-in period is completed, the transfer layer forms a sliding contact with the frictional layer and this sliding system governs the overall tribological performance [9].

2.8 LUBRICATION

Surface to surface contact can be prevented by a lubricant, a viscous fluid that can withstand shear loads. Lubrication is the process of introducing such a fluid film to reduce wear and frictional resistance, and also to carry away the heat produced at the interface. Viscosity, that represents the internal friction of a fluid, relates the local stresses in a moving fluid to its strain rate.

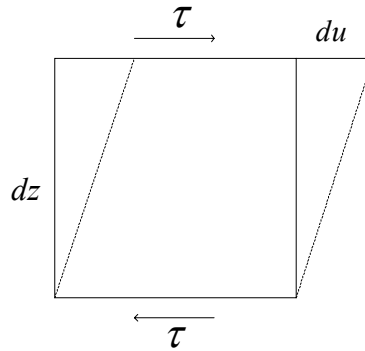


Figure 9: Shear force on a fluid element

When a fluid is sheared, it begins to move at a strain rate inversely proportional to a property called its coefficient of viscosity, μ , obtained from the well-known equation,

$$\tau = \mu \frac{du}{dz} \quad (6)$$

where, τ is applied shear stress, dz is the height of the fluid element cube and du is the relative movement, μ is known as the modulus of viscosity or simply, viscosity. The term, du/dz , indicates the rate of shear (see figure 9 for details).

From equation (6), it follows that the shear stress and strain follow a linear relationship. Fluids that obey this linear law are called as Newtonian fluids. The rest, such as grease, are called as Non-Newtonian fluids. Viscosity, also referred here as dynamic viscosity, is given either in terms of poise or reyns and the conversion factor is $1 \text{ micoreyn} = 14.5 \text{ poise}$.

It is not always possible to keep the rubbing surfaces apart, especially when speeds are low or the loads are high. This situation is characterized by mixed lubrication in which both the asperities and the lubricant present in the intervening space share the load. A much severe condition of mixed lubrication is known as boundary lubrication.

Various types of lubrication regimes can be better understood with the help of a plot of coefficient of friction against generalized Sommerfeld number. This graph is called Striebek curve and is shown in figure (10).

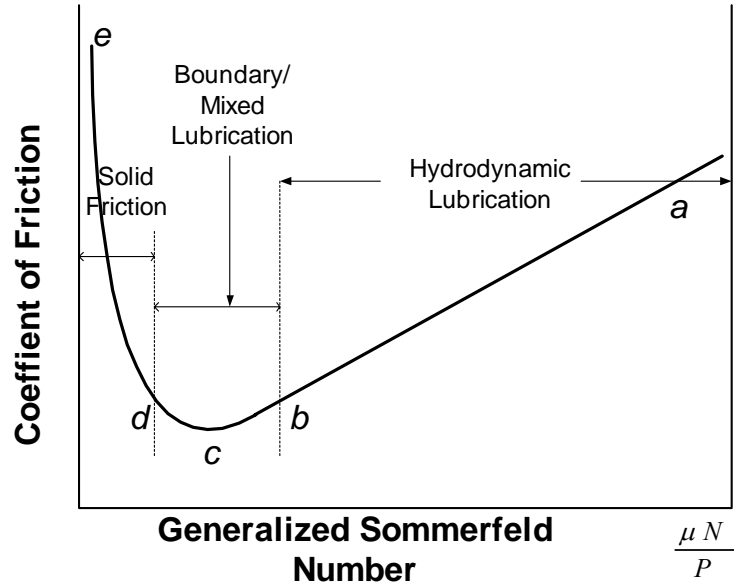


Figure 10: Stribeck curve [22]

Higher values on the abscissa are due to higher film thicknesses and this corresponds to thick film or full hydrodynamic lubrication regime. In contrast, very low values indicate solid friction. The transition is represented by boundary and mixed lubrication regimes. The graph *abcde* can be fragmented into different regions *ab* (hydrodynamic), *bcd* (boundary or mixed) and *de* (solid) and the point *c* gives the minimum value of friction. In hydrodynamic regime, *ad*, a fall in the coefficient of friction is attributed due to a reduction in speed and as speed is further reduced, solid friction comes into play due to the contact of asperities. Due to heat generation, fluid viscosity decreases and so does the shear force, resulting in reduction of this component. Within the boundary regime, the curve requires explanation from all the components of friction as given by the equation,

$$f_{BL} = f_{liq} + f_{solid} + f_{def} \quad (7)$$

The falling slope of *bc* is explained by a general reduction in f_{liq} , greater than the increase due to f_{solid} . If speed is further reduced, more contact area is created and thus, f_{solid} increases rapidly and overcomes the effect of reduction of f_{liq} due to viscosity. Therefore coefficient of friction rises along *cd*. The segment, *de* corresponds to solid friction where the effect of lubricant is almost negligible. Thus, the minimum point *c* indicates the optimum value. However, a slight disturbance in a system operating at this critical point is likely to destabilize and either a high value of friction coefficient is registered or seizure takes place. Therefore it is recommended to operate the system more into the hydrodynamic regime, along the curve *bca*.

In this present thesis focus is made on hydrodynamic lubrication as the fabrication of deterministic asperities on thrust surfaces controls their tribological properties and ensures the provision of lubrication in hydrodynamic region, thus reducing friction and wear.

Chapter III: MICROFABRICATION

3.1 DETERMINISTIC ASPERITIES

Deterministic microasperities are being fabricated at the UK Bearings and Seals Laboratory for subsequent experimentation work in the later part of the ongoing research. This chapter provides an overview of the available microfabrication processes at UK and also briefly describes a few other alternative processes.

These are microscopic surface features having a regular geometry and a repeatable structure. Microstructures can be designed to give a desired tribological performance [5]. An impact on the physical, chemical and optical properties of materials can also be made by modifying the microstructures [10]. Structured surfaces are found on mouse pads, computer hard disks, compact disks, high reflectivity road signs, to name a few. One of the advantages of using deterministic microasperities is to remove the difficulty arising out of quantitatively relating the random surface texture to the function it is intended for. Some of the other applications are given in table (5) below.

Table 5: Applications of structured surfaces [10]

<i>Function</i>	<i>Example</i>
Optical	Gratings Reflective road signs
Mechanical contact	Piston rings/cylinder liners Hard disk surfaces Grooved Roadways
Hydrodynamics	Thrust bearing surfaces Golf balls
Biological	Cell culture systems Breast Implants and Bio-MEMS
Thermal	Heat Exchanger fins
Friction and Wear	Abrasives, Tools, Files and Undulated surfaces

3.2 MICROFABRICATION PROCESSES

3.2.1 Photoetching

Early studies [5] have used the technique of photoetching for microasperity fabrication. In this method, a photoresist of a desired pattern is printed on a lapped metallic surface and then the surface is bathed with an etchant. As a result, only areas of the surface in between the asperities are dissolved, leaving the surface with an array of microstructures.

3.2.2 LIGA (modified)

Figure (11) shows a modified method of LIGA process that involves the processes of lithography and electroplating but excludes molding. Lithography uses either X-Ray or UV rays for irradiating a photoresist. With an X-ray radiation, microasperities with high aspect ratio are achieved.

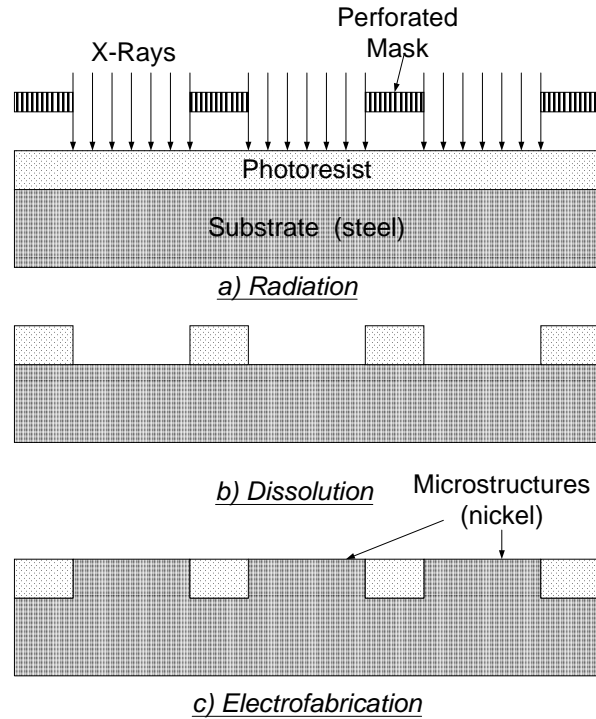


Figure 11: Modified LIGA process [1]

Initially, a mask made of gold is fabricated with the required pattern. X-rays are then allowed to pass through the perforations in the mask to strike a photoresist, made of PMMA (Poly Methyl Methacrylate), only in certain areas as guided by the pattern in the mask. The thickness of the photoresist decides the height of the micro asperities. The photoresist is later developed in a solvent and glued to a specimen on which microstructures are to be fabricated.

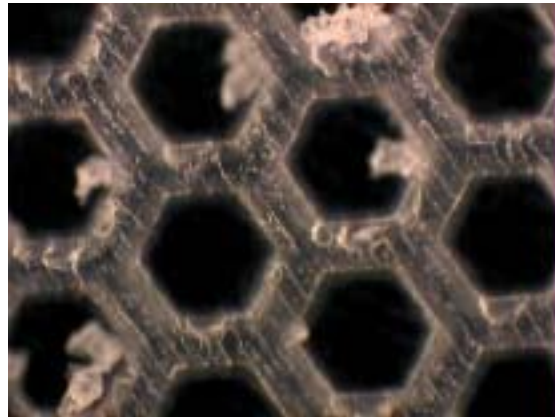


Figure 12: PMMA template [1]

Figure (12) shows a template after development. The specimen is held in jigs and fixtures, electrically connected to an electroplating machine, also called as a potentiostat / galvanostat, and subjected to a series of electroplating processes. The microfabrication lab at the University of Kentucky is currently equipped to produce nickel-based microstructures. After the completion of electroplating, the photoresist is dissolved in acetone to give us a clean surface with an array of microstructures, for e.g., as shown in figure (13).

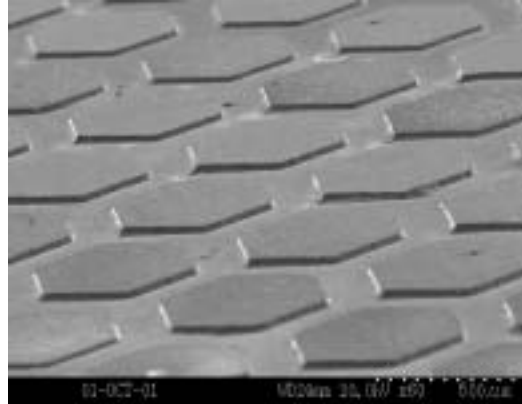


Figure 13: Electroplated microstructures [1]

3.2.3 Laser Ablation

Laser machining process has the capability of producing three-dimensional microstructures on diverse materials such as polymers, ceramics, metals and glass. In this method, laser pulses striking on the surface cause ablation of the material at their focal plane. Similar to LIGA method, with the help of a designed mask, microstructures of a desired geometry can be achieved. A three dimensional surface structure is achieved by using overlaps of single laser pulses in combination with a flexible mask. Heat affected zone near ablation areas are minimized by using lasers with short pulses.

Hemispherical pores up to diameter of approximately *200micrometers* and a depth up to *50micrometers* have been successfully produced and tested for tribological performance [4].

3.2.4 UV Photolithography

There are eight sequences of operation used in this method [32]. The substrate is cleaned at first with acetone and then a layer of adhesive is applied before photoresist is laid by spin coating. Spin coating is done at sufficient speed (3000 RPM at UK) to give a uniform spread of the photoresist layer. Two types of photoresists, positive and negative can be used. With a positive photoresist, the exposed portion is cleared away by the developer solution and the converse holds true for a negative photoresist. Later, the photoresist is softbaked to render it photosensitive before being exposed to a UV light source through a mask, just as done in a LIGA process. UV light source used at UK is of *500-600 nanometers* in wavelength and the exposure time is *45 seconds*. There are three ways by which this process can be done, contact printing, proximity printing and projection printing. At UK, contact printing is used. Subsequently, the specimen goes through a hard baking process to improve the adhesion of the photoresist with the specimen. The final step is electrofabrication. With a positive photoresists, we get positive asperities and with a negative photoresist, we obtain negative asperities.

3.3 SURFACE FINISHING

Thrust bearings such as mechanical seals require flat surfaces for sealing purposes. This is achieved by two material removing machining processes called as lapping and polishing.

3.3.1 Lapping

Lapping is intended to produce a flat surface. In this process, the surface to be lapped is held against another metal plate with a predetermined pressure. A relative motion between these two metallic surfaces is usually given through a rotation of the base plate at a specific speed. Loose abrasives along with a lubricant are pumped onto the machine base plate. The rotation of the base plate leads the abrasives into the sliding interface. If excessive pressures are used to hold the surfaces together, abrasive grains are broken and the metal removing process is rendered ineffective. Similarly, excessive speed tends to impart more centrifugal force to the abrasives and results in inadequate lapping. The lubricant, also called as a vehicle, usually helps in reducing this effect apart from performing its usual functions of lubrication and heat removal. The abrasives need to be harder than the work piece to facilitate metal removal. The size of the abrasives also has an effect on the process. The larger the size, the lesser is the penetration and hence, the lesser the abrasive action. Different types of abrasives are used for different materials, aluminum oxide for softer materials and boron oxide or diamond for harder materials. Similarly, cast iron base plates are used for soft materials and ceramic base plates, for hard materials. The surface finish obtained with lapping is usually in the range of 0.25-1.0 *micrometers*.

3.3.2 Polishing

Once the work piece is lapped, it is kept cleaned and dried before it undergoes polishing. Polishing process further improves the surface finish and gives a reflecting surface required for observing under an optical flat to determine the flatness. Polishing is achieved by rubbing the work piece on polishing paper in a back and forth motion and by applying a moderate pressure, usually by hand. The polishing paper has to be kept clean and free of lint. Selection of appropriate polishing paper is done as per the material hardness and the required surface finish. The flatness of a work piece is determined with the help of an optical flat and a monochromatic light source. One can observe light bands through an optical flat when placed on the polished surface and exposed to monochromatic light source. A formation of parallel light bands indicates a perfectly flat surface. For curved light bands manufacturer's manual may be referred.

3.4 METROLOGY

3.4.1 Optical Microscope

Optical microscope is an indispensable instrument used in the field of metallurgical observation. It offers greater details of a specimen through a better resolution and a higher magnification than what a naked eye provides us. However, the extent of the view, called as the field, is limited both by the area and by the depth. Typically we can get a resolution of $1\mu\text{m}$ instead of $50\mu\text{m}$ as with a naked eye. The overall magnification can be as high as 500 X. and is a product of the magnification of the eyepiece and that of the objective. The eyepiece however does not increase the resolution. Each size of the objective has a different working distance and different area and depth of view.

3.4.2 Electron Microscope

To obtain higher performance than what an optical microscope offers, a scanning electron microscope (SEM) is used. A beam of electrons is impinged on a metallic surface (the specimen) and then, by collecting the reflected electron beam an image is obtained. An SEM can give resolutions as low as 10 nanometers and magnifications as high as 30,000X. The surfaces appear smoother than they actually are, and therefore may lead to false judgments. The constraints in using an SEM are the size and the electrical conductivity of the specimen. The limitation in sample size is posed by the size of the vacuum chamber in which samples are placed. The maximum size of the specimen that can be used at UK is 1.25" (31.75 mm) diameter and 0.5" (12.7mm) height. The surface has to be conductive to avoid building up of electron charge and to deflect the incoming electron beam. Gold coating may be used for non-conductive surfaces or to improve the conductivity. Though the SEM image does not correspond exactly with the optical microscope image, it may be useful to compare images of the same magnification.

Secondary X-rays are produced with the interaction of electrons and the specimen. SEMs are usually equipped with energy dispersive X-ray analysis instrumentation (EDAX) to monitor the secondary X-rays for identifying the elements present on the surface of the specimen. This can be useful in tribological studies. Figure (14) is an SEM picture of a hexagonal microstructure that shows the accuracy of the produced geometry. White patches in the groove are the traces of solvent remained due to incompleteness of drying up process.



Figure 14: SEM details of an asperity groove [1]

3.4.3 Optical Interferometer

Surface roughness measurements have been traditionally achieved by using stylus profilometry. A three-dimensional surface profile is also obtained by stitching together multiple samples of two-dimensional profiles. With the advances in optical interferometry, it is now possible to obtain a 3-D image with a single exposure and a superior resolution. NewView 5000®, possessed by our lab, gives a *1 angstrom* resolution over vertical distances upto 5mm, lateral resolution up to 1.18μm and large fields of view up to 14mm. A wealth of information regarding this instrument is contained in the user's manual.

Chapter IV: MODELING

4.1 INTRODUCTION

4.1.1 Hydrodynamic Theory

The presence of a viscous fluid film such as lubricating oil, in between any two sliding solid surfaces is known to reduce frictional resistance and wear occurring at their surfaces. Apart from carrying away a major portion of the heat generated by friction, it also supports a part of the normal load. Design of hydrodynamic bearings such as thrust and journal bearings is carried out to ensure the presence of a fluid film. In non-conformal bearings, for example, gears and rolling bearing elements, elastic distortion of metal gives rise to the development of a fluid film. In machine tool slide ways a wedge is produced by the thermal distortion of metals to provide space for lubricant. In all these cases the fluid film may not carry the full load, but it relieves the metal of carrying most of it. The rest of the load is carried by the metal-to-metal asperity contacts. Generally, a convergent wedge along with speed and viscosity produces fluid film pressure.

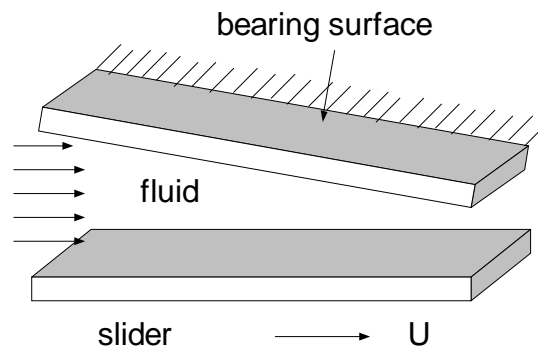


Figure 15: Convergent wedge [25]

Additives in lubricant, those have high endurance to extreme conditions created by temperature, help in forming a protective layer of surface-active molecules and thus prevent the chance of welding of asperities that can lead to the breakdown of the system. In fluid film lubrication, a very thin layer of fluid separates the two sliding surfaces completely, preventing the asperity contacts. Therefore, the frictional resistance to the motion is reduced to the level of shear forces experienced by the fluid. In order to support a normal load, pressures have to be developed in this fluid film. In hydrostatic lubrication, the lubricant is pressurized externally to achieve this. But, in boundary lubrication, the sliding faces are not completely separated and so wear takes place at the contacting points. An example of such type of lubrication is the operation of low speed bearings that are small in size. In comparison, with hydrodynamic or thick film lubrication, pressure is developed internally by the combined action of speed of the moving surfaces and the viscosity of the lubricant. If the surfaces are smooth and parallel, no pressures are developed and if irregularities are present on the surfaces, pressures are formed in the fluid film. The mechanism of this type of lubrication can be better understood by studying the action of a converging wedge of sliding surfaces on an interfacial fluid film (see figure 15). Convergence of a fluid film is formed either due to natural profile of asperities and surfaces or

due to created profiles, as in the case of thermal distortion. Such converging wedge occurs in every lubricated pair of materials and produces pressure proportional to the viscosity and the sliding speed. As a result, the lubricated sliding pair carries a certain load.

4.1.2 Velocity Distribution

Figure (16) illustrates the action of a moving surface dragging viscous oil into converging zone that can be classified as a Couette flow. Since oil is virtually incompressible, and as it moves progressively into lesser space, it builds up pressure and finally falls to the ambient pressure at the exit. Hence, at the entry, the positive pressure gradient limits the inward flow by forcing the velocity profile to be concave. Once the oil passes beyond the point of maximum pressure, negative pressure gradient boosts the flow out through the reduced space at the end of the converging section. Hence, at the exit, the velocity profile is convex. At an intermediate point, the velocity profile is linear and it is where the pressure gradient is zero. Velocity distribution in the transverse direction is due to the pressure gradients only. If the inclination angle is increased, zero or negative velocity of flow at the fluid surface may develop near the entrance, thus initiating a reverse flow or separation. Further, if viscosity of the lubricant is less, this may even cause eddy or vortex formation.

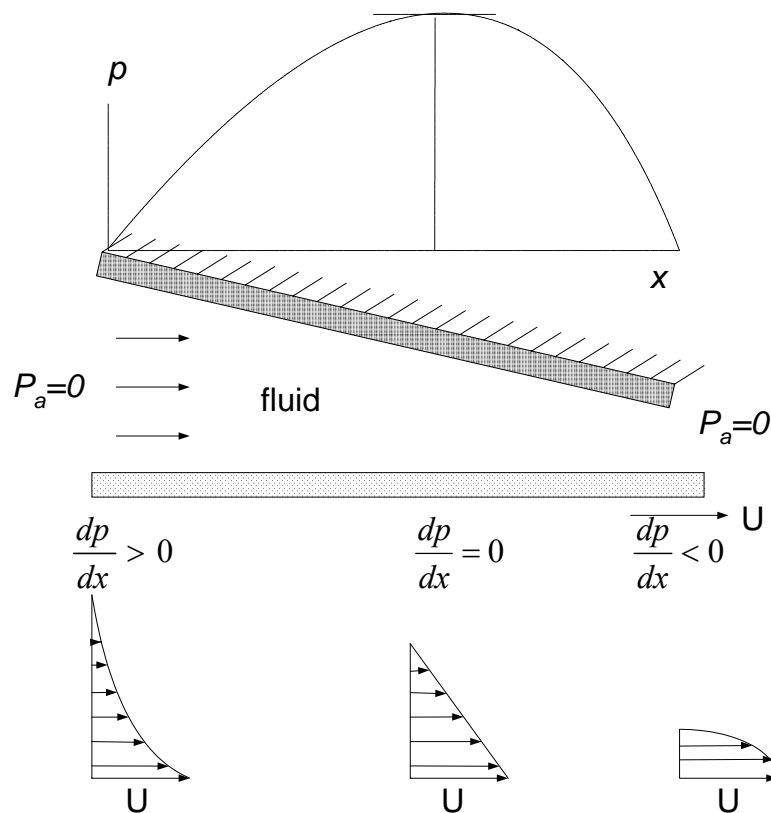


Figure 16: Velocity distribution [22]

The phenomenon of converging wedge action forms the basis for the hydrodynamic theory of lubrication. Generally, high speeds and light loads characterize hydrodynamic lubrication whereas low speeds and heavy loads define thin film lubrication. Both

these types may occur in the same bearing at different times, thin film while starting or stopping of the relative movement of two interacting surfaces, and a fluid friction (thick film) when the moving member has reached a speed (critical speed) sufficient to maintain a thick film.

4.1.3 Steady State Reynolds Equation

The mathematical expressions for hydrodynamic conditions are given by the Reynolds equation (8), as given below this paragraph. In simplifying the derivation of a mathematical expression, the following assumptions are made:

- The surfaces are considered to be smooth.
- The curvature of the surfaces is large compared to film thickness.
- The fluid flow is laminar.
- There is no slip at the boundaries.
- Body and inertia forces are neglected.
- The lubricant is Newtonian.
- Pressure is constant across the thin film.

Steady state Reynolds equation is developed by applying the continuity of flow and equilibrium of forces on a representative fluid element. The generalized expression is presented as,

$$\frac{\partial}{\partial x} \left(\frac{\rho h^3}{\mu} \frac{\partial p}{\partial x} \right) + \frac{\partial}{\partial y} \left(\frac{\rho h^3}{\mu} \frac{\partial p}{\partial y} \right) = \underbrace{6(U_1 - U_2)}_{\text{WedgeTerm}} \frac{\partial(\rho h)}{\partial x} + \underbrace{6\rho h \frac{\partial(U_1 + U_2)}{\partial x}}_{\text{StretchTerm}} + 12 \underbrace{\frac{\partial(\rho h)}{\partial t}}_{\text{SqueezeTerm}} \quad (8)$$

where U_1 and U_2 are velocities of the moving surfaces.

The physical significance of Reynolds Equation is that the pressure generation in the fluid film is given as a composition of the wedge, stretch and squeeze contributions to the load support. The wedge effect is dependent on the variation of film thickness in the direction of the velocity. The stretch effect is caused due to the variation in the velocities of the moving surfaces as in the case of elastomeric surfaces. When rigid surfaces are considered for lubrication, stretch terms are of no significance. Finally, the squeeze effect is due to the impact or vibration of the surfaces relative to each other.

For rigid surfaces, if one of the sliding pairs is considered stationary and the other moving with a velocity, U and if density (ρ) and viscosity (μ) variations across the thin lubricant film are ignored (as a reasonable assumption), the above equation can be further simplified to

$$\frac{\partial}{\partial x} \left(h^3 \frac{\partial p}{\partial x} \right) + \frac{\partial}{\partial y} \left(h^3 \frac{\partial p}{\partial y} \right) = 6\mu U \frac{\partial h}{\partial x} + 12\mu V \quad (9)$$

where V is the vertical velocity of sliding surfaces relative to each other. If squeeze effects are absent, then the above equation reduces to

$$\frac{\partial}{\partial x} \left(h^3 \frac{\partial p}{\partial x} \right) + \frac{\partial}{\partial y} \left(h^3 \frac{\partial p}{\partial y} \right) = 6\mu U \frac{\partial h}{\partial x} \quad (10)$$

This is the well-known Reynolds equation in two dimensions that is generally referred in most literature. Appendix A.3 shows a derivation of equation (10).

4.1.4 Microasperity Lubrication

Surfaces in reality are not smooth, as considered in the lubrication theory earlier. Irregularities are present in the form of surface roughness on the interfacial surfaces at microscopic levels. The generation of pressure in a fluid film due to the converging and diverging wedges of micro irregularities is classified as microasperity lubrication and experimental evidence has been presented in support of this theory [5].

The theory of microasperity lubrication can be better understood by an idealized one-dimensional model of a single irregularity. As an example, figure (17) shows a rectangular model paired with a flat slider in one dimension, in the presence of a fluid film. The moving surface produces antisymmetric pressure distribution around a single asperity. Positive pressure is developed towards the converging edge and negative in the diverging region. Since the load support is zero for an antisymmetric pressure distribution, as is evident by the resulting net area under the graph, there would be no generation of thrust.

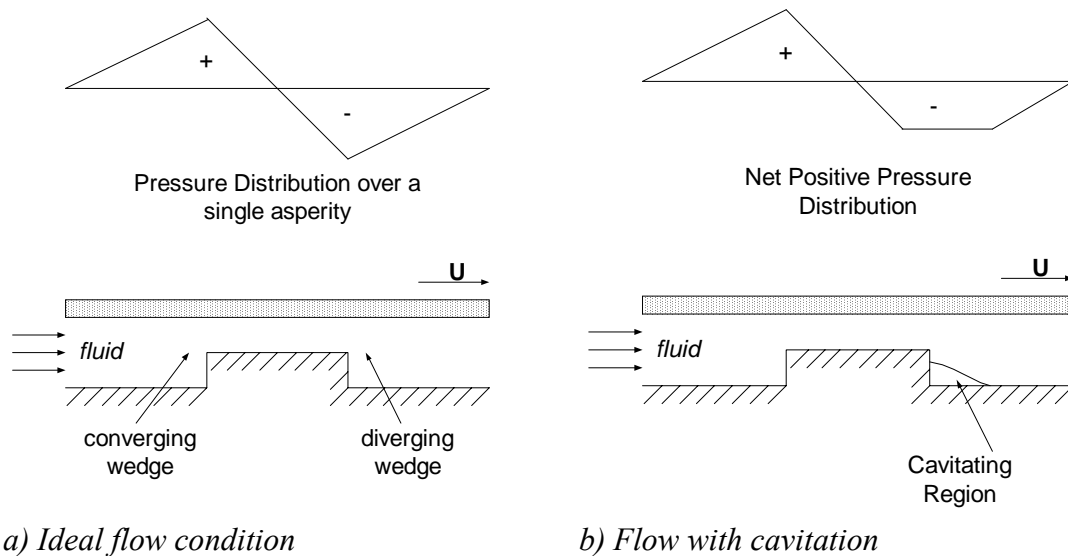


Figure 17: Couette flow over idealized asperity [5]

This contradiction to the experimental evidence is explained by the presence of a phenomenon known as cavitation, in the negative pressure zone of the lubricant [5]. Two types of cavitation in lubricants are generally observed. The first one, known as gaseous cavitation (in which gaseous bubbles are emanated by the lubricant when saturation pressures of dissolved gases are reached) is commonly found in bearings. The saturation pressures are generally near to the atmospheric pressure. Pure lubricants are generally free of dissolved gases, but most of the available lubricants are rarely pure. The second type called as vapor cavitation (in which liquid starts boiling when the pressure acting on it falls below the vapor pressure) is prevalent in hydraulic machinery. Due to the inability to withstand tensile forces, lubricant breaks up into a cavitating region and a fluid flowing path. In the cavitating negative pressure region, isobaric pressure conditions prevail and thus, the net area under the graph as shown in figure (17-b) is no more zero, but positive. The integrated effect of the net positive pressure distribution of all the asperities on a sealing surface explains for the creation of thrust and hence, the otherwise mating surfaces tend to separate.

4.1.5 Cavitation

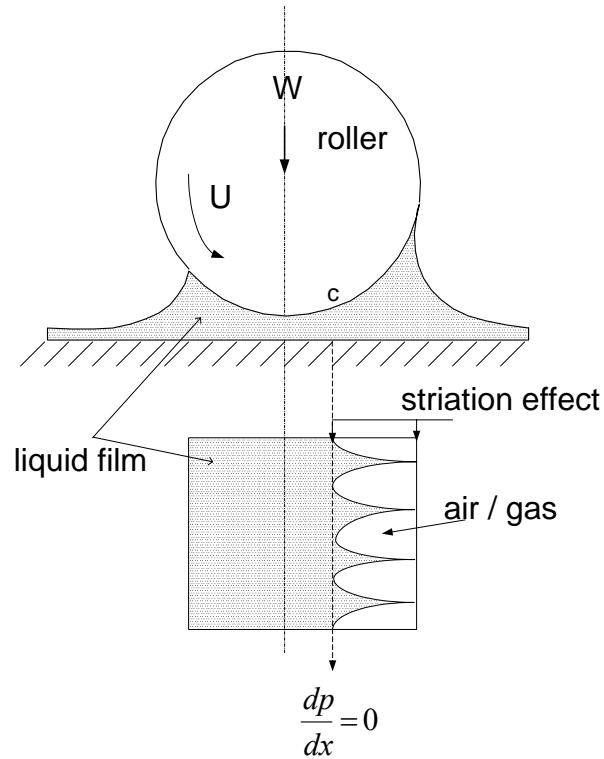


Figure 18: Cavitation with rolling [22]

A variety of reasons were presented to explain the hydrodynamic effects in thrust seals, including the effect of non-parallel surfaces, axial seal vibration, variable lubricant properties and inertial effects [23]. In all these cases, hydrodynamic pressures were greater than the hydrostatic pressures. Lack of accurate measurement tools during earlier times hindered the verification of the contribution of viscosity and hence attention was given to cavitation as a means of explaining the hydrodynamic effects.

As explained earlier, when a lubricant is subjected to negative pressures the dissolved gases get liberated at their saturated vapor pressures or cavitation pressures, P_c . The illustration provided in figure (18) helps us understanding cavitation visually. This figure shows the action of a rolling cylinder on a flat surface with a liquid film in between. As the roller drags the liquid at the entrance, it passes through progressively contracting space until it reaches the mid point. Thereafter, it finds gradual expansion in space for incoming flow to occupy and hence, the increase in film thickness above the original level is compensated by a reduction in the effective width of the lubricant as is seen in the striation zone. It is the surface tension effect that helps the liquid split into streams and leave space for cavitation. At the point of separation, c , both the pressure and its gradient are zero. Accordingly, upstream cavitation boundary conditions, also called as Swift-Steiber condition, are given as:

$$p = P_c \quad \text{and} \quad \frac{\partial p}{\partial n} = 0 \quad (11)$$

In reality, to preserve the continuity of mass, the lubricant is expected to join again at a point further down, where the boundary condition (downstream), also called as Jakobsson condition, is given as:

$$\frac{h^2}{12\mu} \frac{\partial p}{\partial n} = \frac{U_n}{2} (1 - \theta_n) \quad (12)$$

where θ is the fraction of the cavitating zone occupied by lubricant striations stretching between the moving and the stationary surfaces. The void region is given by $(1 - \theta)$. The subscript, n , refers to the distance normal to the interface. This second condition is generally not used in a numerical solution due to the difficulty experienced in programming, in order to obtain the interface loci between computation grid points and to evaluate the required pressure gradient.

4.1.6 Mechanisms of Hydrodynamic Load Support

Load support with hydrodynamic lubrication can be achieved both by smooth and rough surfaces. Some of the familiar mechanisms of load support are given below.

4.1.6.1 Smooth Surfaces

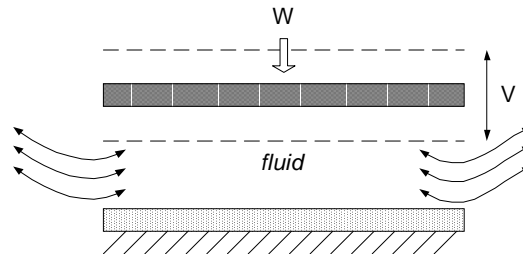


Figure 19: Squeeze effects [22]

In case of smooth surfaces, the load support mechanism is caused by three different phenomenon of the wedge, stretch and squeeze effects (as shown in figure-19). Stretch effects are found in the case of sliding tires. In case of a plain slider bearing with at least one elastomer surface, wedge and stretch effects are observed. In a journal bearing, wedge and squeeze effects are found.

4.1.6.2 Rough Surfaces

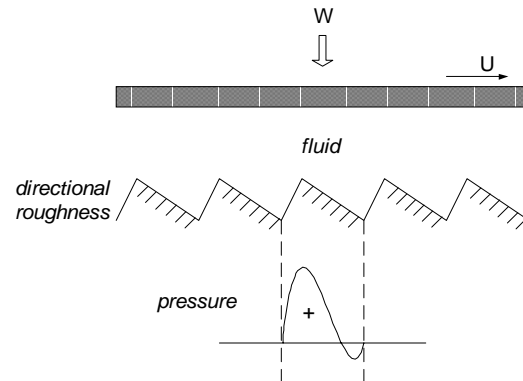


Figure 20: Directional roughness [22]

There are four different phenomenon of load support mechanisms associated with rough surfaces [22]. In one of the mechanisms, roughness aligned in one particular direction generates more positive pressure zones than the negative ones and as a result, net load support is observed (figure-20). Another mechanism is due to the combined effects of pressure and temperature. While pressure increases the viscosity and hence the load support, temperature has a reverse effect. These effects are assumed to be negligible in the thrust slider system used for this study. The other two mechanisms of load support due to net positive pressure effects are those commonly found with cavitation (as explained earlier) and elastohydrodynamic effects as shown in figure (21). Elastohydrodynamic lubrication occurs when at least one of the surfaces is elastic. Even rigid bodies when subjected to very high pressures (in order of thousands of *psi*) as in the case of non conformal bearings (for e.g. roller bearings) undergo plastic deformation. As shown in the figure, due to deflection of the asperity a shift in the pressure profile occurs leading to the formation of a net positive pressure.

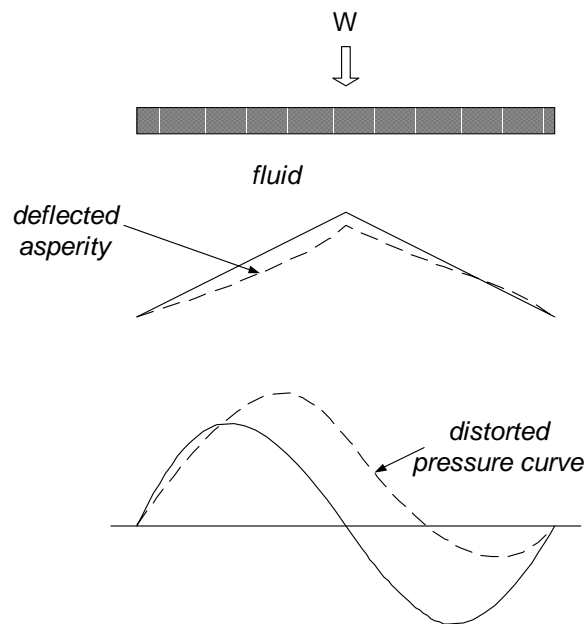


Figure 21: Elastohydrodynamic effects [22]

4.1.6.3 Spiral Grooves

Spiral shaped grooves, commonly found in centrifugal pumps, are used in conjunction with a sealing dam to produce both hydrostatic and hydrodynamic pressures on a sealing face [21]. These spiral grooves are recessed into the sealing surface, typically onto a stator, all around in the circumferential direction. Due to rotation, lubricant is pumped in between the mating faces in a radial direction leading to the generation of pressure. This helps in the separation of the faces even in the absence of an external hydrostatic pressure. Tangential velocity also produces hydrodynamic pressure due to variation of film thickness in the circumferential direction. Spiral grooves can be designed to provide either upstream or downstream pumping.

4.1.6.4 Radial Grooves

A radial groove when used in combination with a sealing dam on the thrust surface such as a seal, gives both hydrostatic and hydrodynamic pressures. The sealing dam contributes to the hydrostatic pressure and the hydrodynamic pressure is generated due to the alternative grooves and lands that are present all around the circumference towards the outside diameter of the thrust face. Unlike the spiral groove type of design, this has a bi-directional capability due to its circumferential symmetry [12].

4.1.6.5 Wavy-Tilt Dam:

This type of design has similarities with the radial groove pattern except that, instead of radial grooves waviness is produced by grinding the surface in the tangential direction. The waviness contributes to hydrodynamic support due to the effect of rotation. Due to the created radial taper, hydrostatic pressure is generated, just as found in a uniformly convergent tapered seal. The presence of a sealing dam also minimizes the leakage [11].

4.1.6.6 Macro Roughness

Macro roughness is a surface undulation with relatively long wavelengths when compared to micro irregularities. It is caused due to machining vibrations, tool chatter and feed. As in the case of microstructures, macro roughness also generates hydrodynamic pressures due to the action of converging and diverging wedge of waviness in the circumferential direction [18].

4.1.6.7 Temperature effects

When temperature gradients are present, lubricating film experiences thermal expansion. As a result, a velocity distribution similar to that found in a normal convergent wedge forms, and hydrodynamic effects are experienced. The magnitude of thrust produced is found to be comparable to that of a tilting pad bearing [17]. Though no direct measurements were made in the referred paper, the existence of a viscous pressure film between the surfaces was assumed based on certain observations such as the absence of striations on the thrust surfaces, the extent of load carried and the reduced frictional torque.

4.1.6.8 Miscellaneous Effects

Apart from the mechanisms mentioned above, other factors such as wobble, bounce, waviness, warpage, eccentric rotation and non-Newtonian lubricants are also found to produce hydrodynamic effects [5].

4.2 ANALYTICAL SOLUTIONS

As explained earlier, a convergent wedge is required to generate a positive hydrodynamic pressure. The exact shape of the wedge between the entry and the exit is inconsequential. It is the ratio of the film thickness at the entry and the exit that plays an important role in the determination of pressure generation in a slider bearing [25]. In the following examples, a step slider is chosen due to its familiarity and the simplicity of mathematical expressions it gives, in providing the required understanding.

4.2.1 One Dimensional Step Slider Solution

4.2.1.1 Positive Step Slider

Figure (22) shows a positive type, one dimensional convergent step slider bearing that can also be viewed as a two-dimensional infinitely long bearing. This model is also called as Rayleigh Step bearing.

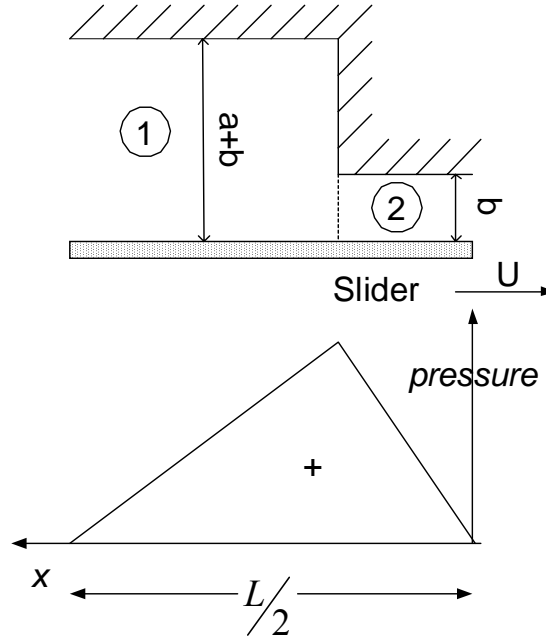


Figure 22: Rayleigh step bearing

The above figure shows point b taken as origin. The variables $L/2$, R_0 , $(a+b)$ and b indicate the total length of the slider, length of the step, maximum film thickness and minimum film thickness respectively. The difference between film thicknesses gives the height of the step, a .

Since viscosity and density are taken as constant, the relevant Reynolds equation in the absence of stretch and squeeze effects is given as per equation (10) and is expressed as:

$$\frac{\partial}{\partial x} \left(h^3 \frac{\partial p}{\partial x} \right) + \frac{\partial}{\partial y} \left(h^3 \frac{\partial p}{\partial y} \right) = 6\mu U \frac{\partial h}{\partial x} \quad (13)$$

Since the problem is one dimensional, this equation reduces to

$$\frac{d}{dx} \left(h^3 \frac{dp}{dx} \right) = 6\mu U \frac{dh}{dx} \quad (14)$$

By dividing the fluid element into two regions, 1 and 2, of constant film thickness, as illustrated above, equation (14) can be further simplified as

$$\frac{d^2 p}{dx^2} = 0 \quad (15)$$

which is valid in both the regions.

In such a case, appropriate boundary conditions are given as:

- Pressure, p is zero at either ends; $p_1=p_2=0$ @ $x=-L/2$ and 0 .
- Pressures in both the regions are equal at their common boundary; $p_1=p_2$ @ $x=-R_0$
- Flow is continuous at the common boundary; $q_1=q_2$

where, rate of flow per unit width, q_x , is given as per the equation,

$$q_x = -\frac{h^3}{12\mu} \frac{dp}{dx} + \frac{h}{2} U \quad (16)$$

The general solution to equation (15) is given as:

$$p = ax + b \quad (17)$$

When applied to both the regions, it yields two equations:

$$p_1 = c_1 x + c_2 \text{ and}$$

$$p_2 = c_3 x + c_4$$

Applying the boundary conditions to these two equations, gives the following expressions for constants

$$c_1 = \frac{6\mu U a R_0}{(a+b)^3 R_0 + b^3 (L/2 - R_0)} \quad ;$$

$$c_2 = c_1 L/2$$

$$c_3 = \frac{-6\mu U a (L/2 - R_0)}{(a+b)^3 R_0 + b^3 (L/2 - R_0)}, \quad \text{and}$$

$$c_4 = 0$$

The final solution for pressure in each region is given as

$$p_1 = \frac{6\mu U a R_0}{(a+b)^3 R_0 + b^3 (L/2 - R_0)} (x + L/2) \quad (18)$$

$$p_2 = \frac{-6\mu U a (L/2 - R_0)}{(a+b)^3 R_0 + b^3 (L/2 - R_0)} x \quad (19)$$

And, the related pressure distribution curve is also given in figure (22)

4.2.1.2 Negative Step Slider

Details of the geometry for this type of a slider are shown in figure (23). The fluid element is once again divided into two regions. Hence, Reynolds equation as expressed in equation (15) and the associated boundary conditions are also applicable to this situation. Solving the equations yield different expressions for constants that are given as:

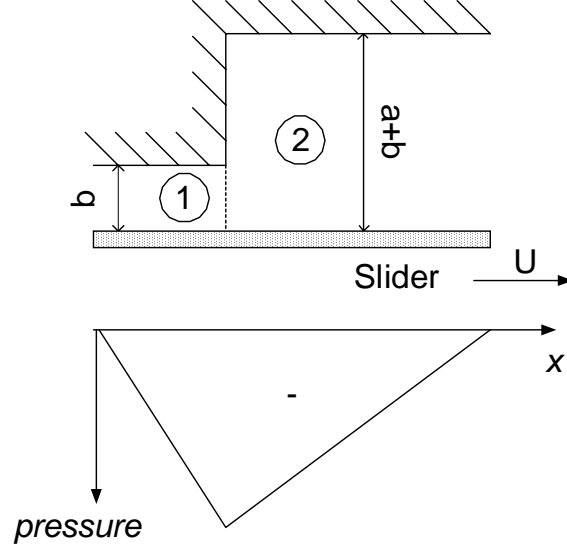


Figure 23: Negative step slider

$$c_1 = \frac{-6\mu U a R_0}{b^3 R_0 + (a+b)^3 (L/2 - R_0)}$$

$$c_2 = c_1 L/2$$

$$c_3 = \frac{6\mu U a (L/2 - R_0)}{b^3 R_0 + (a+b)^3 (L/2 - R_0)}, \text{ and}$$

$$c_4 = 0$$

Accordingly, the solution to pressures in region 1 and 2 are given below

$$p_1 = \frac{-6\mu U a R_0}{b^3 R_0 + (a+b)^3 (L/2 - R_0)} (x + R_1) \quad (20)$$

$$p_2 = \frac{6\mu U a (L/2 - R_0)}{b^3 R_0 + (a+b)^3 (L/2 - R_0)} x \quad (21)$$

Pressure distribution is also given in figure (23). If the negative pressures are large, lubricant breaks down into streamers as mentioned earlier.

4.2.2 Boundary Conditions

4.2.2.1 Full Sommerfeld

By combining a converging wedge back to back with itself a converging-diverging wedge is formed. Two such examples are shown in figure (24). The first is an extension of a Rayleigh Step bearing and the second is the shape found generally in a journal bearing. Positive pressures are generated in the converging region and negative in the diverging region, giving an anti-symmetrical pressure distribution. Pressure boundary conditions at the entry, exit and the center of the wedge are each equal to zero and these conditions are known as Full Sommerfeld

conditions. The resulting pressure curve is shown in figure (24-c&d). For low supply pressures, P_s , Reynolds equation predicts negative pressures that lead to erroneous results in load capacity [29].

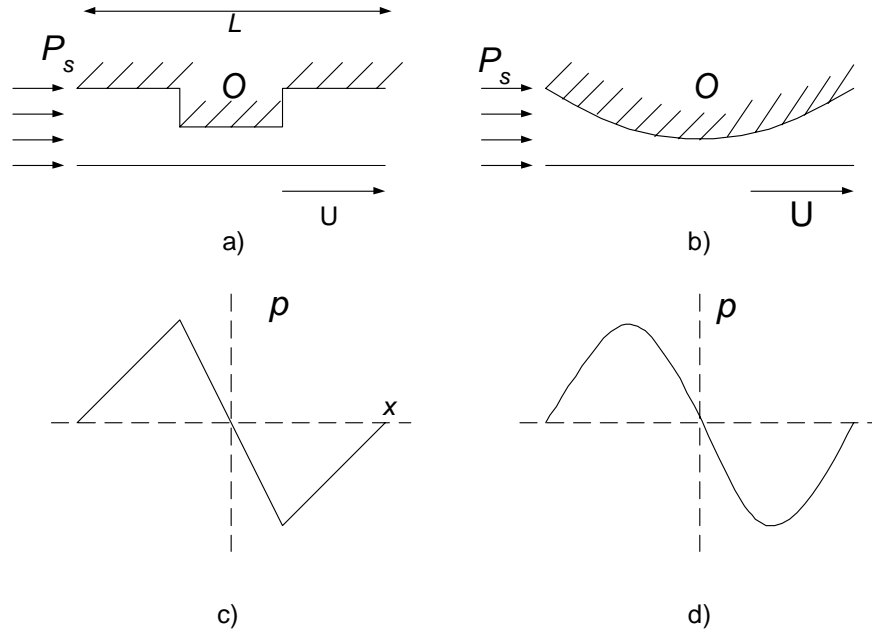


Figure 24: Full Sommerfeld pressure distribution

Load carrying capacity is given as:

$$W = \int_{-L/2}^{L/2} p dx \quad (22)$$

For a full Sommerfeld condition, continuity of flow can be easily obtained by using equation (16) given earlier.

4.2.2.2 Half Sommerfeld

This condition assumes that cavitation occurs over the entire diverging region and hence pressures are considered to be completely and continuously zero in the negative zone. However, this condition is rejected based on the continuity of flow. At a point O'' where the pressure gradient is zero, the flow rate is given as per the expression, $q_x = \frac{Uh''}{2}$ and this is the incoming flow at the center of the thrust pad. The flow to the immediate right side of this center is also equal to $q_x = \frac{Ub}{2}$ since both pressure and pressure gradient are equal to zero according to the boundary conditions. Hence, this difference, $\frac{U(h''-b)}{2}$ in flow rate violates the continuity equation and consequently half Sommerfeld condition is rejected. A typical pressure profile is shown in figure (25-b).

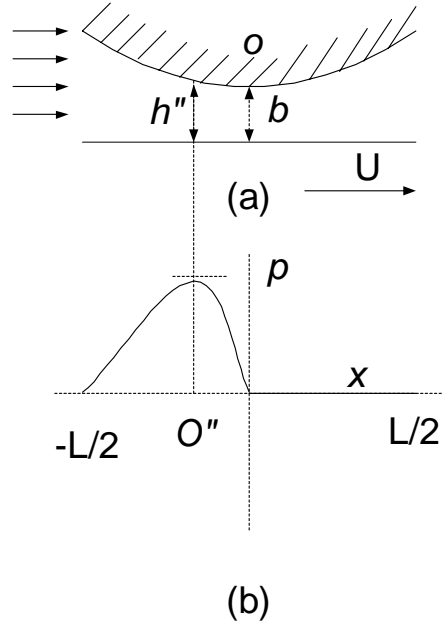


Figure 25: Half Sommerfeld pressure distribution [29]

Load carrying capacity is given as:

$$W = \int_{-L/2}^0 p dx \quad (23)$$

4.2.2.3 Reynolds Condition

While Half Sommerfeld condition treats the entire diverging region as cavitating, Reynolds condition assumes that pressure and its gradient fall to a zero value, at an intermediate point, O' , in the diverging region instead of the center. This assumption is found to be more accurate and is widely used in literature now, especially in the two dimensional numerical solutions, as it is easy to implement it. The resulting load capacity is generally found to be 40% more than its value obtained by half Sommerfeld condition.

At O' , the flow rate is given as

$$q_x = \frac{Uh'}{2}$$

Beyond this point, since the gap is increasing, all incoming flow is accommodated and hence continuity of flow is maintained [25]. The pressure profile is shown in dotted line in the same figure (26-b). Load carrying capacity is given as:

$$W = \int_{-L/2}^{O'} p dx \quad (24)$$

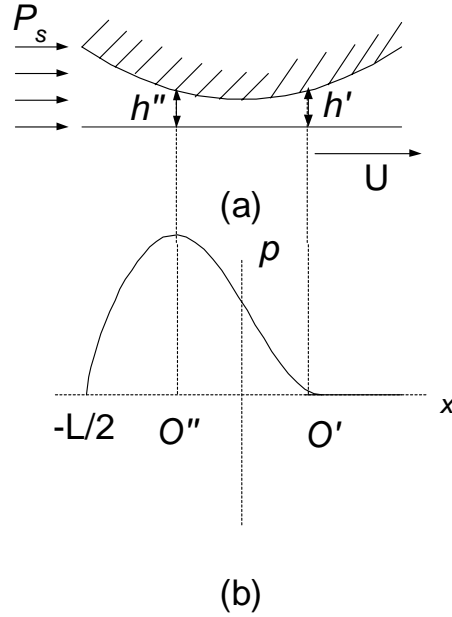


Figure 26: Reynolds pressure distribution [25]

4.2.3 Two Dimensional Models

All real applications are two dimensional in nature, whether it is a journal bearing, a Michel pad bearing or any other similar type of a thrust surface. Rarely do we find analytical solutions to such two dimensional problems in literature and it is because of the difficulty experienced in evaluating integration of expressions. Traditionally such problems have been made tractable by considering bearings as either infinitely long or infinitely short, thus reducing the problem to merely a single dimension. There is a lesser-used method known as axial approximation that incorporates a second dimension in its solution despite simplifying the problem to one dimension [29]. However, one needs to check the accuracy of using such a method before using it. In some other solution methods, certain approximations have been made, in finding a closed form solution. However, numerical approach is the most predominant method used in finding solutions to two-dimensional problems because of the simplicity and the acceptable accuracy. Before dealing with this procedure, an overview of different types of asperity shapes considered in this thesis and a two-dimensional analytical solution for a hexagonal layout is given below.

4.2.4 Arrays, Geometries and Orientation

In microasperity lubrication, improvement in tribological performance depends upon the viscosity of the lubricant, the relative velocity of the moving surfaces and the geometries of both the micro asperities and the thrust bearing. Generally, for a given situation, the applied load, the viscosity (ignoring the temperature effects), velocity and the dimensions of the thrust bearing are constant. The parameters then available for a designer to enhance the friction and leakage performance are, the micro asperity shapes. The term, ‘shapes’, is used in a generic sense to encompass the associated parameters such as arrays, geometries, asperity types, (positive and negative), size and orientation. An array refers to the way asperities are distributed in a layout. The most common array shapes are square, hexagonal and radial as shown in figure (27).

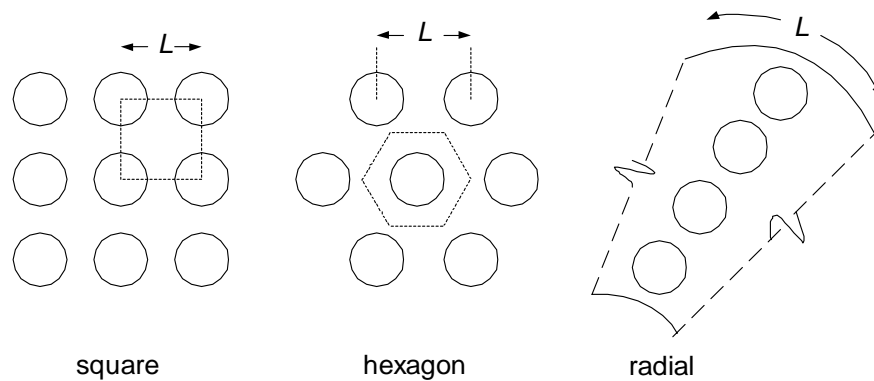


Figure 27: Types of arrays

In each such array, different geometries of asperities can be used. Some of the common geometries are shown in figure (28)

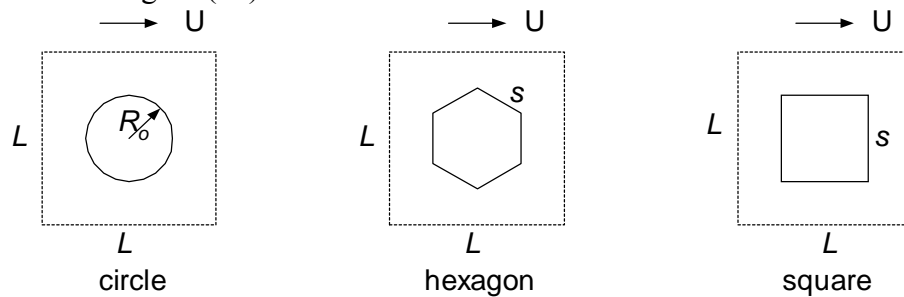


Figure 28: Types of asperity geometries

Orientation refers to the way an asperity is placed in an array. This is shown in figure (29). In the case as a circle, it is evident that the shape is independent of the orientation. Hence, no differences in hydrodynamic effects are expected.

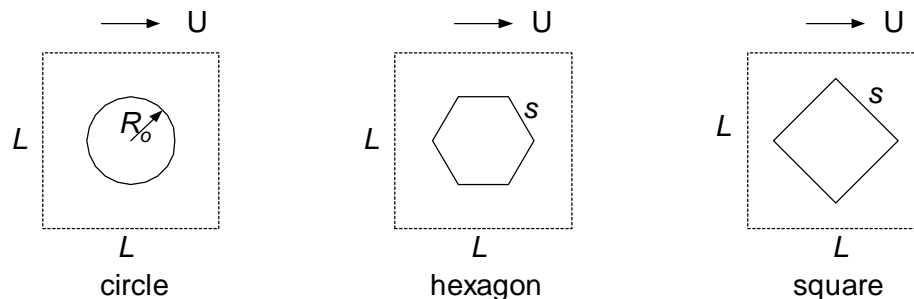


Figure 29: Orientations of asperities

4.2.5 Solution to a Two Dimensional Model

Cylindrical asperities in a hexagonal layout, as illustrated in figure (30), have been investigated in reference [5]. A brief description of the solution process is given here.

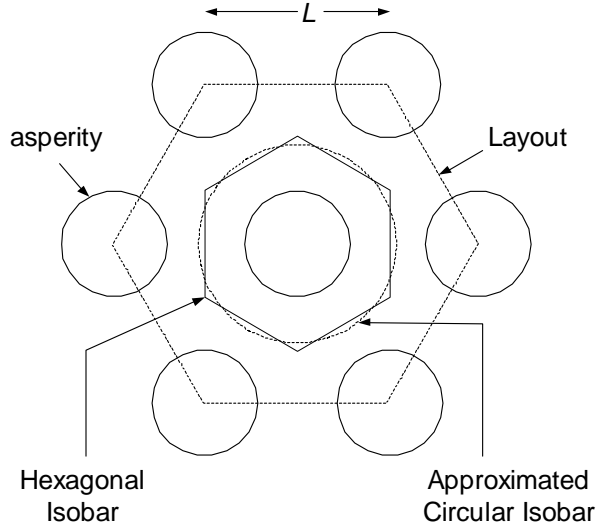


Figure 30: Hexagonal asperity layout

As shown in figure (31), the film thickness equation in cylindrical coordinates for two regions, one over the asperity and the other in the grooves, is given as

$$h(r) = \begin{cases} b, & r < R_0 \\ a+b, & R_0 \leq r \leq L/2 \end{cases}$$

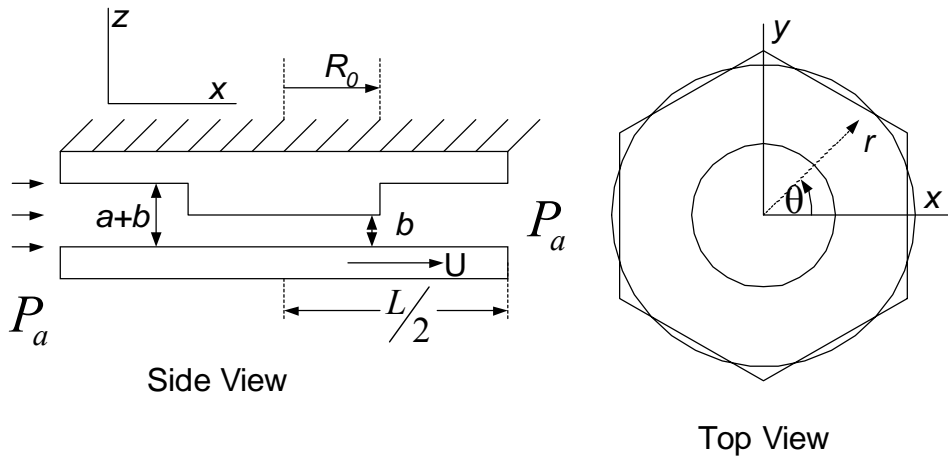


Figure 31: Unit cell sliding system

Since film thickness is constant in each of the regions, Reynolds equation, in cylindrical coordinates, for each of these regions reduces to the Laplacian:

$$\frac{\partial}{\partial r} r \frac{\partial p}{\partial r} + \frac{1}{r} \frac{\partial^2 p}{\partial \theta^2} = 0 \quad (25)$$

Radial flow rate is given as

$$q_r = \left[-\frac{h^3(r)}{12\mu} \frac{\partial p}{\partial r} + \frac{Uh(r)}{2} \right] \cos \theta \quad (26)$$

The boundary conditions are as follows.

- p is bounded at the origin
- $p \rightarrow 0$ as $r \rightarrow \infty$
- Radial flow rate at the boundary of regions I & II is continuous
- Pressures at the boundary of regions I & II are equal
- Pressure is periodic in the angular direction, implying $p(r, \theta) = p(r, \theta + 2\pi)$ and,
- $\frac{\partial p(r, \theta^+)}{\partial \theta} = \frac{\partial p(r, \theta^-)}{\partial \theta}$

The solution to equation (25) is:

$$p = -\left(\frac{6\mu Uar}{b^3 + \gamma(a+b)^3}\right) \cos\theta + P_a \quad \text{for } 0 \leq r \leq R_0 \quad (27)$$

$$p = -\left(\frac{6\mu UaR_0^2}{b^3 + \gamma(a+b)^3} \frac{\left(\frac{L}{2}\right)^2 - r^2}{r\left(\left(\frac{L}{2}\right)^2 - R_0^2\right)}\right) \cos\theta + P_a \quad \text{for } R_0 \leq r \leq \frac{L}{2} \quad (28)$$

where the variable γ is given as

$$\gamma = \frac{1+b^2}{1-b^2}$$

A typical pressure distribution graph for a 2-D cylindrical asperity for a hexagonal layout approximated by a circular array is given in figure (32).

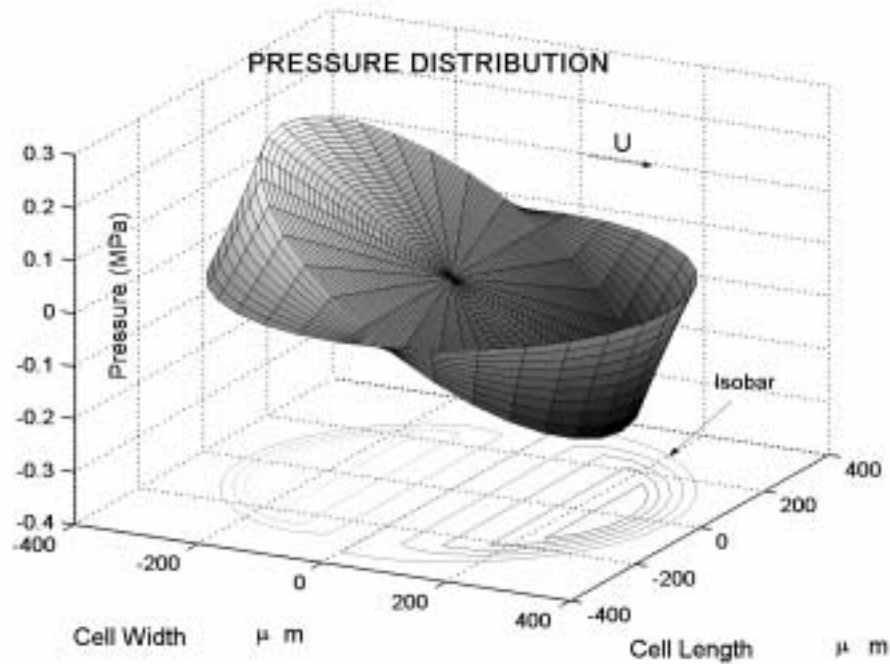


Figure 32: A 2-D full Sommerfeld pressure distribution

And the load support is given by the equation,

$$W = \int_0^{2\pi R_1} \int_0^0 p r dr d\theta \quad (29)$$

4.2.6 Coefficient of Friction

Coefficient of friction is not only influenced both by the asperity tops and the grooves in between, but also by their surface roughness. By lapping the asperity tops, the effect of latter is reduced, but the surface roughness in the grooves that is not accessible to machining processes has its own effect on friction. It can be statistically quantified and is left open for future studies.

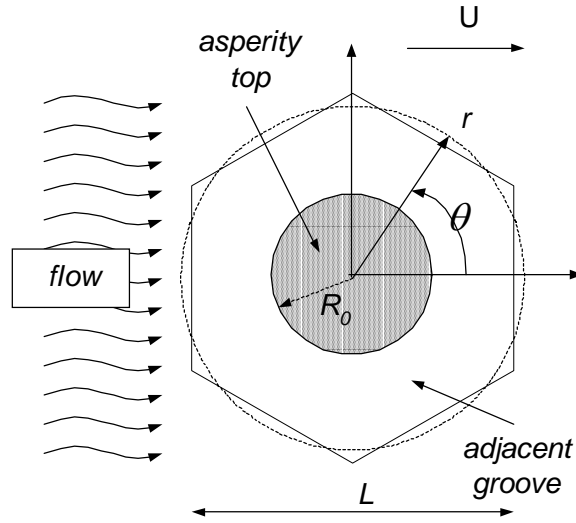


Figure 33: Shear flow on a unit cell

Each region of constant film thickness the surfaces are plane, shear stress is expressed as

$$\tau(x, y) = \mu \frac{\partial u}{\partial z} \quad \text{where} \quad (30)$$

$$\frac{\partial u}{\partial z} = \frac{1}{\mu} \frac{\partial p}{\partial x} \left(z - \frac{h}{2} \right) + \frac{U}{h} \quad (31)$$

(see appendix equation (a.8) for details). Friction force considered here can be expressed as a sum of the shear effects on asperity tops and grooves and also due to the pressure gradients acting on the surfaces (see figure 33). In Cartesian coordinates it is given as:

$$F = \int_{-L/2}^{L/2} \int_{-L/2}^{L/2} \tau dx dy \quad (32)$$

Substituting equations (30 & 31) into the above equation and dividing by the area of each asperity, L^2 the above equation gives average shear stress

$$\tau_{avg} = \mu U \left(\frac{\delta^2}{b} + \frac{(1-\delta^2)}{(a+b)} \right) + \frac{1}{L^2} \int_{-L/2}^{L/2} \int_{-L/2}^{L/2} \frac{\partial p}{\partial x} \frac{h}{2} dx dy \quad (33)$$

This formula holds true for other geometries as well. The second term in the above equation is the contribution by the pressure gradients. And, finally coefficient of friction is given as

$$f = \frac{F}{W} = \frac{\tau_{avg.}}{P_{avg.}}; \quad (34)$$

4.2.7 Leakage (based on Poiseuille Flow)

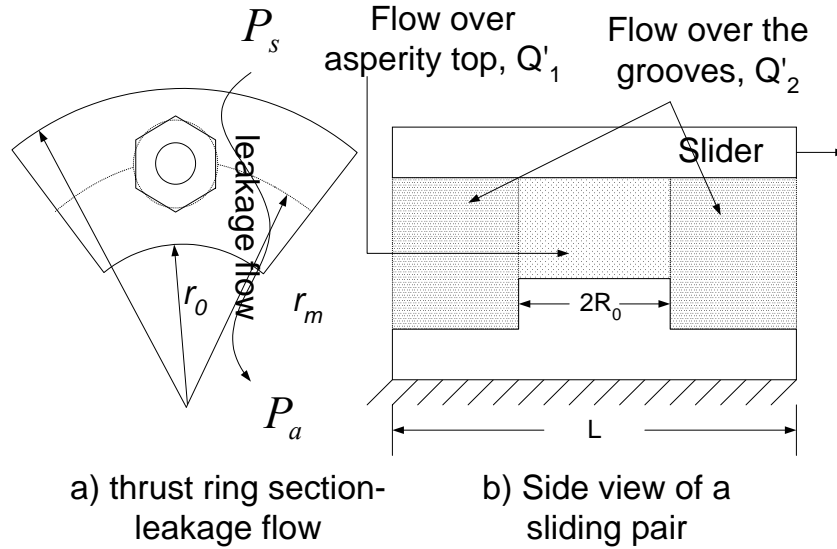


Figure 34: Leakage paths for a positive asperity

Leakage occurs in the radial direction and is governed by the well-known Poiseuille's law given as;

$$Q = \frac{h^3 \Delta p (2\pi r_m)}{12\mu(r_1 - r_0)} \quad (35)$$

where Δp is the hydrostatic pressure difference across one unit cell [7]. Though this formula for leakage is in its simplified form, since other effects such as rotation and surface tension are not considered [7], a reasonable estimate of leakage can be expected, good enough for comparative studies.

Figure (34) shows the leakage path for each unit cell, which is a fraction of its length (L) to the circumference ($2\pi r_m$). For simplifying the calculations, partitioning of the unit cell length is further done into two paths, one above the asperity top with a width of $2R_0$, and the other in the grooves, with a width of $(L-2R_0)$. Leakage for a unit cell, Q' is given as:

$$Q' = Q'_1 + Q'_2 = \frac{b^3 \Delta p (2R_0)}{12\mu(r_1 - r_0)} + \frac{(a+b)^3 \Delta p (L-2R_0)}{12\mu(r_1 - r_0)} \quad (36)$$

Total leakage flow through the entire circumference is given as:

$$Q = Q' \times \frac{2\pi r_m}{L} = \frac{\Delta p (2\pi r_m)}{12\mu(r_1 - r_0)} (b^3 \delta + (a+b)^3 (1-\delta)) \quad (37)$$

4.3 NUMERICAL SOLUTIONS

The most common numerical solutions are finite element methods and finite difference methods. The application of finite differences is commonly found in the numerical solution to elliptic partial differential equations such as a Laplacian, $\nabla^2 f = 0$ or a Poisson's equation, $\nabla^2 f = g(x, y)$. Finite difference methods are preferred because of the advantages of less computational time and simplified incorporation of Reynolds cavitation condition.

4.3.1 Finite Difference Equations

The difference operator, Δ when applied to a given function, $f(x)$ and its variable, x , gives

$$\Delta f(x) = f(x + \bar{h}) - f(x) \quad (38)$$

$$\Delta x = (x + \bar{h}) - x = \bar{h} \quad (39)$$

where \bar{h} is the difference interval. The error introduced due to the approximations of differentials by finite differences is estimated from the Taylor Series,

$$f(x + \bar{h}) = f(x) + \Delta x f'(x) + \dots + \frac{(\Delta x)^n}{n!} f^{(n)}(x) + O(\bar{h}^{n+1}), \quad (40)$$

where $O(\bar{h}^{n+1})$ is the truncation error of order $(n+1)$. Using central difference method, the first order partial derivative of a function of two variables is approximated as,

$$\frac{\partial f(x, y)}{\partial x} \approx \frac{f(x + \bar{h}, y) - f(x - \bar{h}, y)}{2\Delta x} \quad (41)$$

and a second order partial derivative, as

$$\frac{\partial^2 f(x, y)}{\partial x^2} \approx \frac{\frac{f(x + \bar{h}, y) - f(x, y)}{\Delta x} - \frac{f(x, y) - f(x - \bar{h}, y)}{\Delta x}}{\Delta x} \quad (42)$$

where the error is $O(\bar{h}^2)$.

In Cartesian coordinates, the two-dimensional steady state Reynolds equation of a slider bearing is given as:

$$\frac{\partial}{\partial x} \left(h^3 \frac{\partial p}{\partial x} \right) + \frac{\partial}{\partial y} \left(h^3 \frac{\partial p}{\partial y} \right) = 6\mu U \frac{\partial h}{\partial x} \quad (43)$$

Generally, a five-point finite difference formula (figure 35-a) is used for approximating solution at the interior grid points. The second derivative in Reynolds equation is found to be highly sensitive to the cube of film thickness, h^3 . Hence, its values are taken from intermediate points instead of the grid points, as shown in figure (35-b). This method is known as a staggered grid approach. The results obtained by staggered grid method are found to agree with the analytical solution. For comparative results section (5.3), given later, may be referred.

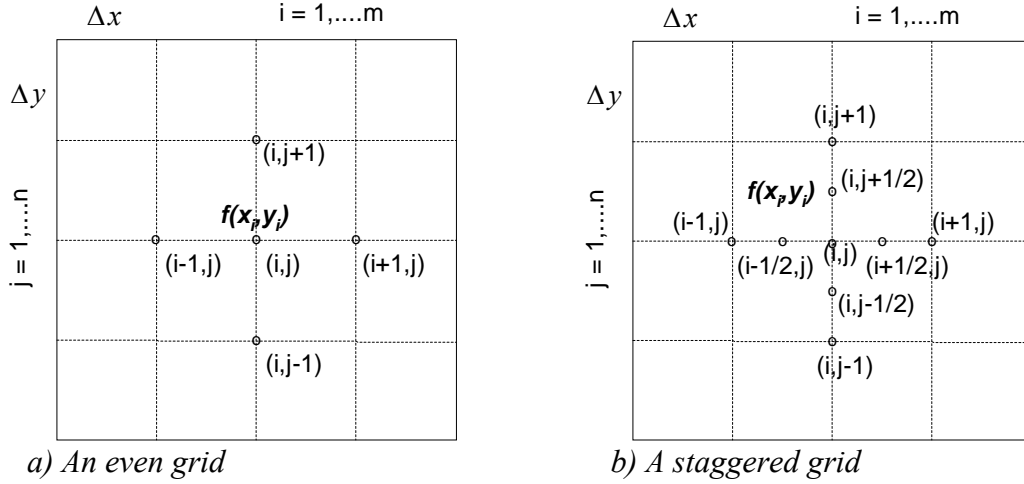


Figure 35: A finite difference mesh [33]

The terms from equation (43) are written as:

$$\frac{\partial}{\partial x} \left(h^3 \frac{\partial p}{\partial x} \right) = \frac{h^3_{i+1/2,j} \frac{p_{i+1,j} - p_{i,j}}{\Delta x} - h^3_{i-1/2,j} \frac{p_{i,j} - p_{i-1,j}}{\Delta x}}{\Delta x}$$

$$\frac{\partial}{\partial y} \left(h^3 \frac{\partial p}{\partial y} \right) = \frac{h^3_{i,j+1/2} \frac{p_{i,j+1} - p_{i,j}}{\Delta y} - h^3_{i,j-1/2} \frac{p_{i,j} - p_{i,j-1}}{\Delta y}}{\Delta y}$$

$$\frac{\partial h}{\partial x} = \frac{h_{i+1/2,j} - h_{i-1/2,j}}{\Delta x}$$

Substituting these equations back into Reynolds equation (43) gives:

$$\frac{h^3_{i+1/2,j} \frac{p_{i+1,j} - p_{i,j}}{\Delta x} - h^3_{i-1/2,j} \frac{p_{i,j} - p_{i-1,j}}{\Delta x}}{\Delta x} + \frac{h^3_{i,j+1/2} \frac{p_{i,j+1} - p_{i,j}}{\Delta y} - h^3_{i,j-1/2} \frac{p_{i,j} - p_{i,j-1}}{\Delta y}}{\Delta y} = \quad (44)$$

$$6\mu U \frac{h_{i+1/2,j} - h_{i-1/2,j}}{\Delta x}$$

Simplifying the above equation, we get

$$p_{i,j} = a_0 + a_1 p_{i+1,j} + a_2 p_{i-1,j} + a_3 p_{i,j+1} + a_4 p_{i,j-1} \quad (45)$$

$$i = 1 \dots m, j = 1 \dots n$$

where

$$a_0 = \frac{-6\mu U \frac{h_{i+1/2,j} - h_{i-1/2,j}}{\Delta x}}{\frac{h^3_{i+1/2,j} + h^3_{i-1/2,j}}{\Delta x^2} + \frac{h^3_{i,j+1/2} + h^3_{i,j-1/2}}{\Delta y^2}}$$

$$a_1 = \frac{\frac{h_{i+1/2,j}}{\Delta x^2}}{\frac{h^3_{i+1/2,j} + h^3_{i-1/2,j}}{\Delta x^2} + \frac{h^3_{i,j+1/2} + h^3_{i,j-1/2}}{\Delta y^2}}$$

$$a_2 = \frac{\frac{h_{i-1/2,j}}{\Delta x^2}}{\frac{h^3_{i+1/2,j} + h^3_{i-1/2,j}}{\Delta x^2} + \frac{h^3_{i,j+1/2} + h^3_{i,j-1/2}}{\Delta y^2}}$$

$$a_3 = \frac{\frac{h_{i,j+1/2}}{\Delta y^2}}{\frac{h^3_{i+1/2,j} + h^3_{i-1/2,j}}{\Delta x^2} + \frac{h^3_{i,j+1/2} + h^3_{i,j-1/2}}{\Delta y^2}}$$

$$a_4 = \frac{\frac{h_{i,j-1/2}}{\Delta y^2}}{\frac{h^3_{i+1/2,j} + h^3_{i-1/2,j}}{\Delta x^2} + \frac{h^3_{i,j+1/2} + h^3_{i,j-1/2}}{\Delta y^2}}$$

4.3.2 Solution Method

Equation (45) results in a linear system of algebraic equations expressed as

$$\sum_{j=1}^n a_{ij} x_j = b_i \quad , \quad i = 1, \dots, n$$

The coefficient matrix obtained for lubrication applications is not only large and sparse, but also amenable for iterative methods [31] & [30]. It addition, it is computationally advantageous to solve the set of equations by an iterative method rather than by direct calculations [29]. The iterative method produces a sequence of solution vectors,

$$\mathbf{x}^0, \mathbf{x}^1, \mathbf{x}^2, \mathbf{x}^3 \dots \dots \dots \mathbf{x}^k, \mathbf{x}^{k+1} \dots \dots$$

The system of equations, given in equation (45) above, can be solved by Jacobi iteration, Gauss-Seidel iteration or by Successive over relaxation.

In Jacobi iteration, the values obtained in any iteration are based entirely on the values of the previous iteration. This is given as:

$$x_i^{k+1} = x_i^k - \frac{1}{a_{ii}} \left(b_i - \sum_{j=1}^n a_{ij} x_j^k \right) \quad , \quad i = 1, \dots, n \quad (46)$$

Gauss-Seidel method on the other hand uses the most recent computed values in the iteration. It is expressed as:

$$x_i^{k+1} = x_i^k + \frac{1}{a_{ii}} \left(b_i - \sum_{j=1}^{i-1} a_{ij} x_j^{k+1} - \sum_{j=i}^n a_{ij} x_j^k \right) \quad , \quad i = 1, \dots, n \quad (47)$$

The number of iterations in both of these methods is proportional to N^2 , where N is the number of grid intervals in one dimension. However, with only a fewer iterations, a faster convergence to the correct solution is obtained by introducing a relaxation parameter, ω into the solution set, given as:

$$x_i^{k+1} = x_i^k + \omega \frac{1}{a_{ii}} \left(b_i - \sum_{j=1}^{i-1} a_{ij} x_j^{k+1} - \sum_{j=i+1}^n a_{ij} x_j^k \right) \quad i = 1, \dots, n \quad (48)$$

If the value of ω is unity, the above set of equations reduces to the Gauss-Seidel method. If $\omega < 1$, the method is slower and is called as under relaxation. When $1 \leq \omega \leq 2$, the method is called successive over relaxation (SOR). For values of $\omega > 2$, the method proves to be unstable. The optimal choice for ω , is obtained from the study of the eigenvalues of the iterative matrices. For lubrication problems, the values for ω in the range of 1.5 to 1.8 have been found to work well [30].

There are various ways of estimating the degree of convergence of the solution and one of them is the norm of relative error. Iteration process is stopped when the largest value of relative error is found to be less than an acceptable error value. The values obtained in the final iteration give us the solution. The relative error criterion is given as:

$$\max_{\substack{1 < i < i_{\max} \\ 1 < j < j_{\max}}} \left| \frac{p_{i,j}^{(k+1)} - p_{i,j}^{(k)}}{p_{i,j}^{(k)}} \right| < \varepsilon \quad (49)$$

The values of ε depend upon the grid size. For problems that can use coarser grids, smaller values of ε may yield the desired results. Generally, in lubrication problems, values of $\varepsilon = 0.0001$ have been found to have worked well [30]. As suggested in reference [27], a higher mesh size was used to improve the accuracy of approximations introduced by the misalignment of the grid points on the slant geometric boundaries, as shown in figure (36).

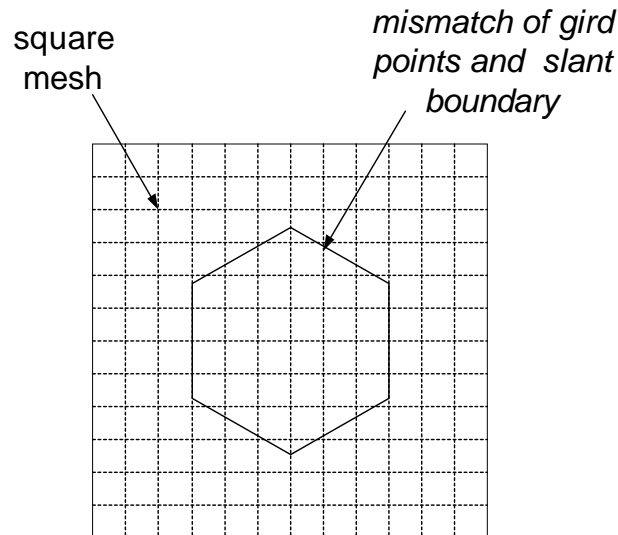


Figure 36: A hexagonal asperity in a square mesh

Accordingly, a higher value of $\varepsilon = 1e^{-6}$ had to be used even at the cost of greater computation time. The advantage of such a choice has clearly reflected in the accuracy of the solutions as will be evident in the graphs shown in the results section.

4.3.3 Reynolds Cavitation Condition

Numerical methods facilitate an easy process of introducing Reynolds condition in contrast to analytical methods. This is done by setting the sub cavitation values of the pressure obtained during each iteration step to cavitation pressure. For the present study, a zero cavitation pressure (gauge) has been assumed for convenience. In reality, saturation pressures of vapors and gases exist below this pressure. In mathematical terms this condition is written as:

$$P_{i,j}^{(k+1)} = \max(p_c, P_{i,j}^{(k+1)} S.O.R) \quad (50)$$

4.3.4 Negative Asperity Model

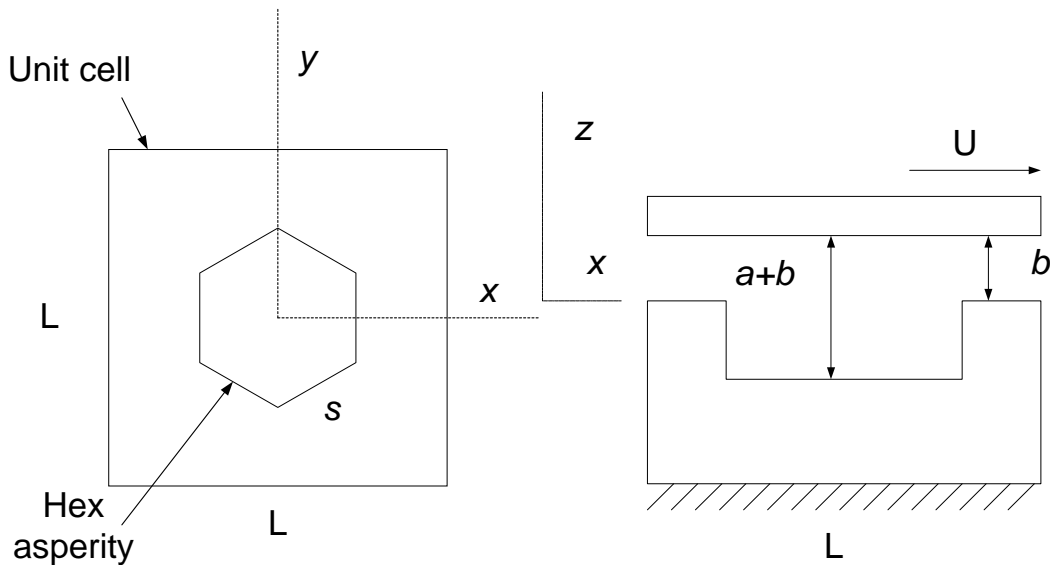


Figure 37(a) Top view

Figure 37(b): Side view

Figure 37: Negative asperity model

Figure (37-a) shows a hexagonal model used for studying the performance characteristics of the negative asperities presently produced with UV photolithography process at University of Kentucky. This figure also shows the side view details, (figure 37-b) of the unit cell in conjunction with a top slider moving with constant velocity, U

With the assumption of a perfectly flat surface, the equations for film thickness can be written as:

$$h(x, y) = \begin{cases} a + b & \text{above the negative asperity} \\ b & \text{between asperities} \end{cases} \quad (51)$$

Neglecting the squeeze effects, the governing steady state Reynolds Equation for pressure distribution for the entire unit cell is given by the equation:

$$\frac{\partial}{\partial x} \left(h^3 \frac{\partial p}{\partial x} \right) + \frac{\partial}{\partial y} \left(h^3 \frac{\partial p}{\partial y} \right) = 6\mu U \frac{\partial h}{\partial x}$$

In the direction of y , following boundary conditions exist:

$$p(x, -L/2) = 0$$

$$p(x, L/2) = \Delta p$$

However, without the loss of trends in the results, simplified boundary conditions may also be used. Complete boundary conditions are thus expressed as:

$$p(x, -L/2) = p(x, L/2) = 0 \quad (52)$$

$$p(-L/2, y) = p(L/2, y) \quad (53)$$

$$\frac{\partial p}{\partial x}(-L/2, y) = \frac{\partial p}{\partial x}(L/2, y) \quad (54)$$

This resulting finite difference equation is solved iteratively using Successive Over-Relaxation (SOR) method. The Swift-Steiber cavitation condition was applied by setting negative values of pressure to P_c during each iterative process. After obtaining pressure distribution, average pressure for one unit cell is calculated by dividing the load support expression by the area of a unit cell. Accordingly, we have

$$P_{avg} = \frac{1}{L^2} \sum_{-L/2}^{L/2} \sum_{-L/2}^{L/2} p(x, y) dx dy \quad (55)$$

Since the applied load is assumed constant for this study, film thickness is solved for, iteratively, using the value obtained from equation (55) above. In addition to the pressure distribution and load capacity, an expression for the friction coefficient is arrived at, by considering the total frictional force over the unit cell. Average shear stress is given as:

$$\tau_{avg} = \frac{1}{L^2} \sum_{-L/2}^{L/2} \sum_{-L/2}^{L/2} \tau(x, y) dx dy \quad (56)$$

Coefficient of friction is obtained from equations (31, 32, 55 and 56) and is given as:

$$f = \frac{1}{P_{avg}} \left[\mu U \left(\frac{\delta^2}{(a+b)} + \frac{(1-\delta^2)}{b} \right) + \frac{1}{L^2} \int_{-L/2}^{L/2} \int_{-L/2}^{L/2} \frac{\partial p}{\partial x} \frac{h}{2} dx dy \right] \quad (57)$$

The general expression for leakage at the exit (at I.D.), for a unit cell is given as;

$$Q = q_y dx = \left(-\frac{h^3}{12\mu} \frac{\partial p}{\partial y} + \frac{Uh}{2} \right) dx$$

However, leakage is found to be governed by Poiseuille law [7] and occurs through the leakage channels in the radial direction due to hydrostatic pressure difference. For negative asperities, only the film thickness provides the leakage channel. Thus, the governing expression for leakage rate for the entire ring is given as;

$$Q = \frac{\pi \Delta p (r_o + r_i)}{12\mu (r_1 - r_o)} b^3 \quad \text{for negative asperities} \quad (58)$$

4.3.5 Flow Chart for a Numerical Solution

To start with, input parameters such as speed, viscosity, dimensions of the ring, hydrostatic pressure and cavitation pressure are all taken as constants for a given application. Then, input variables such as the number of asperities, radius of the asperity, asperity height are also taken from the sample dimensions. The process starts with an initial guess of the film thickness. After setting the boundary conditions, solution for pressure distribution is obtained. Later, Reynolds cavitation condition is imposed and convergence is checked. Grid size may be refined till a satisfactory solution is obtained. Subsequently, load support is calculated and if this value does not match the value of the given constant load, the solution process goes through reiteration till a proper value is obtained. (In this study, this step was done manually). Once

satisfactory load support is achieved, other outputs such as average pressure, average shear stress, coefficient of friction, leakage are calculated and recorded along with the film thickness value. The process may be restarted for a different case where either the number of asperities or asperity height, etc. is varied. Matlab script files given in the appendix (A.2) may be referred for a clear understanding of the scheme used for obtaining results in this study. To summarize, a complete process of a numerical scheme is also given in the flowchart in figure (38) below.

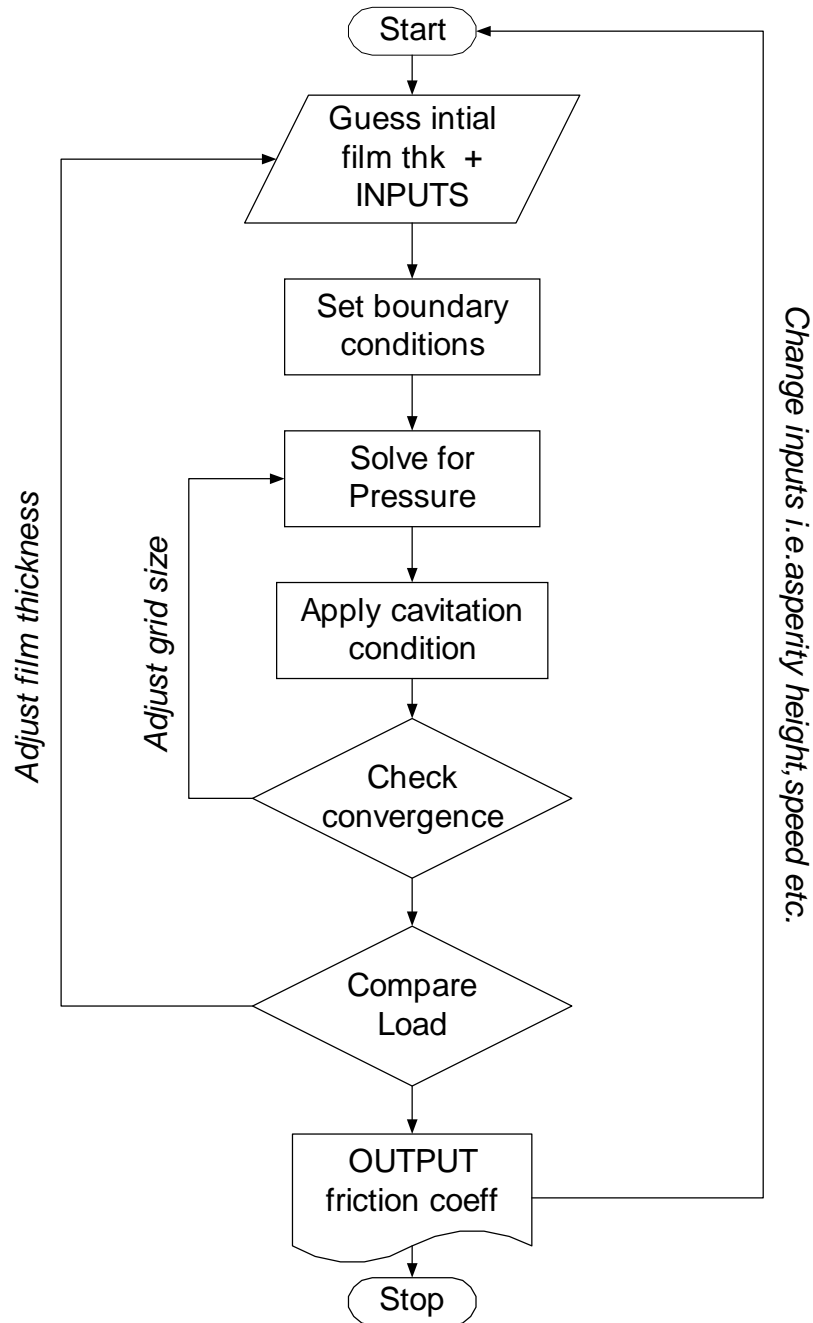


Figure 38: Flow chart for a numerical scheme

4.3.6 Radial Distribution Model

This model, shown in figure (39), gives the advantage of applying actual pressure boundary conditions in the radial direction without resorting to approximations such as those found in either the unit cell model or the hexagonal distribution model where an outer pressure boundary was assumed. However, the drawback in this model is that the unit cell dimensions are not held constant. They are found to increase progressively in the radial direction, from inner diameter to outer diameter, but in the circumferential direction, they are the same. Hence, an approximation of a constant unit cell area is required, in order to use these models. Though the present thesis uses a unit cell model, a radial model has been developed to present the asperity interactions and the profile of pressure distribution for a better understanding. The unit cell model has been favored in this study for saving computation time.

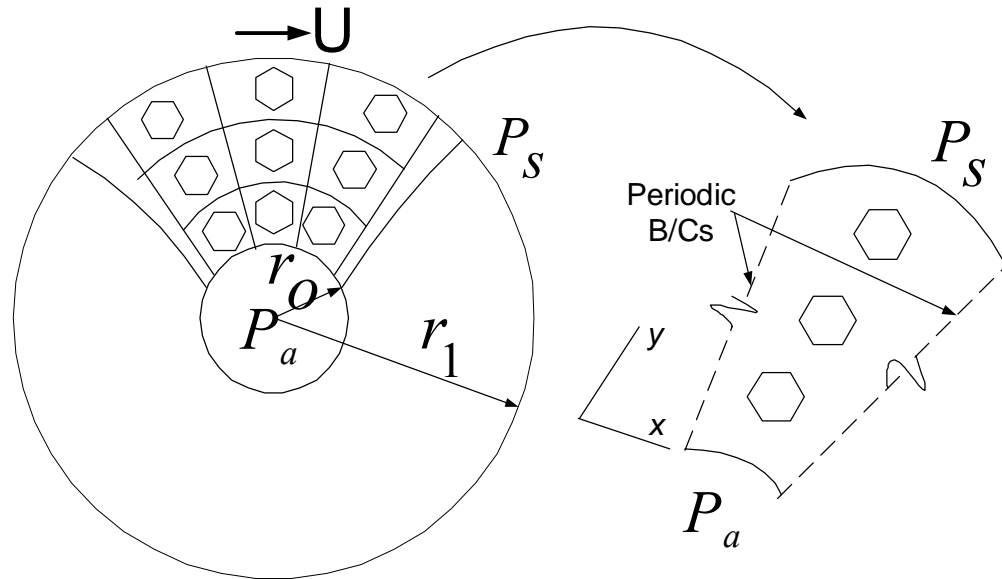


Figure 39: Microasperities on a thrust bearing (not to scale)

A thrust bearing specimen with radial distribution of asperities is considered for fabrication and testing. The thrust ring has an inner radius of r_o , an outer radius of r_1 and is subjected to an external sealant pressure of P_s . The exit pressure is P_a at the inner boundary. Since the distribution of asperities is axisymmetric, instead of a single square unit cell, a row of cells in the radial direction is taken as a periodic entity. For a higher ratio r_o to the face width ($r_1 - r_o$), the hydrodynamic characteristics can be analyzed in Cartesian coordinates by unrolling the thrust ring geometry into a strip. It may be pertinent to know that the asperities nearer to the inner row are less affected by the hydrostatic pressure and hence they are more likely to cavitate when compared to the cells nearer to the outer diameter.

Reynolds equation in Cartesian coordinates is given as:

$$\frac{\partial}{\partial x} \left(h^3 \frac{\partial p}{\partial x} \right) + \frac{\partial}{\partial y} \left(h^3 \frac{\partial p}{\partial y} \right) = 6\mu U \frac{\partial h}{\partial x}$$

Dirichlet boundary conditions in the radial direction are:

$$p(x, y = 0) = P_a \tag{59}$$

$$p(x, y = (r_1 - r_0)) = P_s \quad (60)$$

And in the circumferential direction, along the direction of speed, periodic boundary conditions are used:

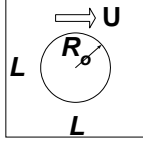
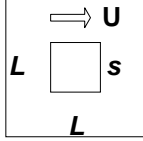
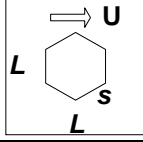
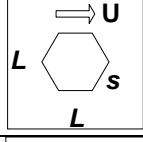
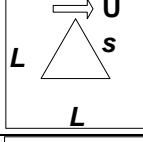
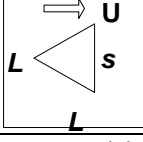
$$p\left(x = -\frac{L}{2}, y\right) = p\left(x = \frac{L}{2}, y\right) \quad (61)$$

$$\frac{\partial p}{\partial x}(-L/2, y) = \frac{\partial p}{\partial x}(L/2, y) \quad (62)$$

4.3.7 Model Matrix

The various models considered in this study are a combination of different shapes and one of their respective orientations, as shown in table (6). As discussed earlier, a single cell is used instead of a radial model for saving computation time. However, no contradiction in trends is found (see section 5.8.5). Table (6) also gives the corresponding allowable maximum asperity area fraction in a separate column. It is important to note that a full range of asperity area fractions (up to a maximum of 1.0) is not obtained with all the geometries. A square geometry gives the full range and a triangle has the least range of asperity area fractions when considered in a square unit cell. Reynolds number is expected to be different for different asperity area fractions and also for positive and negative asperity area fractions. With each different asperity area fraction, a different film thickness is observed and hence the hydraulic diameters would be different. Similarly, for different geometries, different Reynolds numbers are obtained; the maximum value obtained is 369 that corresponds to a laminar flow, in line with the assumption made for deriving Reynolds equation. A range of values for each of the geometries is also given in the following table.

Table 6: Geometries used in this thesis

<i>S.No.</i>	<i>Unit Cell</i>	δ^2	δ^2_{\max}	<i>Asperity Width</i>	<i>Reynolds Numbers* (range)</i>
1		$\frac{\pi R_0^2}{L^2}$	0.785	$2R_0$	225-351
2		$\frac{s^2}{L^2}$	1.0	s	11.3-369
3		$\frac{3\sqrt{3}s^2}{2L^2}$	0.65	$2s$	8.59-363
4		$\frac{3\sqrt{3}s^2}{2L^2}$	0.65	$\sqrt{3}s$	37.0-168
5		$\frac{\sqrt{3}s^2}{4L^2}$	0.433	$\frac{\sqrt{3}s}{2}$	37.0-156
6		$\frac{\sqrt{3}s^2}{4L^2}$	0.433	s	8.59-146

* For positive asperities

Chapter V: RESULTS AND DISCUSSION

5.1 VARIABLES AFFECTING LOAD SUPPORT

For a given thrust ring size, the physical parameters affecting hydrodynamic load support are the film thickness, viscosity, speed and the geometry of the asperities. The geometry of the asperity includes the dimensions such as the asperity radius, the unit cell radius (or the number of asperities) and the asperity height. Since viscosity is constant for a given situation or an application, only the effect of the rest of the factors is considered here. For obtaining reliable results from the effect of each of these variables, analytical model as described in section (4.2.3) is used. Simulations are then undertaken using the values of parameters from our sample dimensions as given in table (2), to give us an approximate indication of the expected magnitudes. Asperity radius is taken as 7 micrometers and film thickness as, 7.8 micrometers as considered in our earlier paper [1].

5.1.1 Speed

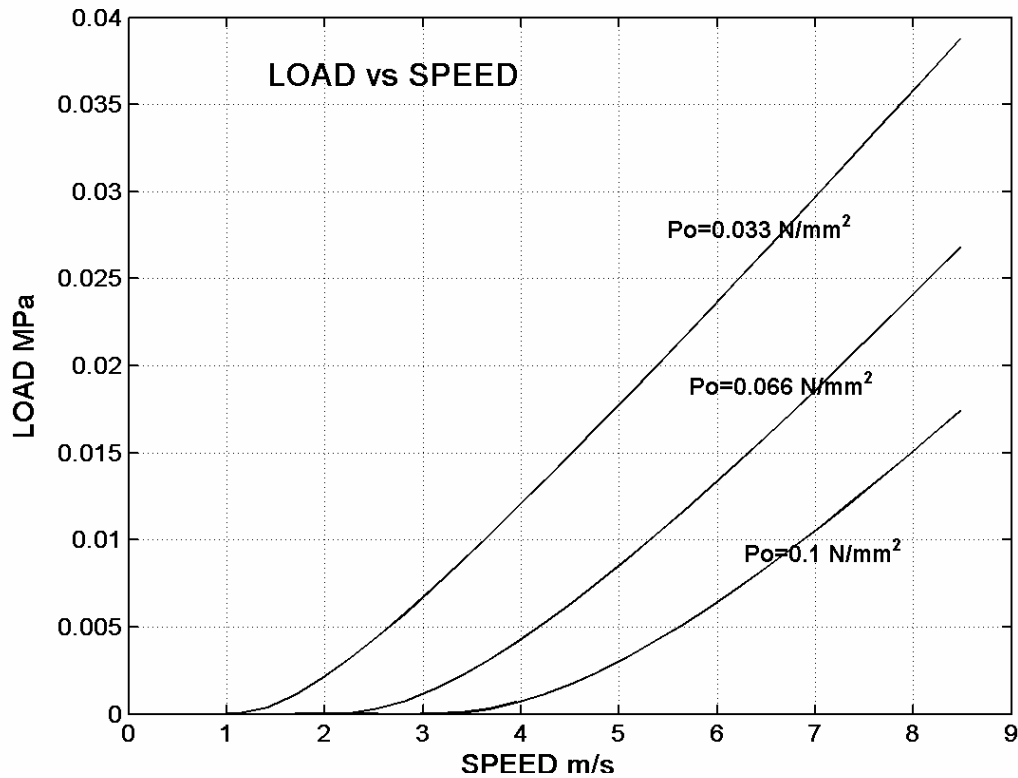


Figure 40: Load support curves for sealing pressures

Figure (40) shows the graph of the load support at various speeds for various sealing pressures, P_o . Cavitation begins to occur when a critical speed is reached and once the maximum cavitation effect is attained, load support is found to depend only on speed. Hence, the graph is linear at higher speeds. As the sealing pressures are increased, a decrease in load support is observed.

5.1.2 Number of Asperities

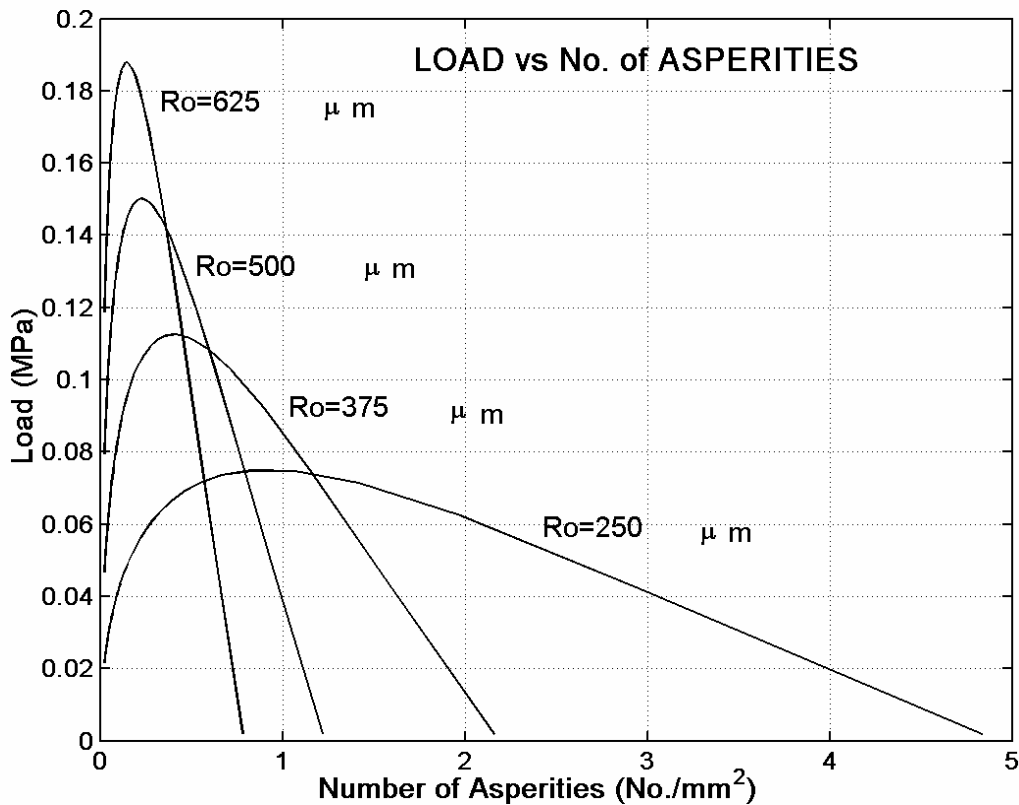


Figure 41: Load support for number of asperities

The graph of load capacity and the number of asperities, for various values of asperity radius, is given in figure (41). The fewer the numbers of asperities, fewer are the load supporting asperities, and hence lesser is the aggregate load support. Also, the asperity interaction is weak in such a case. With increased number of asperities, more interactions and more load supports are observed. Further close package of asperities results in a downward trend in load support values, after gaining an optimum value. For an asperity radius of $275\mu m$, as used in our earlier paper [1] and number of asperities of $2.5/mm^2$, it may be inferred from the above graph that the load support is closer to $0.1MPa$, which is the load that has been used for testing.

5.1.3 Asperity Radius

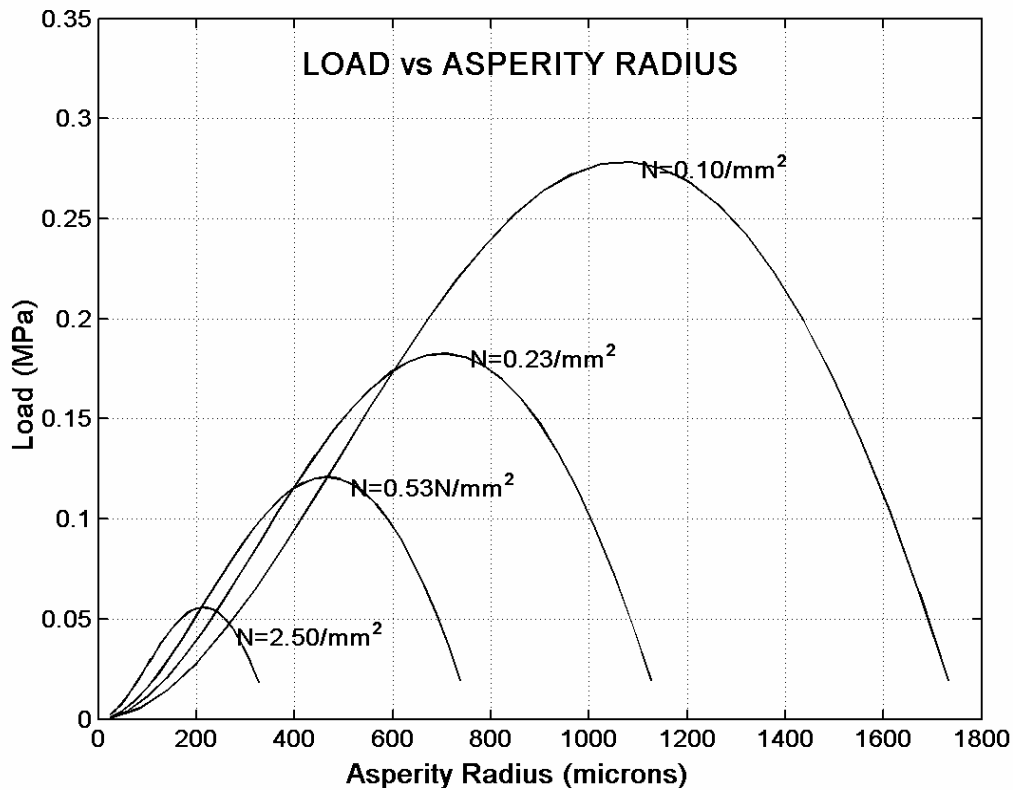


Figure 42: Load support for asperity radius

For a given number of asperities, if the radius of an asperity is increased, load support increases only up to a certain value and later it decreases. This trend is clearly seen in figure (42), which shows the influence of asperity radius on load support for different values of number of asperities. A decrease in number of asperities gives rise to an increase in load carrying capacity. This observation can also be inferred from figure (42) given above.

5.1.4 Asperity Area Fraction

Closely related to the figures (41) and (42), is the graph (figure 43) of load support for various values of asperity area fraction, defined as the fraction of the area of the asperity in a unit cell area. As expected, there exists an optimum value for asperity area fraction too. The optimum level is noted to occur in the asperity area range of 0.2 and 0.5. Also, as the number of asperities is decreased, an increase in load support may be observed till an optimum value is reached.

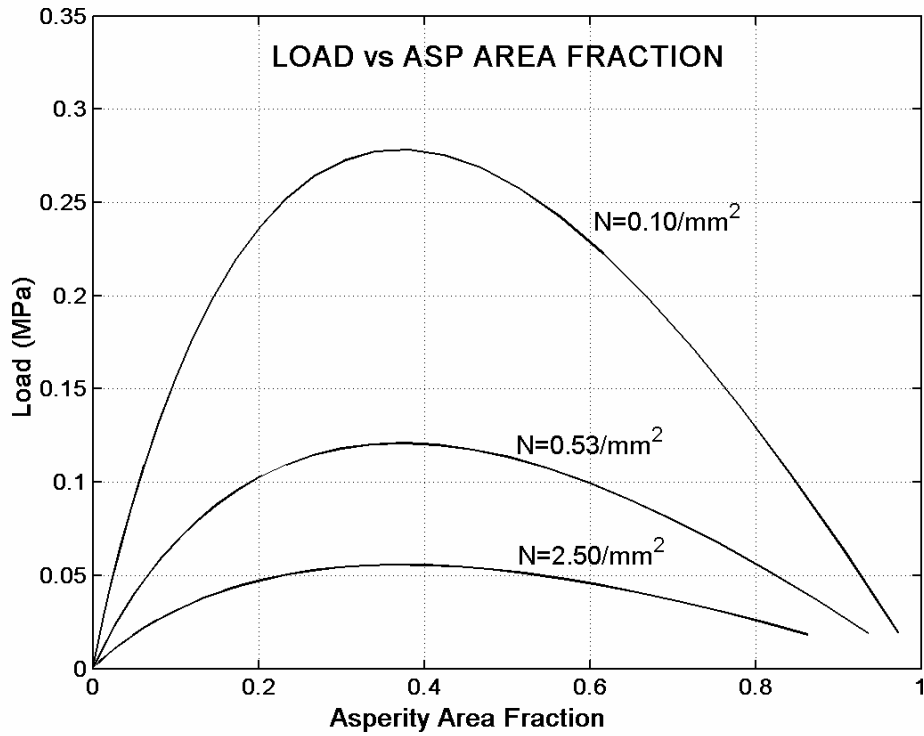


Figure 43: Load support for asperity area fractions

5.1.5 Asperity Height

For a fixed value of total film thickness ($a+b$), as the asperity height is increased, more pressure is generated until the asperity begins to touch the other surface. However, if the value of film thickness is taken constant and as the asperity height is increased, more load support is generated initially. Later, the values are reduced. This is due to the diminished effect of shear stresses when total film thickness is increased. Figure (44) shows the graph of such relationship. It is also be deduced from the graph that greater support is experienced when both the film thickness and the asperity height values are sufficiently low.

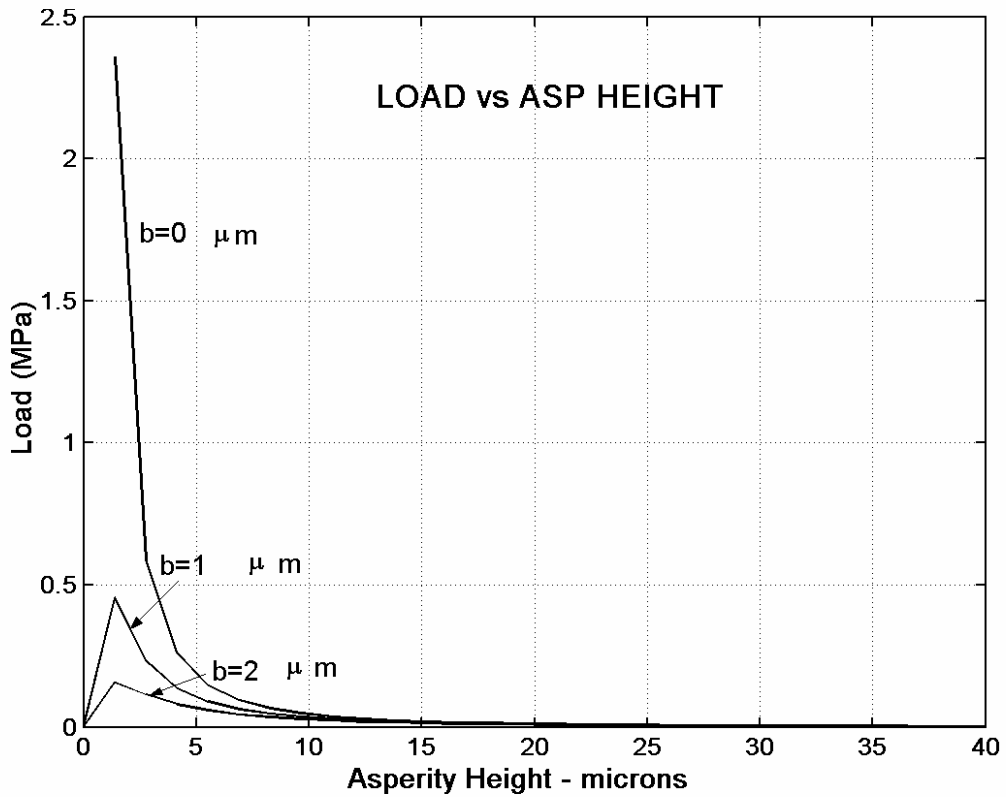


Figure 44: Load support for asperity heights

5.1.6 Film Thickness

In a practical situation, asperity height is constant and hence changes in operating conditions influence the film thickness values. It may be then useful to find out the relationship between film thickness and load capacity. Figure (45) shows, for a low film thickness, it is evident that high load capacities are formed. The slope of the graph gives stiffness. A decrease in film thickness and similarly a decrease in asperity height, result in higher film stiffness.

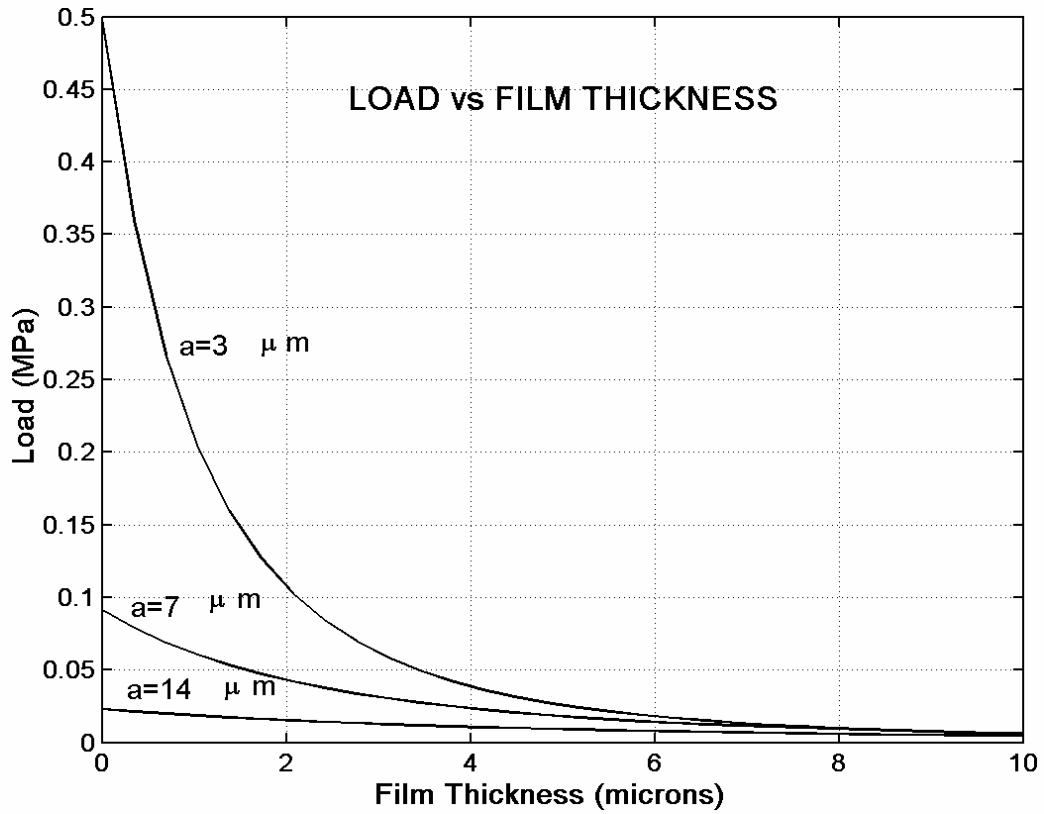


Figure 45: Load support for film thickness

5.2 ANALYSIS WITH ANSYS®

Initially, ANSYS® (*Flotran*) was used as an analysis tool to find out the hydrodynamic effects of various asperity shapes considered for this thesis. The flexibility and ease of using a wide range of irregular geometries and the advantage of utilizing Navier Stokes equations as a solution process had been major deciding factors in favor of using ANSYS.

While results for a one-dimensional step slider agreed closely with the analytical solution, the data from a two-dimensional case was not encouraging, though no difference was found in the trend.

Table 7: Comparison of ANSYS and analytical solution

<i>Asperity Radius (μm)</i>		12.7	25.4	50.8	102	191	203	305	356	368
<i>Max Press</i>	<i>Analytical (MPa)</i>	5.77	14.27	27.97	54.85	70.87	71.31	42.30	15.88	8.03
	<i>ANSYS (MPa)</i>	12.79	20.87	37.01	63.00	80.27	78.46	47.21	*	*
<i>Difference</i>		121%	46%	32%	14%	13%	10%	11%	N.A.	N.A.

* ANSYS gave no solutions due to coincidence of points at higher asperity area fraction.

Table (7) shows the values obtained for a two dimensional circular asperity in a circular layout that can be compared to the available analytical solution. The radius of the unit cell is $381\mu m$. It is evident from the data that wide variations in results exist. In addition to this, another dissuading factor to use the software is that it does not appear to provide any control on the iteration process, once the solution process is initiated. Hence, Reynolds cavitation condition cannot be imposed, as it requires equating sub ambient pressures to zero during each iteration process. However, provision exists, facilitating the implementation of half Sommerfeld condition. As realistic load support values cannot be achieved, this approach was abandoned and finite difference method was adopted in finding numerical solutions to the Reynolds equation by using MATLAB® software.

5.3 EVEN AND STAGGERED GRIDS IN F.D. METHOD

The difference in an even and staggered grid was covered earlier in finite difference equations (see section 4.3.1). A one-dimensional Rayleigh step slider (figure 22) was chosen as the model. Initially, simulations were run with an even grid and the results were found to be deviating quite a lot from the analytical solution. Later staggered grid method was used. The sensitivity in the results obtained due to the selection of a staggered grid is amply demonstrated by the difference in curves given in figure (46). Convergence of the results is obtained by a suitable choice of grid size and error criterion. For an asperity height of $5\mu in(0.125\mu m)$, film thickness of $3\mu in(0.075\mu m)$, step radius of $8e-3 in(0.2mm)$ and a unit cell length of $30e-3 in(0.76mm)$, velocity of $50 in/s(1.27m/s)$, the analytical solution for maximum pressure was found to be $28.78 psi(0.0198MPa)$. The following table (8) shows the grid size and the corresponding values for numerical results.

Table 8: Convergence values

S.No.	Error Value	Grid Size	Numerical Solution <i>Psi (MPa)</i>	Analytical Solution <i>Psi (MPa)</i>
1	1e-6	6	31.15 (0.0215)	28.78 (0.0198)
2	1e-6	12	30.41 (0.0209)	- ditto-
3	1e-6	24	29.59 (0.0204)	-ditto-
4	1e-6	36	29.49 (0.0203)	-ditto-

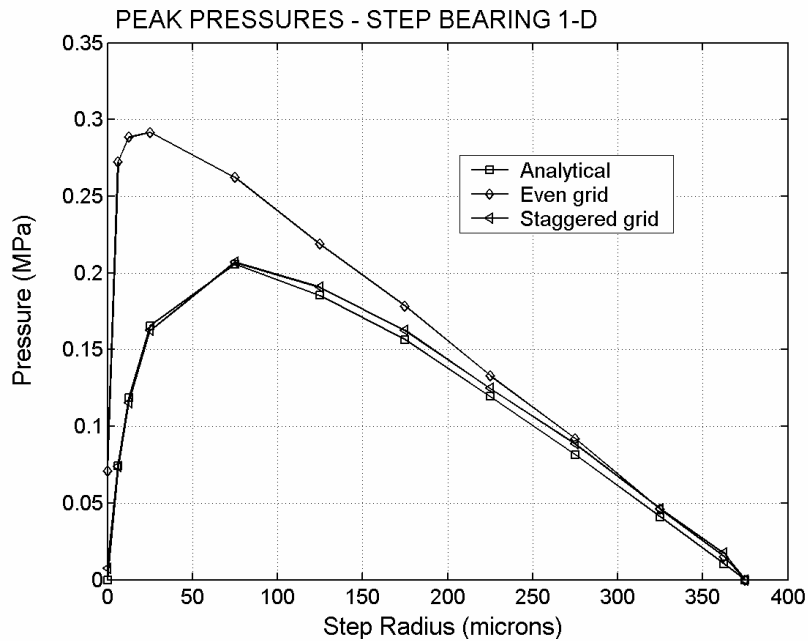


Figure 46: Even, staggered grid and analytical results

From figure (46) we can infer that while the staggered grid values agree well with those of the analytical ones, a significant variation is found with the even grid approach, especially in the range of lesser step length ratios, $\delta = s/L$, and this is the range in which pressure slopes are noted to be high. There is also a difference in the values of δ in both these cases, where peak pressure occurs. For analytical and staggered grid approaches, peak pressure develops at a step length ratio of 0.20 whereas for the even grid case the corresponding value is equal to 0.067. A few other comparative values for pressure are given in table (9). Figures in brackets give percentage deviation from the analytical solution. It may be observed that minor variations exist with a staggered grid approach across the data point range except at the end values.

Table 9: Comparative results for even and staggered grids

Step Radius (μm)	Maximum Pressure in MPa		
	Analytical	Even grid	Staggered grid
6.25	0.0742	0.2523 (240%)	0.0737 (1%)
25	0.1657	0.2916 (76%)	0.1624 (2%)
75	0.2055	0.2621 (28%)	0.2068 (1%)
175	0.1565	0.1786 (14%)	0.1624 (4%)
325	0.0410	0.0459 (12%)	0.0461 (12%)

5.4 BENCHMARKING

Figure (47) shows the benchmarking results for a two dimensional model. The given pressures are transformed to non-dimensional values with respect to atmospheric pressure. Comparison is made between an infinitely long square asperity and the well known analytical solution of a one-dimensional Raleigh step bearing. An infinitely long step bearing is in fact a two dimensional geometry with an assumed infinite width that is equivalent to a one dimensional step bearing. For numerical modeling, this infinite width is taken as five times the length as it gave acceptable results. The curves given in the above figure, for both the cases of positive and negative asperities, are in very close agreement with the analytical results, in the entire range of the step length ratio, $\delta = s/L$. It is also clear from the figure that the results are symmetric with each other.

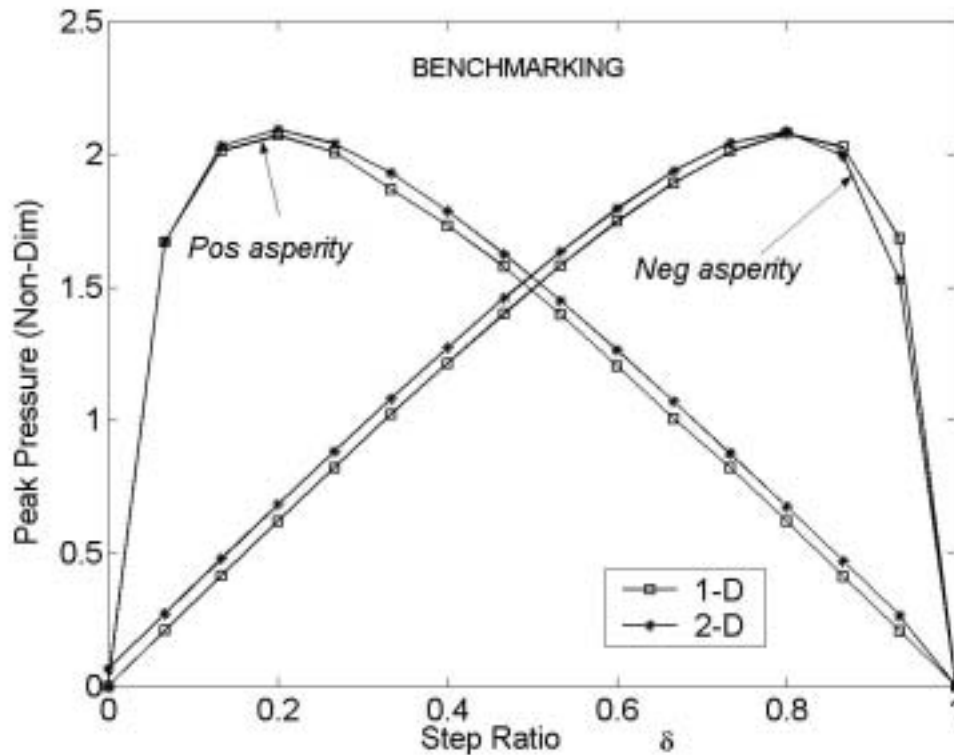


Figure 47: Benchmarking for a 2-D model

For all the results that follow, variables comprising asperity layout, number of asperities per unit area, asperity height, viscosity, velocity, dimensions of the thrust ring, hydrostatic pressure across the thrust bearing, are assumed to be constant. Table (3) in section 1.3, gives the values assumed for this study and the applied load is taken as 0.1 N/mm^2 (MPa). These values are consistent with those used for the experimental results in our earlier paper [1]. At a constant load, different values for δ^2 produce different film thickness values and both these values have a major effect in determining the shear stress and leakage values. For a constant film thickness, on the other hand, shear stress is based on the values of δ^2 only. In the rest of this section, results at constant load are compared at times with constant film thickness conditions, for additional understanding.

5.5 RESULTS FROM THE RADIAL MODEL

Based on the models worked out in the earlier section, simulations for a radial distribution of three asperities are performed for a constant film thickness and a given asperity height.

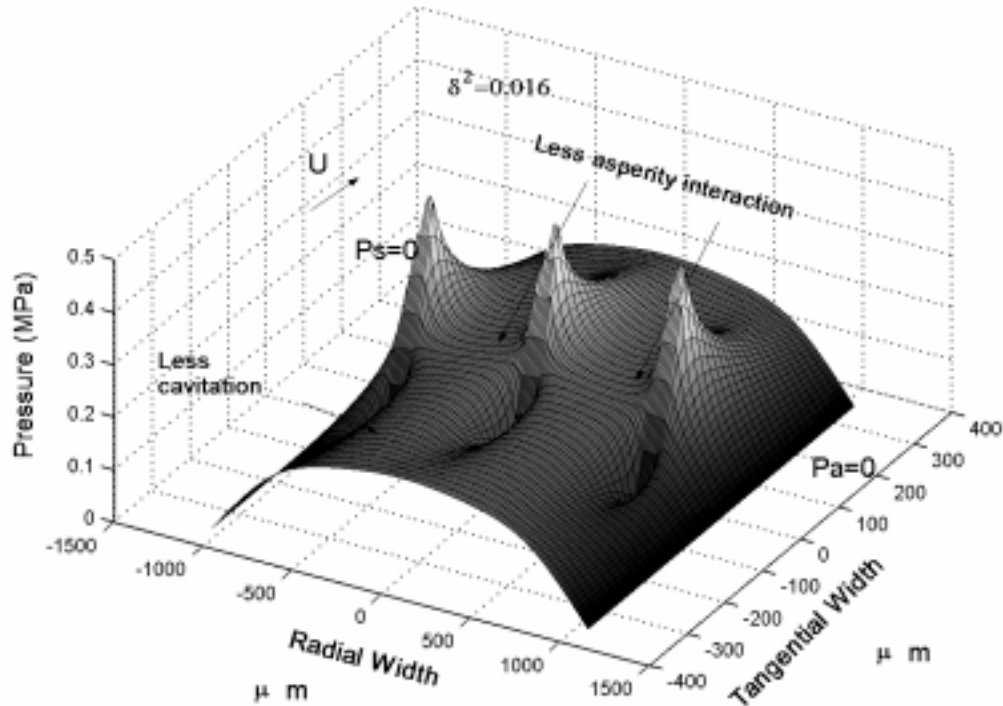


Figure 48: Radial pressure distribution for smaller pores

Figure (48) shows a Reynolds pressure distribution for a circular negative asperity of $100\mu m$ in diameter in a $715\mu m$ tangentially wide model. The radial length is thrice the tangential width. Each sub cell has periodic length equal to the dimensions of the fabricated sample which is used for analytical results as given in section 5.1 earlier. The asperity area fraction is 0.0159. Less asperity interactions prevail in the radial direction due to limited cavitation effects that can also be clearly seen from the figure. The lesser values of pressure and load support given in table (10) below also support this evidence. The values of inter asperity pressures are not zero owing to the hydrodynamic effects in the tangential direction. The asperity at the center generates higher peak pressure when compared to the other two that have equal peak pressures. The figure also reveals that in the circumferential direction, pressures at the boundary are not equal to zero, due to the imposition of periodic boundary conditions in the solution procedure.

Table 10: Sample results for a radial distribution

<i>Property</i>	<i>Wide asperity</i>		<i>Small asperity</i>
	Positive asperity	Negative asperity	Negative asperity
Tangential width (<i>microns</i>)	715	715	715
Asperity diameter (<i>microns</i>)	550	550	100
Asperity area fraction	0.4815	0.4815	0.0159
Maximum pressure (<i>MPa</i>)	0.7601	1.6176	0.4256
Average load (<i>MPa</i>)	0.2923	0.6586	0.1488
Coefficient of friction	0.1064	0.0472	0.2777

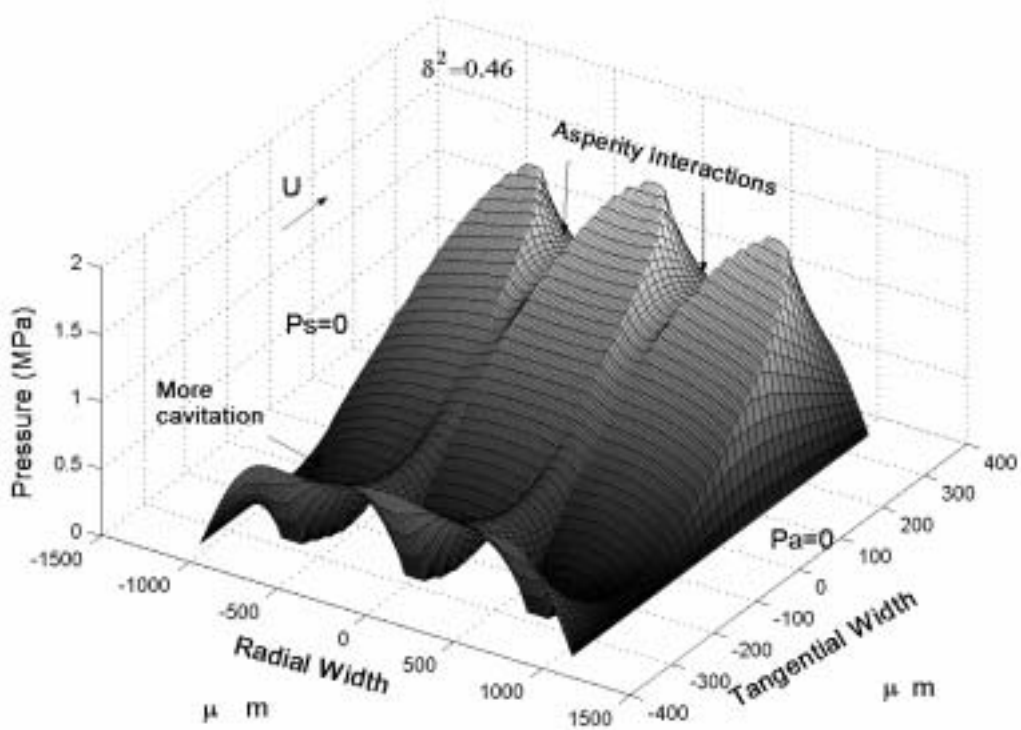


Figure 49: Radial pressure distribution for larger pores

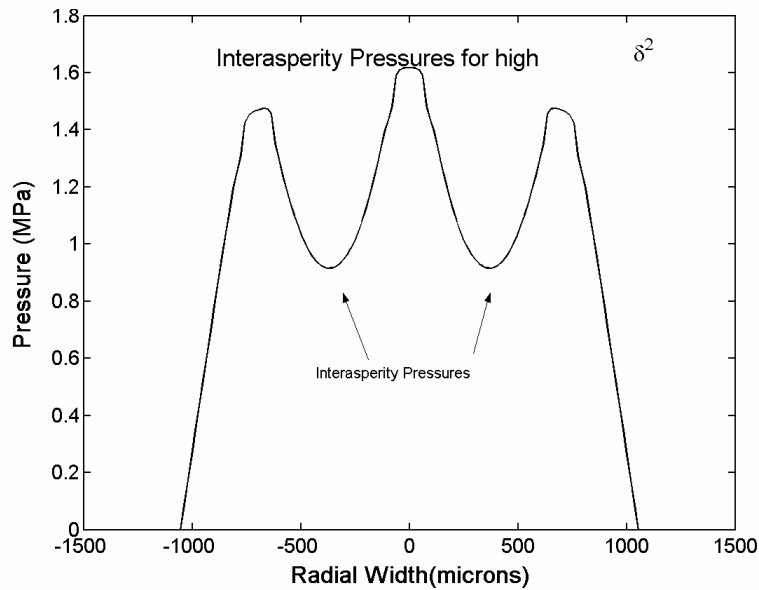


Figure 50: Interasperity pressures in a radial layout

As expected, pressure distribution of a large asperity (see figure 49) shows higher cavitation effects and accordingly higher pressures and greater load support values are recorded. Asperity interaction is also significant because of a closer distribution of asperities. Pressure observed at a mid point between two asperities in the radial direction is significant and is found to be approximately $1MPa$ (figure 50). This finding also agrees with the observations given in reference [2]. Table (10) also gives a comparison of the results for positive and negative asperities with the same dimensions. It is evident that for a constant film thickness, negative asperities support more load and consequently give rise to low coefficient of friction. The pressures generated are also quite high when compared to those of positive asperities.

5.6 BASIS FOR COMPARING DIFFERENT SHAPES

The magnitude and the extent of pressure distribution is dependent upon the asperity area fraction for a given asperity height either for a constant film thickness or for a constant load condition. Load support is calculated by integrating pressure over an entire unit cell area. Hence, the load support values are also dependent on the asperity area fraction. And, a minute change in a load support value results in a disproportionate variation of coefficient of friction. All these interdependencies reveal a significant impact of asperity area fraction on pressure, load support and coefficient of friction. Therefore, it is considered meaningful to ensure that the geometries have equal asperity area fractions when used for comparison. Other alternatives for comparing geometries, such as hydraulic diameter, have also been examined. It has been found that a given hydraulic diameter yields variations in asperity areas for different geometries capable of generating wide variation in results. Accordingly, the option of considering hydraulic diameter as a basis for comparison was discarded and asperity area fraction was preferred.

The values for parameters used in numerical simulations are made consistent with the actual measurements of a thrust surface that is fabricated using U.V. lithography and is planned for use in subsequent tests. These are given in table (3) in section 1.3.

Initially, most of the simulations were performed in a dimensional form using the data given in the above table. It was later viewed that the results for pressure could be made dimensionless with respect to atmospheric pressure and the leakage results may be retained in dimensional form, for better comprehension of the data. Coefficient of friction, being a dimensionless quantity remains unaffected by this decision.

5.7 RESULTS

5.7.1 Pressure Distribution

Full Sommerfeld and Reynolds pressure distributions have been generated for all the geometries and for different orientations. Representative graphs are shown in figures (51&52), for a hexagon and (53&54) for a triangle. These figures represent pressure distributions for positive and negative asperities of equal asperity area fractions in each of the cases. The pressure distribution for all positive asperities appear smooth at the leading edges of the asperity boundaries and can be distinctly seen in figure (51). This observation is consistent with the expected flow pattern around a positive asperity where tangential flow is deflected in the radial directions on striking against a positive asperity. For negative asperities, in general, the pressure distribution follows the geometrical shape of the asperity and this may be due to the absence of any obstruction to the tangential flow. The edges appear to be well defined (straight) for a hexagon (figure 52) when compared a triangle (figure 54). This could be due to the presence of additional sidewalls in a hexagon that help in decreasing the pressure gradient across the direction of flow. As expected, pressures are not zero at the unit cell boundaries in the direction of flow, because of the application of periodicity boundary conditions. Pressures at the boundaries in radial direction are equal to the hydrostatic pressure and the ambient pressure, both assumed as zero in this instance.

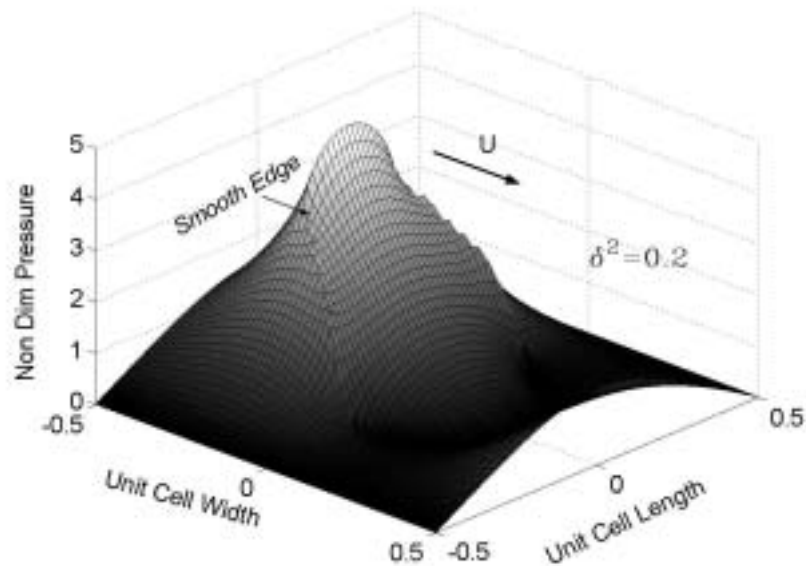


Figure 51: Reynolds pressure distribution for a positive hexagon

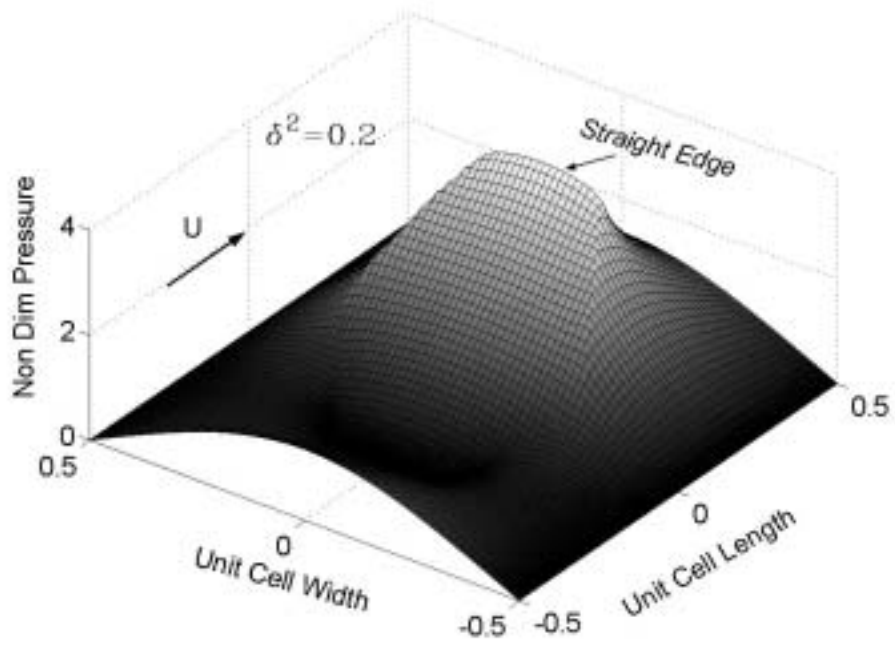


Figure 52: Reynolds pressure distribution for a negative hexagon

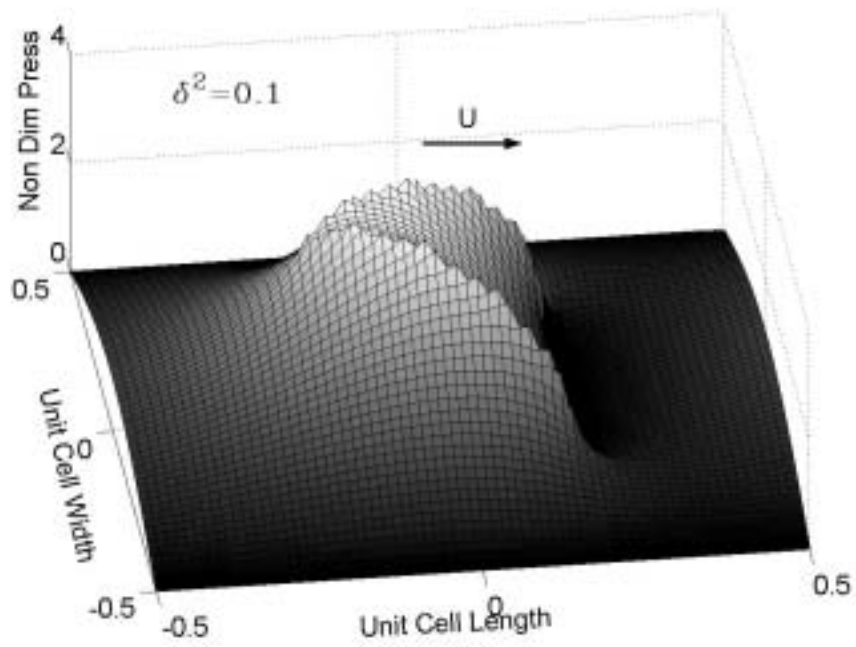


Figure 53: Reynolds pressure distribution for a positive triangle

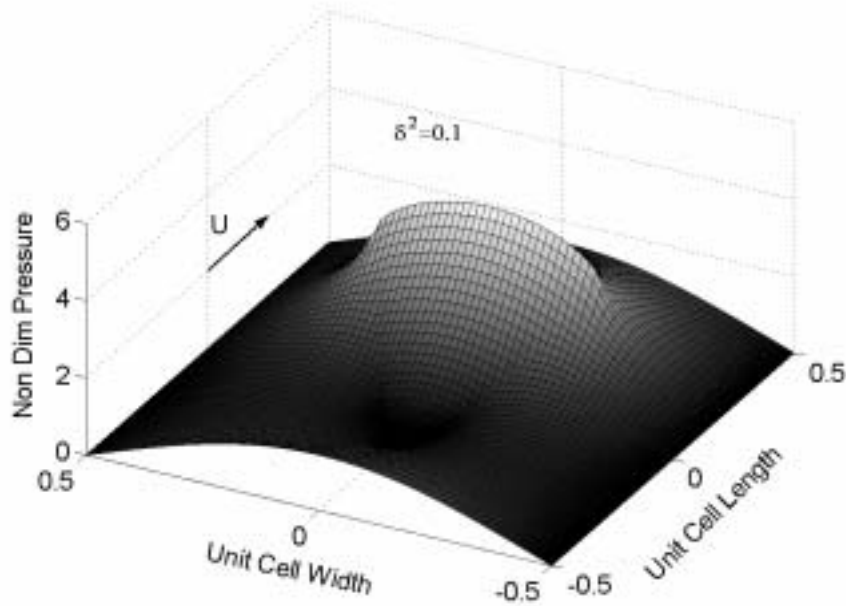


Figure 54: Reynolds pressure distribution for a negative triangle

Table 11: Peak pressures for different shapes

<i>Parameter</i>	δ^2	0.05	0.1	0.2	0.3	0.4
Peak Pressures (MPa)	Rectangle	0.0490	0.0460	0.0349	0.0329	0.0321
	Diamond	0.0382	0.0314	0.0261	0.0230	0.0215
	Triangle	0.0453	0.0377	0.0314	0.0286	0.0270

Table (11) shows peak pressures developed by three different shapes for a constant load condition for varying values of δ^2 . For all the three shapes, the values of peak pressures decrease with an increase in asperity area fraction. These results are expected because they compensate for the increase in asperity area fractions to keep the load support constant. The rest of the shapes also show a similar trend.

Finally, the effect of the shape of the leading edge was investigated. To investigate this factor, numerical simulations were run for different leading shapes as shown in figure (55) and the results are summarized in table (12). These cases were performed for constant film thickness. The table shows that the pressures for a diamond case are lesser than a square and similarly an oriented hexagonal shape (with an angled leading edge) gives lesser pressures when compared to a flat leading edged hexagon. Hence, it can be inferred from the results that the shape of the leading edge influences the magnitudes of pressures and consequently the load supports.

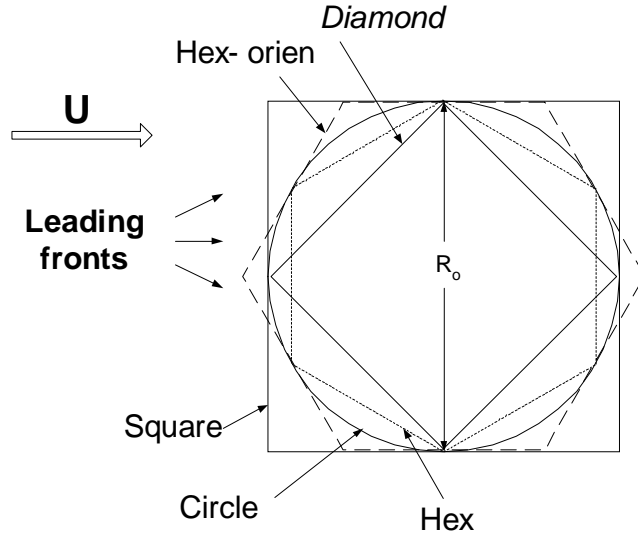


Figure 55: Leading edge shapes of different geometries

Table 12: Peak Pressures for constant film thickness

δ^2	R_o (μm)	<i>Maximum Pressure (Mpa)</i>				
		Circle	Square	Hex - Ori	Hex	Diamond
0.01	50	0.0123	0.0147	0.0121	0.0120	0.0096
0.06	100	0.0197	0.0248	0.0201	0.0200	0.0164
0.13	150	0.0246	0.0297	0.0236	0.0250	0.0209
0.22	200	0.0251	0.0296	0.0243	0.0268	0.0227
0.35	250	0.0223	0.0243	0.0225	0.0264	0.0232

5.7.2 Coefficient of friction

A square asperity in a square pattern offers the advantage of observing the results in the entire range of asperity area fraction, i.e. for $0.0 < \delta^2 < 1.0$. As explained earlier, other geometric shapes do not span this whole range due to the limitations imposed by enlarged asperity widths especially at higher asperity area fractions. Hence the results for a square asperity are illustrated at the outset, to obtain a complete overview.

5.7.2.1 Square Asperity

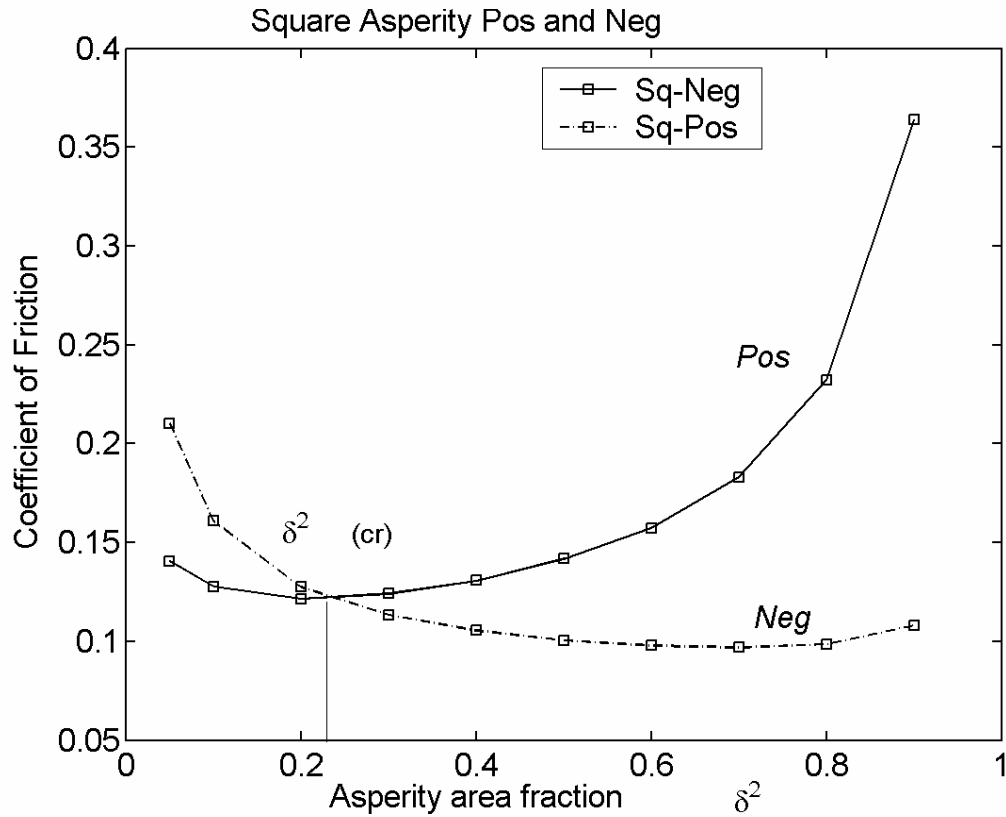


Figure 56: Coefficient of friction for a square positive and negative asperity

Figure (56) shows the comparison of coefficients of friction for positive and negative square asperities, all obtained at a constant load of 0.1 N/mm^2 . In general, the coefficients of friction for a negative asperity are found to be less than those of a positive asperity. For a positive asperity, the coefficient of friction decreases initially and after crossing an optimum point, it ascends with an increasingly larger slope. However, for a negative asperity, the curve exhibits a decreasing slope till it attains a minimum when δ^2 is equal to 0.7 and thereafter, it increases with a small slope. In case of a positive asperity, an asperity area fraction of 0.2 gives the minimum coefficient of friction. It can be observed from the figure that both the minimum values of δ^2 are closer towards the ends of the curves. The graph pertaining to the coefficient of friction for the 2-D analytical model also agrees with the trend observed here.

Figure (56) also shows that both the curves intersect when δ^2 is approximately equal to 0.22. This critical value (δ^2_{cr}) signifies a reversal in the comparative trends of the curves. Accordingly, the curve for a negative asperity, that initially possesses higher values, reverses its trend beyond δ^2_{cr} . Below the critical value, the coefficient of friction is higher due to the generation of higher shear forces caused by larger projected areas (land areas).

In comparison, a constant film thickness condition gives the minimum values of δ^2 as 0.3 and 0.6 for a positive and a negative asperity respectively.

5.7.2.2 Different Geometries

Figure (57) shows the comparative values of coefficient of friction for the positive and negative asperities of all the geometries. It is evident from the figure that there is a close agreement in the trend. A closer look reveals a high correlation of the results for a hexagon and a circle with that of a square, for both the positive and negative asperities. The figure also illustrates that the values are in better agreement for lesser values of δ^2 . This could be due to lesser perceptible differences in geometrical shapes at such values of δ^2 . For higher values of δ^2 , the curves tend to diverge from each other. However, deviations not exceeding 8% were found only in the case of a triangle and this can be attributed due to the increasing difference in its geometric shape when compared to others, at higher asperity area fractions.

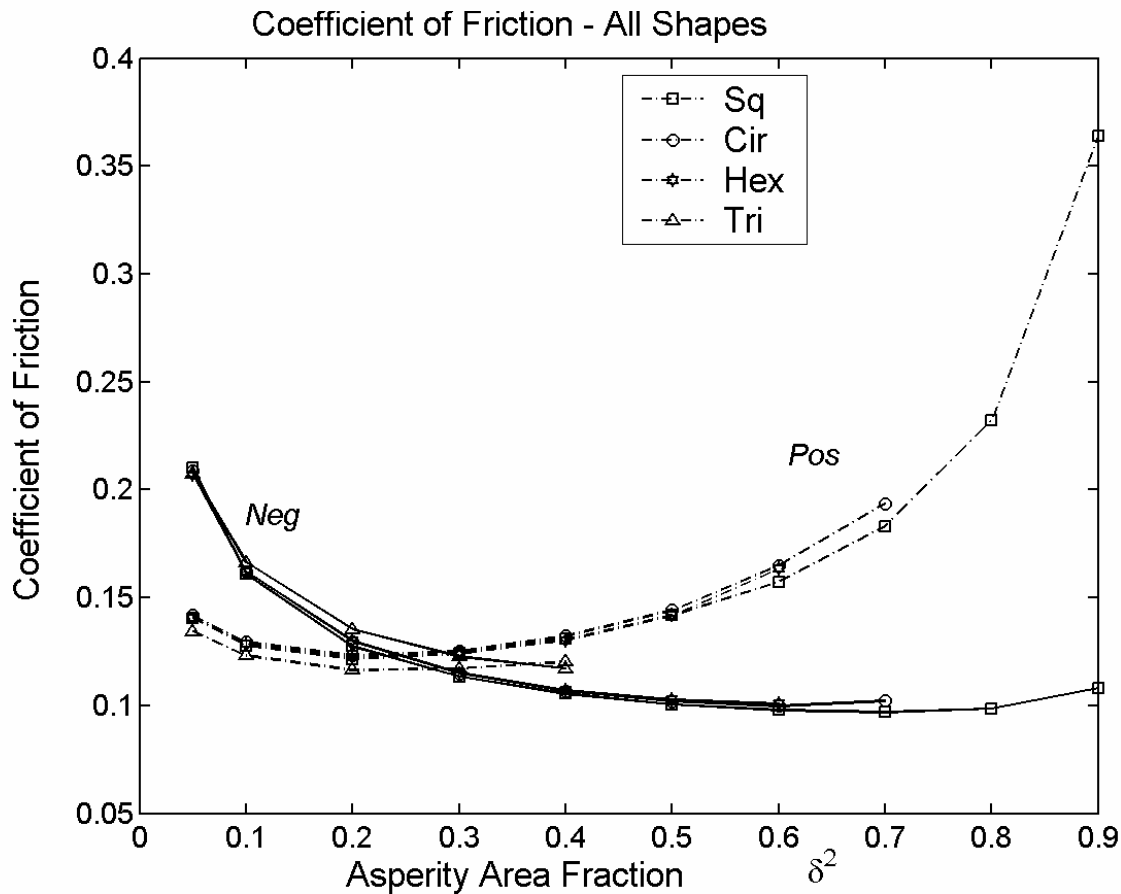


Figure 57: Comparison of coefficient of friction for all the cases

Figure (57) also reveals that all positive asperities of different geometries yield a unique value of δ^2 , equal to 0.2, at which their minimum coefficients of friction are found. Simulations were later run on the available two-dimensional analytical model to verify the existence of a similar trend. Results are given in table (13).

Table 13: Coefficients of friction for the 2-D analytical model

δ^2	<i>0.1</i>	<i>0.2</i>	<i>0.3</i>	<i>0.4</i>	<i>0.5</i>	<i>0.6</i>	<i>0.7</i>	<i>0.8</i>	<i>0.9</i>
<i>f</i>	0.1758	0.1637	0.1716	0.1885	0.2133	0.2547	0.3323	0.529	2.4182

It is observed that the minimum coefficient of friction occurs at the same value of δ^2 as with all the numerical models. This observation reveals the independence of the minimum value of δ^2 both with the asperity layout and also with the asperity shape. In comparison, for a constant film thickness, the analytical model gives a δ^2 value of 0.3; but the numerical models still give the same value of 0.2.

As discussed earlier, figure (56) also shows that for a negative square asperity, minimum value for coefficient of friction is found when asperity area fraction is 0.7. It is found that none of the other shapes attain this asperity area fraction to check the consistency of this value, except for a circle for which minimum coefficient of friction is found when δ^2 is equal to 0.6 instead of 0.7. This appears to be true even for a constant film thickness condition. Analytical solution to a two dimensional negative asperity is unavailable and hence this aspect could not be verified.

The restriction on the asperity area fraction for negative geometries curtails the optimal asperity area fractions to their respective attainable maximum values of δ^2 . Accordingly, in such cases, minimum coefficients of friction are observed at the maximum attainable asperity area fractions.

Finally, the existence of a critical value of asperity area fraction for all the shapes was investigated and found to exist in the range between 0.2 and 0.4 and this can be clearly observed from the same figure (57).

5.7.2.3 Orientation effects

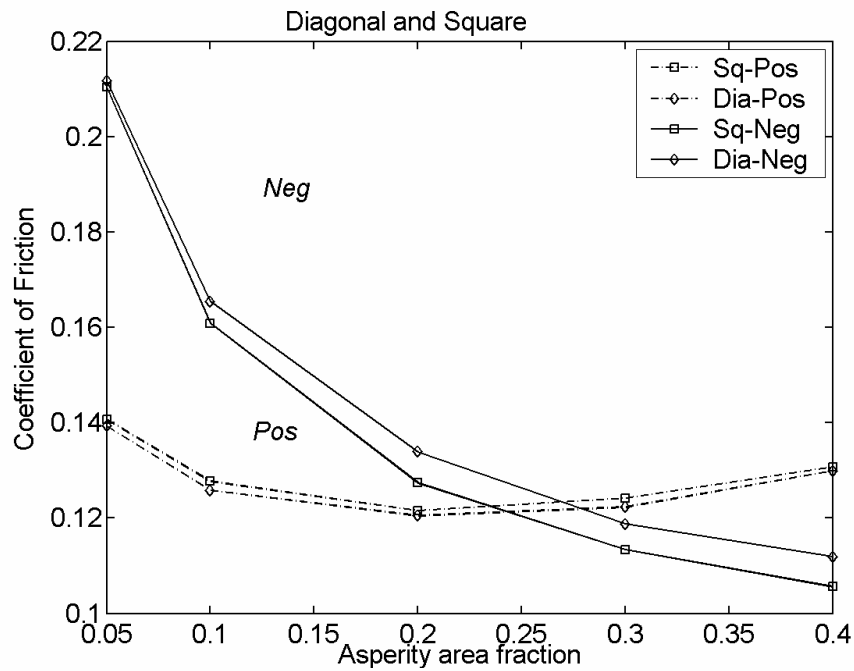


Figure 58: Coefficient of friction for a square and a diamond

The results for a square and a diamond (a square oriented by 45°) shape, both for positive and negative asperities are given in figure (58). For positive asperities, there is a negligible difference (within 2%) whereas for negative asperities, the difference does not exceed a maximum value of 6%.

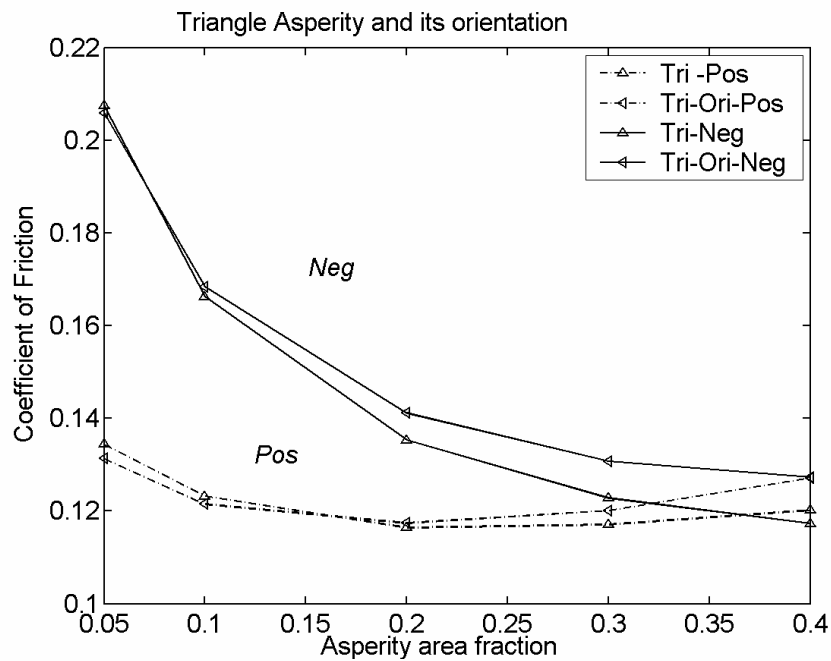


Figure 59: Coefficient of friction for a triangle and its orientation

Similar to the above observation, in case of a positive triangular asperity, coefficients of friction for both the orientations agree with each other better than a negative asperity. The maximum difference of 6 % is noticed at their highest asperity area fraction, as shown in figure (59).

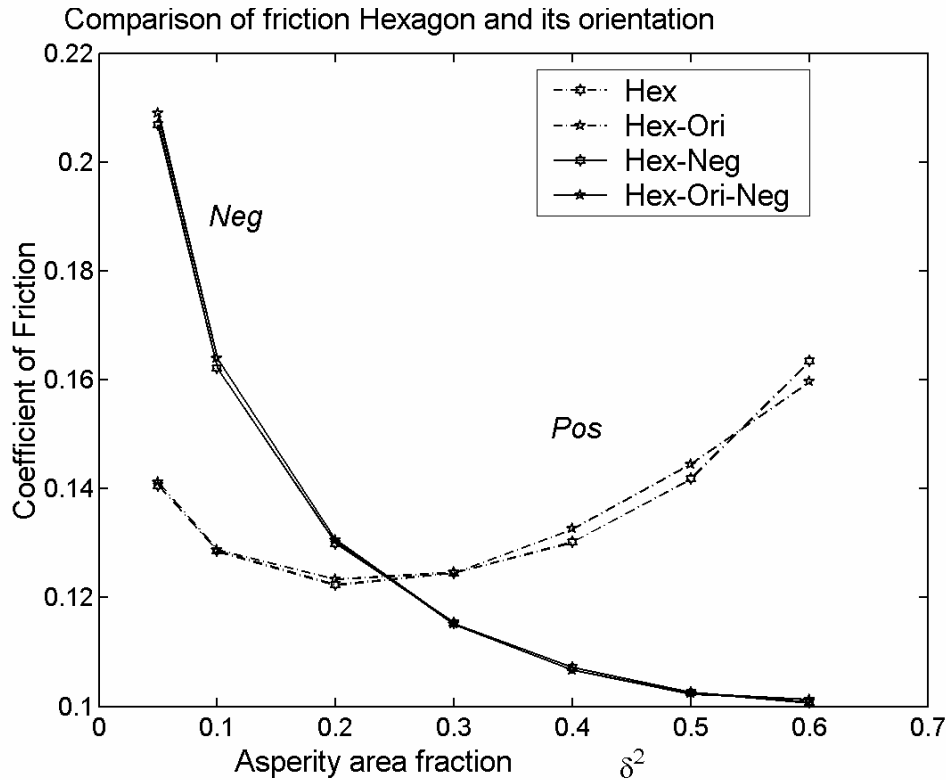


Figure 60: Coefficient of friction for a hexagon and its orientation

Figure (60) shows the results for a hexagon in two different orientations, each differing from the other by 90° orientation. There is a close agreement in both the cases and this can be correlated to a lesser deviation in these geometrical shapes when compared to a triangle or a square. This argument can be further supported by considering the case of a circle, where the results are obvious and are predicted to be the same, irrespective of the orientation. It therefore follows, that a triangle having the least uniformity in shape in different orientations, is more likely to show a wider difference in the results, though not significant, when compared to other regular polygons.

5.7.3 Film thickness

5.7.3.1 Square asperity

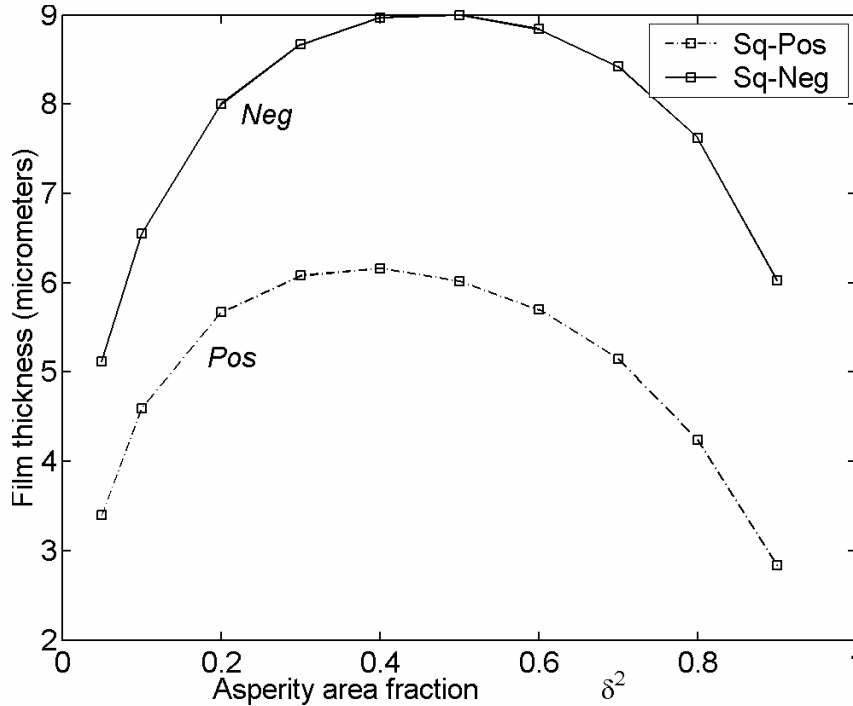


Figure 61: Film thickness of a positive and negative square asperity

Figure (61) shows the film thickness graph for a positive and a negative square asperity. These graphs are convex shaped in contrast to the concave shape found for coefficient of friction (see figure-56). This signifies an inverse relationship between these two properties. It is also observed from the graph that the film thickness values for negative asperities are greater than for positive asperities. This result is expected because, when a negative asperity supports a greater load for a constant film thickness, conversely, it would generate lesser film thickness for a constant load condition. For a positive asperity, the maximum film thickness occurs when asperity area fraction is 0.4 and for a negative asperity, the value is 0.5. Lesser values at the ends are a result of minimal contribution of the respective asperity area fractions in the generation of load support.

5.7.3.2 All cases

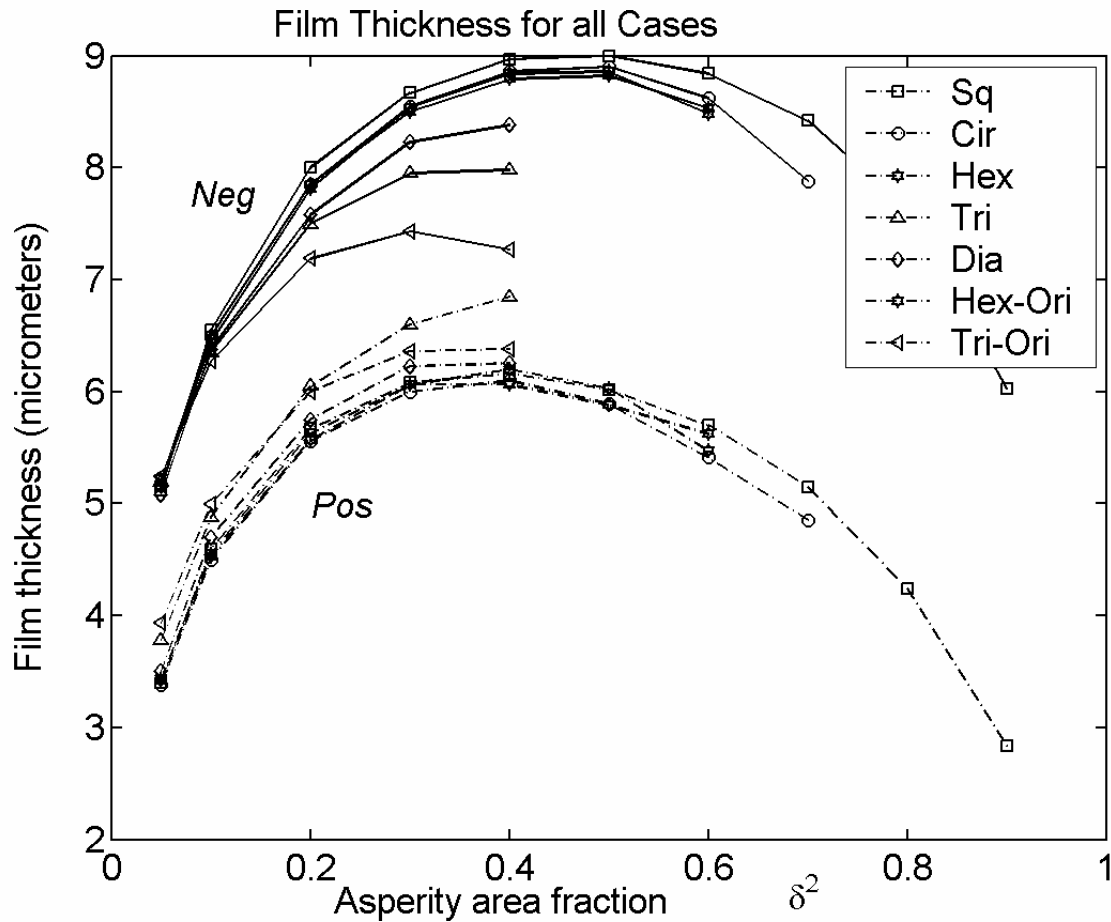


Figure 62: Film thickness results for all the cases

Figure (62) shows film thickness curves for different shapes. As found with the coefficient of friction, the curves for hexagonal, circular and rectangular asperities agree more with each other at lesser values of asperity area fraction. The curves for triangular or diamond shaped asperities deviate more from the general trend as observed before. The film thickness curve of an oriented triangle shows the least magnitude suggesting its advantage over the other negative geometries in terms of leakage.

5.7.4 Leakage (Poiseuille flow)

5.7.4.1 Square Asperity

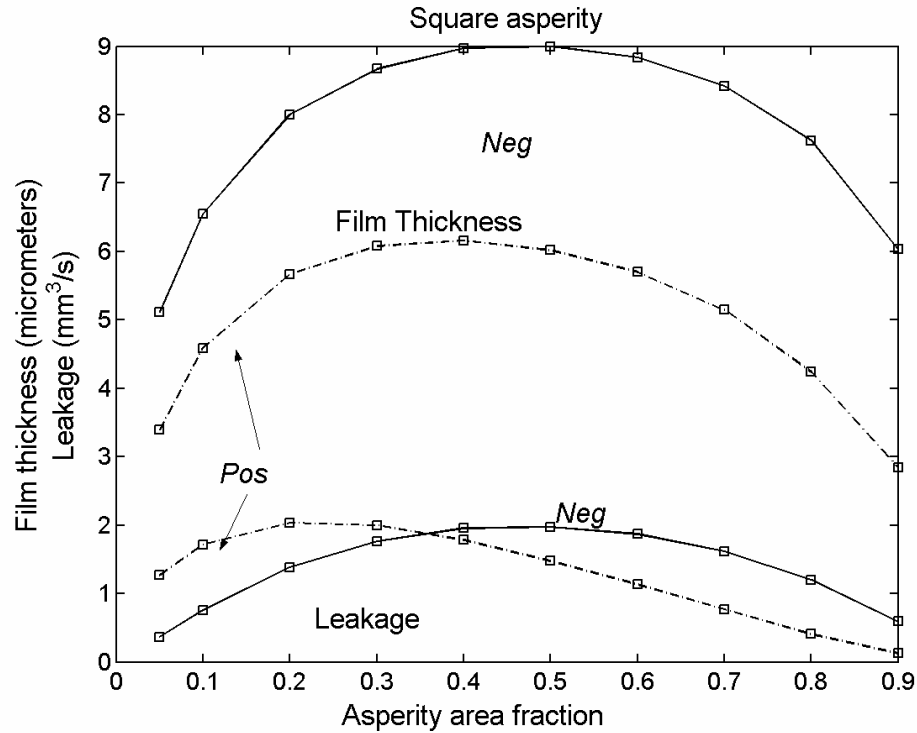


Figure 63: Film thickness and leakage for a square asperity

Leakage occurring due to hydrostatic pressure difference in the radial direction is largely affected by film thickness. Equation (37) estimates leakage for positive asperities and equation (58) is used for negative asperities [7]. Since a positive asperity area fraction provides a blockage for the leakage path, it is factored into the equation (37).

Figure (63) contains the curves for leakage and film thickness for both positive and negative asperities of a square shape. It is clear that leakage generally follows the trend of film thickness. In case of a negative square asperity, leakage is maximum when δ^2 is equal to 0.5 and this agrees with the maximum value observed for film thickness. However, in case of a positive asperity, maximum film thickness occurs when δ^2 is equal to 0.4, whereas for leakage, δ^2 takes the value of 0.2. This is due to the effect of asperity area fraction.

Figure (63) also shows the existence of a critical asperity area fraction, beyond which positive asperities contribute lesser leakage. The critical value is approximately 0.35 for a square asperity. This observation attracts attention especially when it is widely known that a negative asperity generates lesser leakage.

It is worth mentioning that the magnitudes of leakage are of the same order as those found in reference [7].

5.7.4.2 Different Geometries

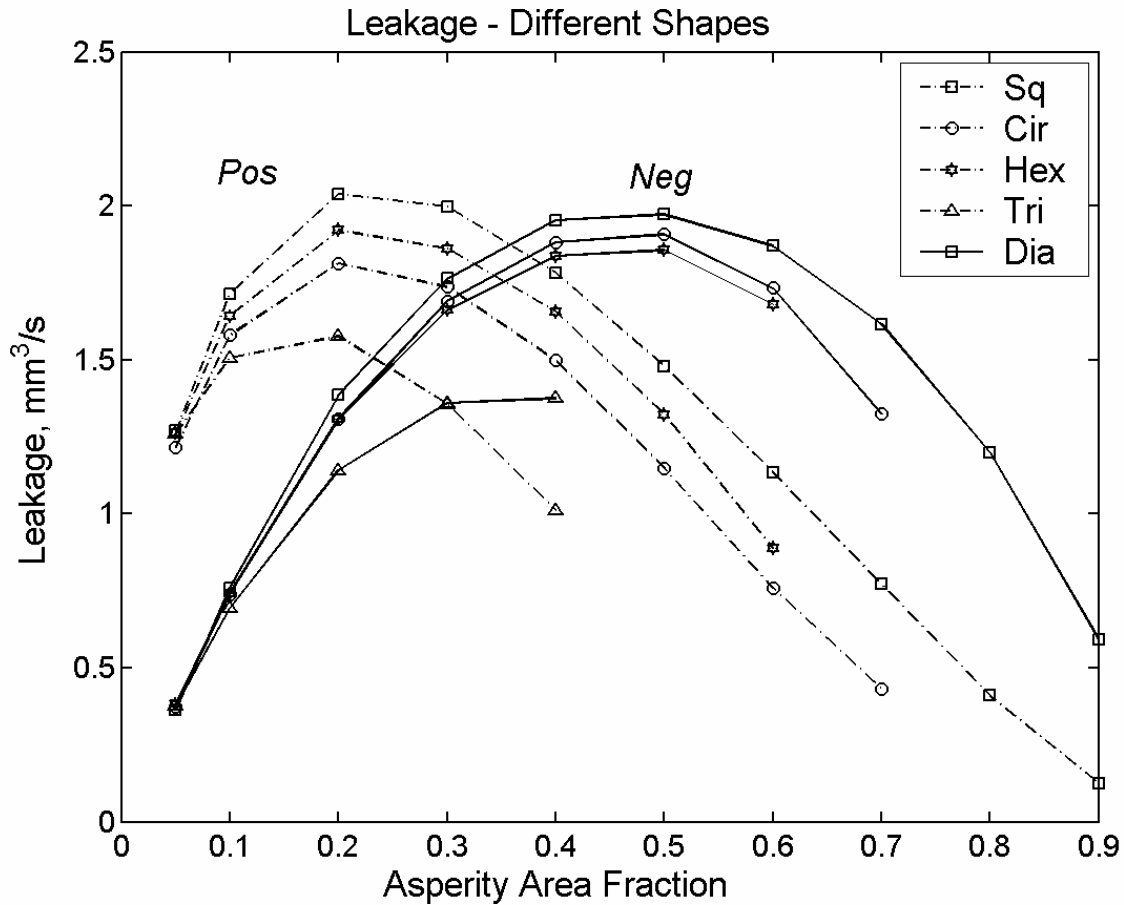


Figure 64: Leakage comparison for different shapes for Poiseuille flow

Figure (64) shows the comparative graph for all the shapes for both positive and negative asperities. All the curves follow the same trend as that observed with a square. The maximum leakage for all positive asperities occurs when asperity area fraction is 0.2. In case of negative asperities, circular and hexagonal shapes show maximum leakage when δ^2 is equal to 0.5, just as found with a negative square asperity. For a negative triangular asperity the maximum leakage occurs when it attains its highest value of δ^2 . It is also observed from the figure that the critical δ^2 values for all the geometries occur between 0.3 and 0.4. In both the positive and negative cases, least amount of leakage is found with a triangle, suggesting its advantage over other geometries.

5.7.4.3 Orientation Effects

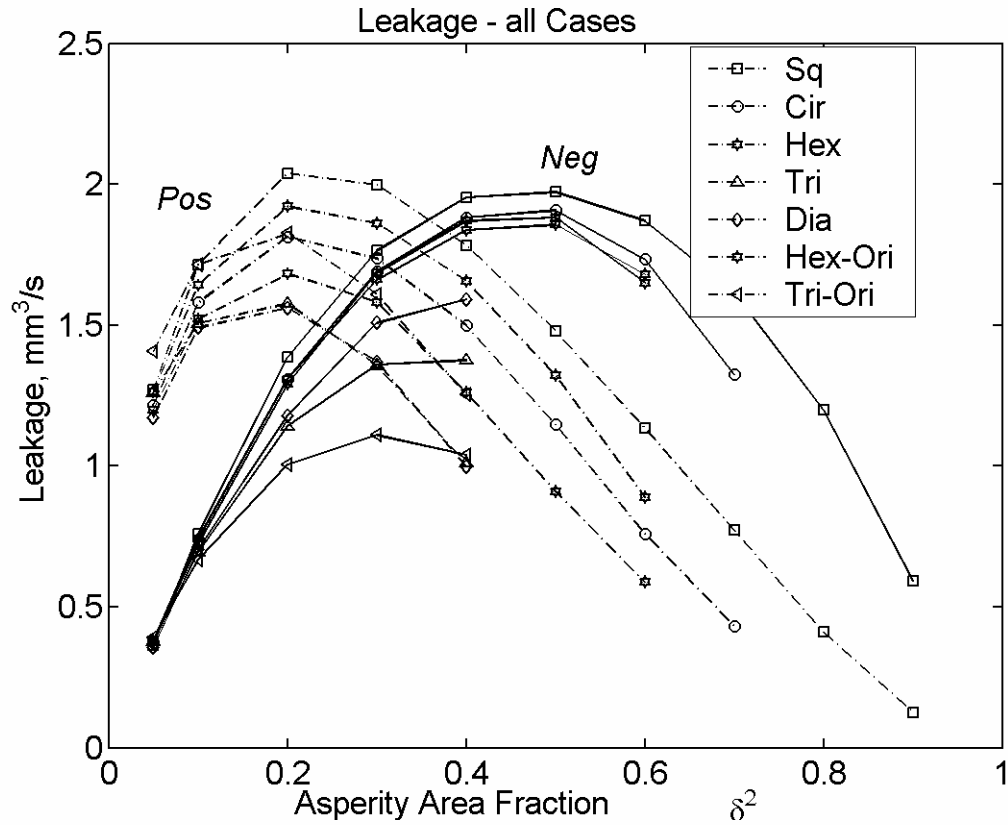


Figure 65: Leakage for all the cases due to Poiseuille flow

Figure (65) contains the curves for all the types of asperities and their orientations. It is observed that there is an agreement in trend among all the positive asperities and also among all the negative asperities. From the graph it is clear that the least values of leakages are found towards either ends of δ^2 values. However, corresponding values of coefficients of friction are high as can be seen from figure (57).

Since both the factors are important for a designer, search may be made for an optimum value within the intermediate range of δ^2 values, between 0.2 and 0.6, by using optimization methods. It may also be observed that this range gives the option of choosing a variety of shapes.

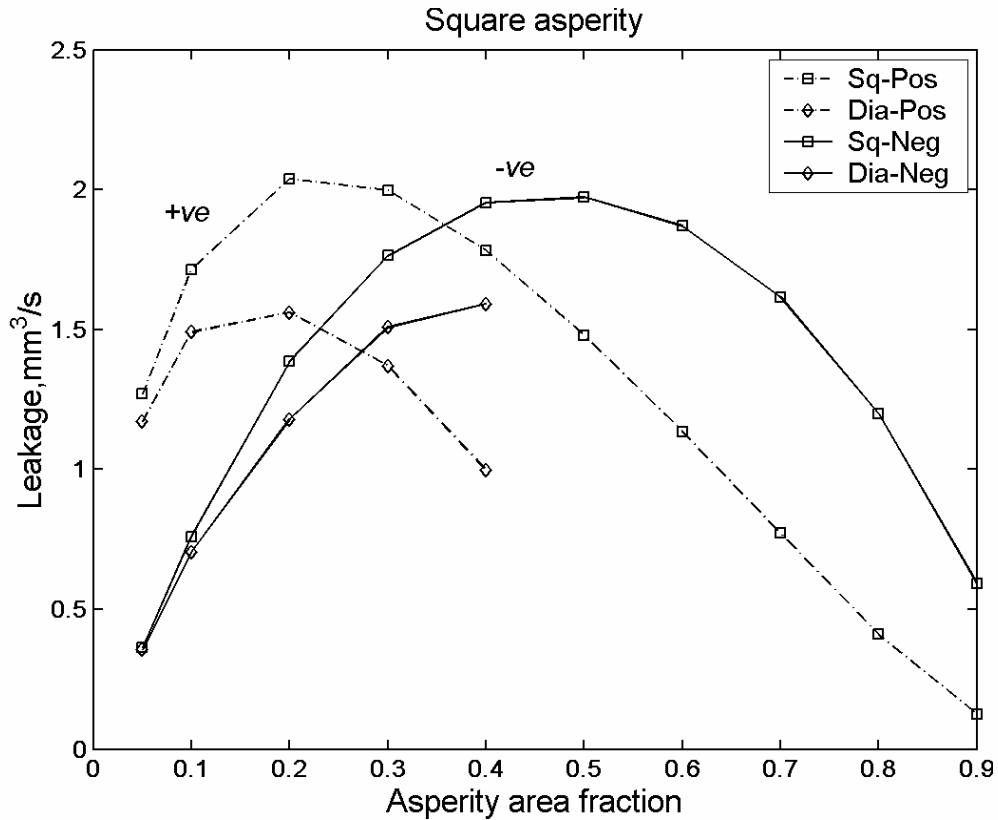


Figure 66: Leakage comparison for square and diagonal asperities

For positive asperities, the largest difference is found between a square asperity and a diamond shaped asperity as shown in figure (66). This difference is directly proportional to the extent of difference in their leakage paths. In case of a diamond, more blockage is offered to the leakage path and hence less leakage results. For a positive triangular case as shown in figure (67), the difference in values is found to be once again due to the variations in leakage paths. In the case of a hexagon, the difference is negligible and for a circle, no differences in values are expected due to its symmetry with respect to orientation.

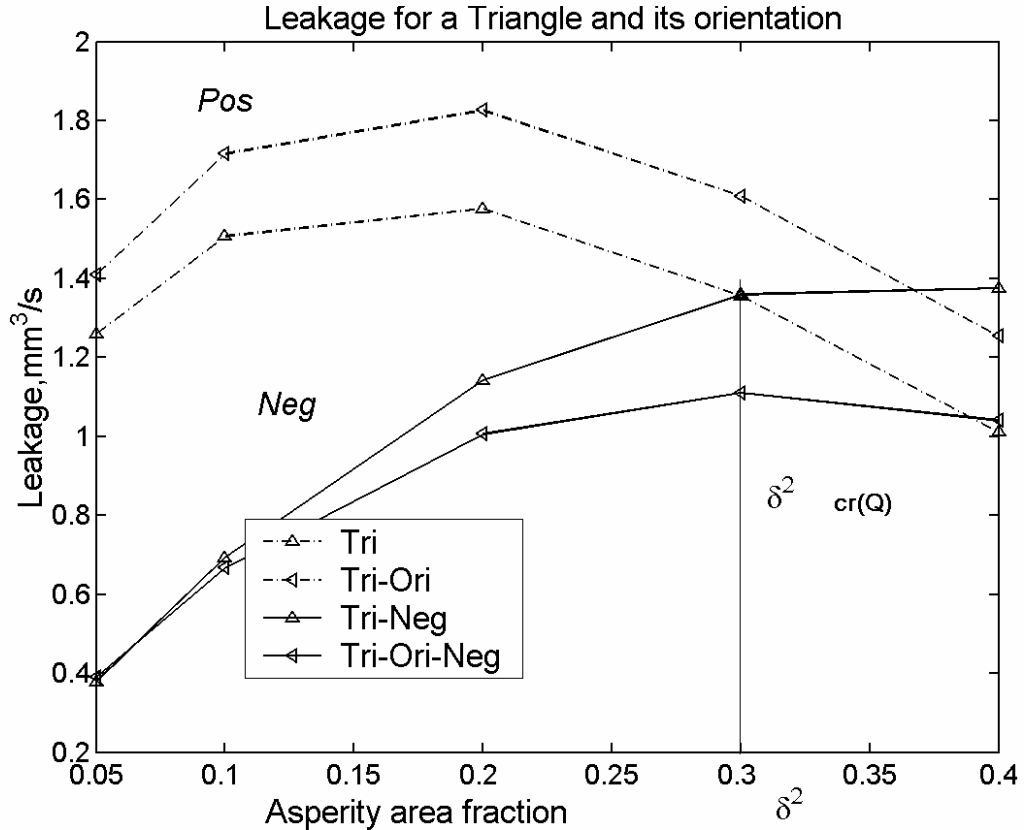


Figure 67: Comparison of leakage for a triangle and its oriented shape

On the other hand, negative asperities do not show practically any difference for a hexagonal and a circular geometry. The difference in the values for a square and a triangle as shown in the same figures (66) and (67) is attributed to the difference in film thickness and not due to asperity area fraction as found in the case of positive asperities. The critical values of δ^2 for different orientations are given later in chapter VI. Again, the values for δ^2 are found to be approximately 0.3.

5.8 RESULTS (with hydrostatic pressure b/c):

The models considered till now have utilized zero pressure boundary conditions in the radial direction both at the outside diameter and the inside diameter of the ring. Also, the models have used only a single asperity instead of a series of asperities across the width of the thrust bearing. In reality, hydrostatic pressure exists at one end and the opposite end is normally exposed to atmospheric pressure. To check the validity of the results obtained earlier, few simulations were again run by considering hydrostatic boundary conditions both with a single asperity and with a row of asperities.

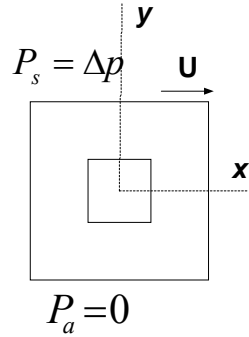


Figure 68: Negative square asperity model

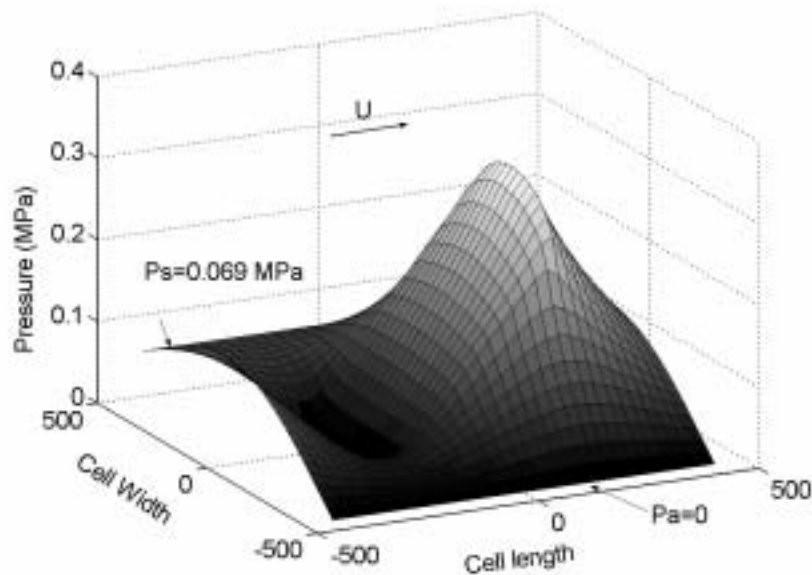


Figure 69: Pressure distribution with hydrostatic pressure b/c

A negative square asperity model and its corresponding pressure distribution are shown in figures (68 & 69). No change in the profile is found except for the magnitude and the appearance of hydrostatic pressure at the outside diameter, as expected. With respect to coefficient of friction, minute variations in magnitudes are caused partly due to marginal difference in load support and due to the use of a coarse mesh. However, it is encouraging to observe that the new results are not in contradiction to those obtained earlier, since the trends of the positive and negative curves remain the same. As found before, there is a critical asperity area fraction at which a reversal in the relative magnitudes is observed. This critical value occurs between the values of 0.2 and 0.3 for δ^2 , not different to what was observed earlier. The minimum coefficient of friction for a positive asperity is found when asperity area fraction is equal to 0.2 and for a negative asperity it is equal to 0.7. Until now, the values of coefficient of friction have been obtained by neglecting the effects of pressure gradients as given in equation (33), as the difference is found to be merely around 5 %. See table (14) for details.

Table 14: Comparative values of c.o.f. for a positive square asperity

δ^2	0.1	0.2	0.3	0.4	0.5	0.6	0.7	0.8
<i>Coefficient of friction (1)</i>	0.1172	0.1124	0.1127	0.1180	0.1275	0.1406	0.1615	0.1984
<i>Coefficient of friction (2)</i>	0.1207	0.1167	0.1178	0.1236	0.1336	0.1470	0.1679	0.2045

(1)- with out pressure gradient effects

(2)- with pressure gradient effects

Results obtained for film thickness are also found comparable to earlier results with a minimal difference in magnitude, as expected due to additional load support. However, the results for the show a sizable change in the magnitude, though the trend remains the same, except for the optimal points. For a positive asperity, the maximum leakage occurs when δ^2 is equal to 0.3 when compared to a value of 0.2 as found before. For a negative asperity, δ^2 is equal to 0.7 as against a value of 0.6. This could be due to the use of a coarse mesh which may be verified during subsequent researches. Table (15) shows the comparative leakage values obtained by both the pressure gradients existing at the exit and also by the Poiseuille method.

Table 15: Comparative leakage values for a positive square asperity

δ^2	0.1	0.2	0.3	0.4	0.5	0.6	0.7	0.8
<i>Leakage</i> (Poiseuille mm^3/s)	2.14	2.51	2.58	2.31	1.92	1.49	1.03	0.59
<i>Leakage</i> (press grad mm^3/s)	70.30	91.97	101.50	100.20	86.37	73.92	58.00	39.36

The values for leakage with this new approach are clearly very high. Investigation revealed that leakage is found to be in agreement with the magnitudes of pressure gradients observed at the exit. The expression used for leakage with the first approach is based on Poiseuille flow. It is a function of pressure gradients in the radial direction whose values are quite less when compared to the exit pressure gradients. This explains for the difference in the magnitudes. It is expected that with low hydrostatic pressures when compared to the magnitudes of hydrodynamic pressures, Poiseuille formula may be applied to get an estimate of leakage. The veracity of the data can be established through experiments in subsequent studies.

Finally, results for coefficient of friction and film thickness respectively for a radial model with three asperities have also shown similar trends as obtained earlier, in support of the use of a single cell model for this present study.

5.9 CONTINUITY OF FLOW

Table 16: Continuity of flow with the first approach

<i>Variables</i>	<i>Tangential flow</i>		<i>Radial flow</i>	
	At the exit	At the entry	At O.D	At I.D.
	<i>mm³/s</i>	<i>mm³/s</i>	<i>mm³/s</i>	<i>mm³/s</i>
<i>Coarser mesh</i>	9.3002	9.2404	0.8957	-0.8956
<i>Finer mesh</i>	9.1320	9.1101	0.9462	-0.9462

Table (16) shows the continuity of flow results for a single square asperity with the first approach. A coarser mesh gives smaller differences in values for both the tangential flow and the radial flow. However, as the mesh size is increased, the differences are narrowed. The following equations have been used to compute the leakage flow:

$$Q_y = \int q_y dx = \int_{-L/2}^{L/2} \left(-\frac{h^3}{12\mu} \frac{\partial p}{\partial y} \right) dx \quad \text{in the radial direction}$$

$$Q_x = \int q_x dy = \int_{-L/2}^{L/2} \left(-\frac{h^3}{12\mu} \frac{\partial p}{\partial x} + \frac{Uh}{2} \right) dy \quad \text{in the circumferential direction}$$

The magnitudes of pressure gradients and the velocities are the equal at the entry and the exit in the circumferential direction. The slopes of pressure gradients are positive at these two points for a Reynolds condition. Hence, the circumferential flow rates (Q_x) are equal. Flow rates in the radial direction (Q_y) are also expected to be of equal magnitude since pressure gradients are the same at both the boundaries (no velocity effects are considered). However, the flows are in opposite directions as shown by the negative sign in the table, resulting in a net outflow from a single cell. Thus, the flow quantities do not add up to support conservation of flow for a two dimensional Reynolds condition unlike a one dimensional case.

Table 17: Comparison of continuity of flow

<i>Variables</i>	<i>Tangential flow</i>		<i>Radial flow</i>	
	At the exit	At the entry	At O.D	At I.D.
	<i>mm³/s</i>	<i>mm³/s</i>	<i>mm³/s</i>	<i>mm³/s</i>
<i>First approach</i>	12.5358	12.4617	0.9920	-0.9920
<i>Second approach</i>	12.4206	12.3593	0.5946	-1.0368

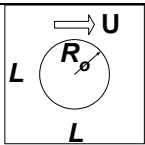
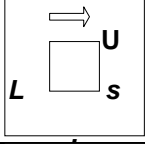
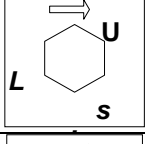
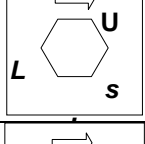
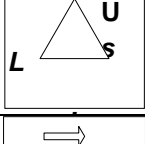
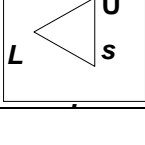
Table (17) shows the comparison of continuity of flow results for a given square asperity for both the cases of boundary conditions taken with a coarser mesh. While a better agreement in data is observed with the first approach, application of hydrostatic boundary condition yields a difference in radial flow, as expected. This is clearly due to the difference in pressure gradients at the radial boundaries. As noted earlier, a net outflow is also observed with the second approach. This discrepancy may be sorted out by using CFD methods that employ Navier Stokes equation in finding a solution. It is also expected that the effects of velocities in the radial direction may clearly emerge by this method, and possibly this may provide explanation for the differences found in conservation of flow.

Chapter VI: SUMMARY, CONCLUSION AND FUTURE WORK

6.1 SUMMARY

This work utilized numerical modeling techniques to explore the effects of the shapes of different asperity geometries on lubrication characteristics, for a simple thrust slider application at constant load conditions. Various regular shapes consisting of square, circular, hexagonal and triangular asperities, all distributed in a square array, are considered. Results for friction and leakage parameters are presented. Table (18) summarizes the critical data obtained from the numerical simulations.

Table 18: Critical data from the results

<i>S.No.</i>	<i>Unit Cell</i>	<i>Type</i>	δ^2 <i>(opt)</i>	δ^2 <i>(cr)</i>	<i>f</i>	<i>Q</i> <i>(mm³/s)</i>	<i>b</i> <i>(μm)</i>	<i>Pmax</i> <i>(Non-Dim)</i>
1		Positive	0.2	0.32	0.1234	1.8136	5.56	4.6536
		Negative	0.6		0.0997	1.8824	8.62	3.0808
2		Positive	0.2	0.35	0.1216	2.039	5.67	5.0611
		Negative	0.7		0.0969	1.9533	8.42	3.0945
3		Positive	0.2	0.34	0.1223	1.9207	5.63	4.7421
		Negative	0.6		0.1007	1.8380	8.53	3.2018
4		Positive	0.2	0.28	0.1234	1.6821	5.57	4.3754
		Negative	0.6		0.1013	1.8696	8.48	2.9374
5		Positive	0.2	0.3	0.1164	1.5771	6.05	4.5582
		Negative	0.4		0.1173	1.3753	7.98	3.2662
6		Positive	0.2	0.3	0.1174	1.8262	6.0	2.9559
		Negative	0.4		0.1273	1.0399	7.27	3.8686

6.2 CONCLUSION

It is important to know that the results are specific to the cases considered here and, though some of them such as, the existence of a transition point could be true even for other models, no general conclusions may be made in the absence of supporting data. Some salient conclusions are listed below.

- Unlike constant film thickness, for a constant load condition a transition point for asperity area fraction clearly exists both for leakage and coefficient of friction.
- The effect of asperity shape is minimal on coefficient of friction. However, both the size and the type of asperity (positive and negative) affect coefficient of friction values.
- Leakage is affected not only by the size of an asperity, but also by its shape, both for positive and negative asperities.
- The least coefficient of friction for all positive asperities is found when δ^2 is equal to 0.2, whereas for the negative ones, the values are found at their maximum asperity area fractions, except for a square and a circle.
- For lesser values of δ^2 , negative asperities give higher coefficient of friction. However, there exists a critical asperity area fraction beyond which negative asperities of all the considered shapes give lesser coefficients of friction their positive counterparts.
- As a contradiction to the common perception, negative asperities are found to produce lesser leakage in certain ranges of asperity area fraction. This transition value is found to be between 0.3 and 0.4 values of δ^2 for all the types of asperities.
- Triangular geometry gives the least leakage for the range of shapes considered here. Hence for a given asperity area fraction, this can be a preferred asperity geometry in an application where leakage is to be kept to the minimum.
- Reduction in leakages can be further obtained by orientating a shape. This is found true for all cases except for a positive triangle where, by orientating the triangle, more leakage follows due to lesser blockage path.
- The trends observed with a square model have been verified to be correct with those found with a radial model in support of its validity, as a first approximation.
- Numerical simulations with hydrostatic pressure boundary conditions for a square asperity also show no difference in the trend, both for the coefficient of friction and leakage, reinforcing the earlier observation of a transition (critical) point. However, relative magnitudes for different shapes need not be similar to those found before, both for coefficient of friction and leakage, since the values for load support change.
- Though found less for a turbulent flow, Reynolds numbers have been observed to be high, suggesting non-negligible inertial effects. This is due to higher velocities.

6.3 FUTURE WORK

- The results obtained in this study are to be revalidated by using a radial model with hydrostatic boundary conditions.
- Comparison of the results need to be made with experimentation work and accordingly models are to be refined, if necessary.
- The amount of leakage found with the second approach of hydrostatic boundary conditions appears to be quite high. Experimental work should give us an indication of the magnitude of leakage and also reveal the validity of Poiseuille flow. Leakage models may then be refined, if necessary using rotation and other effects as suggested in [7].
- Alternatively, CFD methods may be used to give us a better assessment of leakage values and also facilitate verification of continuity of flow.
- CFD methods may be used, also to find out the effects of vortices (at the leading and the trailing edges of the asperities) on the pressure distribution when a pure lubricant is used, implying the elimination of cavitation effects.
- Use of CFD methods would also take care of the inertial effects caused to high Reynolds numbers.
- Models may be improved to take surface roughness into account.
- The computer codes may be improved to automate the process of finding film thickness for a constant load to the desired accuracy.

Appendix

A.1 NOMENCLATURE

F = Friction force per unit cell

L = Periodic length of the unit cell

N = Number of asperities per unit area

P_a = Atmospheric pressure

P_{avg} = Average pressure per unit cell = $\frac{W}{L^2}$

P_c = Cavitation pressure

P_s = Sealing (supply) pressure

Q = Leakage rate

R_o = Equivalent asperity radius

U = Slider velocity

W = Load support per unit cell

a = Asperity height

b = Film thickness

f = Coefficient of friction

p = pressure

q = Leakage rate per unit width

r_0 = Inner radius of the thrust ring

r_1 = Outer radius of the thrust ring

s = Side of a square/triangle/hexagon

Δp = Differential hydrostatic pressure ($P_s - P_a$)

δ = Step length ratio = $\frac{2R_o}{L}$

δ^2 = Asperity area fraction

μ = viscosity of lubricant

τ = Shear stress

τ_{avg} = Average shear stress = $\frac{F}{L^2}$

A.2 MATLAB® SCRIPT FILES

A.2.1 Film Thickness Models

A.2.1.1 Hexagonal Model

A positive hexagonal asperity inscribed in a circle of radius, R_{oo}

```
%% Input N, d, a and b
N=865.0519; % No of asperities/in^2
d=0.1; % Asperity area fraction
a=5*40e-6; % Asperity Height in inches
b=4.88*40e-6; % Film Thickness in inches

%% Other input data
v=42*0.145e-6; % Viscosity in Reyns
u=261.7994; % Velocity in in/s
Pc=0; % Cavitation Pressure

% Derived Data
L=2*sqrt(1/(4*N)); % Unit Cell Length
A2=L^2; % Unit Cell Area
A1=d*A2; % Area of asperity
Ro=sqrt(A1/pi); % Equivalent radius of the traingle
Roo=sqrt(pi*Ro^2/3/sin(pi/3)); % Outer radius of the hexagon

% Mesh Size
ndiv=34*1; % Number of grid points in a unit cell
x=linspace(-L/2,L/2,ndiv);
y=linspace(-L/2,L/2,ndiv);
dx=x(2)-x(1);
dy=dx;
m=length(y);
n=length(x);

%% Film Thickness Equation
for i=1:m
for j=1:n
if (x(j)>=-Roo*cos(pi/6) & x(j)<=Roo*cos(pi/6))&...
y(i)<=((-1/cos(pi/6)+tan(pi/6))*x(j)+Roo)&...
y(i)<=((1/cos(pi/6)-tan(pi/6))*x(j)+Roo)&...
y(i)>=((1/cos(pi/6)-tan(pi/6))*x(j)-Roo)&...
y(i)>=((-1/cos(pi/6)+tan(pi/6))*x(j)-Roo)
h(i,j)=b;
else
h(i,j)=a+b;
end
end
end
end
```

A.2.1.2 Triangular Model

A positive triangular asperity inscribed in a circle of radius, R_{oo}

```
%% Input N, d, a and b
N=865.0519; % No of asperities/in^2
d=0.1; % Asperity area fraction
a=5*40e-6; % Asperity Height in inches
b=4.88*40e-6; % Film Thickness in inches

%% Other input data
v=42*0.145e-6; % Viscosity in Reyns
u=261.7994; % Velocity in in/s
Pc=0; % Cavitation Pressure

% Derived Data
L=2*sqrt(1/(4*N)); % Unit Cell Length
A2=L^2; % Unit Cell Area
A1=d*A2; % Area of asperity
Ro=sqrt(A1/pi); % Equivalent radius of the traingle
Roo=sqrt(pi*Ro^2/(cos(pi/6)*(1+sin(pi/6)))); % Outer Radius of Triangle

% Mesh Size
ndiv=34*1; % Number of grid points in a unit cell
x=linspace(-L/2,L/2,ndiv);
y=linspace(-L/2,L/2,ndiv);
dx=x(2)-x(1);
dy=dx;
m=length(y);
n=length(x);

%% Film Thickness Equation
for i=1:m
for j=1:n

if (x(j)>=-Roo*cos(pi/6) & x(j)<=Roo*cos(pi/6))&...
(y(i)<=(Roo+Roo*sin(pi/6)) & y(i) >=-(Roo+Roo*sin(pi/6))/2)&...
(y(i)<=(sec(pi/6)+tan(pi/6))*x(j)+Roo*(0.5+0.5*sin(pi/6)))&...
(y(i)<=(-sec(pi/6)-tan(pi/6))*x(j)+Roo*(0.5+0.5*sin(pi/6)))
h(i,j)=b;
else
h(i,j)=a+b;
end
end
end
end
```

A.2.1.3 Radial Model

```
%% Input N, Nr, d, a and b
N= 1612.9; % No of asperities/ in^2 (2.5 /mm^2)
Nr= 3; % No of asperities in a row
d= 0.4; % Asperity area fraction
a= 7.8*40e-6; % Pore Depth
b= 7.0*40e-6; % Min film thickness

%% Other input data
v=42*0.145e-6; % Viscosity in Reyns
u=261.7994; % Velocity in in/s
Pc=0; % Cavitation Pressure

% Derived Data
L=2*sqrt(1/(4*N)); % Unit Cell Length
yn= -Nr*L/2; % Negative X coordinate
yp= Nr*L/2; % Positive X coordinate
xn= -L/2; % Negative Y coordiante
xp= L/2; % Positive Y coordiante
A2=4*xp*yp; % Unit Cell Area
A1=d*A2; % Area of asperity
rp=sqrt(A1/Nr/pi); % Radius of the pore
yc= [-L/2 0 L/2]*2; % coordinates of pore centers
xc= [0 0 0];

% Mesh Size
ndiv=34*1; % Number of grid points in a unit cell
x=linspace(xn,xp,ndiv);
y=linspace(yn,yp,ndiv*yp/xp);
dx=x(2)-x(1);
dy=dx;
m=length(y);
n=length(x);

% Film Thickness Equation
for i=1:m
    for j=1:n
        d1=sqrt((x(j)-xc(1))^2+(y(i)-yc(1))^2);
        d2=sqrt((x(j)-xc(2))^2+(y(i)-yc(2))^2);
        d3=sqrt((x(j)-xc(3))^2+(y(i)-yc(3))^2);
        if d1<=rp | d2 <=rp | d3<=rp
            h(i,j)=a+b;
        else
            h(i,j)=b;
        end
    end
end

end
end
```

A.2.2 Analytical 1-D Step Slider Solution

```

    % Input
    a=5*40e-6;          % asperity height (a)
    b=3*40e-6;          % Film thickness (b)
    Ro=3.0e-3;          % Asperity radius (Ro)
    R1=15e-3;           % Periodic Length (R1)
    u=50;                % Speed in/s
    v=1.65e-6;          % Viscosity reyns
    Pc=0;                % Cavitation Pressure
    id=0.883;           % radii and delta_p of ring
    od=1.267;           % outer dia
    dp=10;              % delta p across the seal
    del=Ro/R1;          % Since it is 1-D, 'Ro&R1' are not squared
    h1=a+b;
    N= 1/(pi*R1^2);     % No of asperities / in^2

    ndiv=65*4;
    r=linspace(-R1,R1,ndiv);

    DEN=(h1^3*Ro+b^3*(R1-Ro));

    % Main Program
    for i=1:ndiv

        if r(i)<=-Ro
            %left portion
            PP(i)=6*v*u*(h1-b)*Ro*(R1+r(i));
            P(i)=PP(i)/DEN;
        elseif r(i)>=Ro
            %right portion
            PP(i)=6*v*u*(h1-b)*Ro*(r(i)-R1);
            P(i)=PP(i)/DEN;
        else
            %step portion
            PP(i)=-6*v*u*(h1-b)*r(i)*(R1-Ro);
            P(i)=PP(i)/DEN;
        end
    end

end

```

A.2.3 Numerical 1-D Positive Step Slider Solution

```
% Input
h1=8*40e-6;           % total film thickness
h2=3*40e-6;           % minimum film thickness
U=50;                 % speed in in/s
v=1.65e-6;            % Viscosity in Reyns
R1=15e-3;             % Unit cell Length in inches
Ro=10e-3;             % Step Length in inches

%Mesh Size:
ndiv=65;
x=linspace(-R1,0,ndiv);
dx=x(2)-x(1);

% Film Thickness
for i=1:ndiv
    if (x(i) >= -Ro)
        h(i)=h2;
    else
        h(i)=h1;
    end
end

po=zeros(ndiv,1);     % pressure vectors for 2 sets of values
pn=zeros(ndiv,1);     %

% main program
e=1;                  % initializing error
while e > 1e-5        % checking the condition for desired error
    po=pn;

    for i=2:(ndiv-1)
        hl=(h(i)+h(i-1))/2;           % film thk to left
        hr=(h(i)+h(i+1))/2;           % film thk to right

        %Equation for pressure
        dd=(hr)^3/(hl^3+hr^3);
        ee=hl^3/(hl^3+hr^3);
        ff=6*v*U*dx*(hr-hl)/(hl^3+hr^3);
        pn(i)=((dd)*po(i+1)+(ee)*po(i-1)-(ff));

    end
    e=(sum(abs(pn-po)))/((sum(abs(po)))+eps);
end
```

A.2.4 Analytical 2-D Hex Layout Solution

```

    % Input
Ra= 1.0625;           % Average radius of the ring in inches %
a= 7*40e-6;          % Asperity Height in inches
b= 7.8*40e-6;        % Film Thickness in inches
c= (a+b)^3;
v= 42*0.145*1e-6;    % viscosity in Reyns %
N=1612.9;            % No of asperities/ in^2 (2.5 /mm^2)%
R1=sqrt(1/(pi*N));    % Outer Radius in inches %
n=2500;              % RPM
u= 2*pi*Ra*n/60;     % velocity in in/s %

Ro=11e-3;            % Asperity radius 550 microns
d= Ro^2/R1^2;        % asperity area fraction %
g= (1+d)/(1-d);      % gamma - a ratio %

Pi= 0.0;             % ambient pressure in psi%
Pc= 0.0;             % cavitation pressure in psi%
Po= Pi-Pc;

    % Mesh Size
th= 0:pi/16:2*pi;    % mesh in circumferential direction
r= 0:R1/41:R1;       % mesh in the radial direction %
dr= r(2)-r(1);
dtheta=th(2)-th(1);

    % Pressure Distribution %
for k=1:1
for j=1:33
for i=1:42
    x(i,j)=r(i)*cos(th(j));
    y(i,j)=r(i)*sin(th(j));
    if r(i)<=Ro
        P(i,j,k)= -6*v*u(k)*a*r(i)/(b^3+g*c)*cos(th(j))+Pi;
    else
        P(i,j,k)=-6*v*u(k)*a*Ro^2/(r(i)*(b^3+g*c))*...
        cos(th(j))*(R1^2-r(i)^2)/(R1^2-Ro^2)+Pi;
    end
end
end
end

```

A.2.5 Numerical 2-D Square Asperity Solution

```

    % Input data
N=865.0519;           % No of asperities / in^2
d=0.2;               % Asperity Area fraction
v=42*0.145e-6;      % Viscosity in Reyns
u=261.7994/5*2;     % Velocity inn in/s
Pc=0;               % Cavitation Pressure
dp=10;              % delta P across the seal in psi
r0=0.883/2;         % Inner Radius of the Seal in inches
r1=1.236/2;         % Outer Radius
a=5*40e-6;          % Asperity Height in inches
b=5.01*40e-6;       % Film thickness

L=2*sqrt(1/(4*N));  % Unit Cell Length
B=L;                % Unit cell width
s1=sqrt(d*L*B);     % Asperity length
s2=s1;              % Asperity width

    % Mesh Size
ndiv = 34*1;
x = linspace(-L/2,L/2,ndiv);
y = linspace(-B/2,B/2,ndiv);
dx =x(2)-x(1);
dy =B/L*dx;
m=length(y);
n=length(x);

    % Film Thickness Equation
for i=1:m
for j=1:n
    if (x(j)>=(-s1/2) & x(j)<=(s1/2)) & (y(i)>=-(s2/2) & y(i)<=(s2/2))
        h(i,j)=b;
    else
        h(i,j)=a+b;
    end
end
end

    % Initial Values%
Po=zeros (m,n);
P=zeros (m,n);

    % SOR - parameter
omega=4/(2+sqrt(4-(cos(pi/(n-1))+cos(pi/(m-1))))^2));

```



```

    % Solving Reynolds Eqn (Poisson's) iteratively
err=1;
while err>1e-6
Po=P;

for i=2:m-1
for j=1:n
if j==1
hu=(h(i,j)+h(i+1,j))/2;
hd=(h(i,j)+h(i-1,j))/2;
hr=(h(i,j)+h(i,j+1))/2;
hl=(h(i,j)+h(i,n-1))/2;
hx=((hr)^3+(hl)^3)/dx^2;
hy=((hu)^3+(hd)^3)/dy^2;
a1=hr^3/dx^2/(hx+hy);
a2=hl^3/dx^2/(hx+hy);
a3=hu^3/dy^2/(hx+hy);
a4=hd^3/dy^2/(hx+hy);
a5=-6*v*u*(hr-hl)/(dx)/(hx+hy);
P(i,j)=(a1*Po(i,j+1)+a2*P(i,n-1)+a3*Po(i+1,j)+a4*P(i-1,j)+a5);
P(i,n)=Po(i,1);
elseif j==n
hu=(h(i,j)+h(i+1,j))/2;
hd=(h(i,j)+h(i-1,j))/2;
hr=(h(i,j)+h(i,2))/2;
hl=(h(i,j)+h(i,j-1))/2;
hx=((hr)^3+(hl)^3)/dx^2;
hy=((hu)^3+(hd)^3)/dy^2;
a1=hr^3/dx^2/(hx+hy);
a2=hl^3/dx^2/(hx+hy);
a3=hu^3/dy^2/(hx+hy);
a4=hd^3/dy^2/(hx+hy);
a5=-6*v*u*(hr-hl)/(dx)/(hx+hy);
P(i,j)=(a1*Po(i,2)+a2*P(i,j-1)+a3*Po(i+1,j)+a4*P(i-1,j)+a5);
P(i,1)=Po(i,n);
else
hu=(h(i,j)+h(i+1,j))/2;
hd=(h(i,j)+h(i-1,j))/2;
hr=(h(i,j)+h(i,j+1))/2;
hl=(h(i,j)+h(i,j-1))/2;
hx=((hr)^3+(hl)^3)/dx^2;
hy=((hu)^3+(hd)^3)/dy^2;
a1=hr^3/dx^2/(hx+hy);
a2=hl^3/dx^2/(hx+hy);
a3=hu^3/dy^2/(hx+hy);
a4=hd^3/dy^2/(hx+hy);

```

```

a5=-6*v*u*(hr-hl)/(dx)/(hx+hy);
P(i,j)=(a1*Po(i,j+1)+a2*P(i,j-1)+a3*Po(i+1,j)+a4*P(i-1,j)+a5);
end
P(i,j)=Po(i,j)+omega*(P(i,j)-Po(i,j));
P=P.*(P>0);          %) Coondition for Reynolds Caviation
end
end

      % Error Criteria
PP=max (max(P));
err=(sum(sum(abs(P-Po))))/((sum(sum(abs(Po))))+eps);
end

[Px,Py]=gradient (P,dx,dy);

      % Load Calculation:
W1=dy*trapz(P);
W=dx*trapz(W1);
Wavg= W/L^2;          %)

      % Coefficient of Friction
f=v*u*(d/b+(1-d)/(a+b))/Wavg; %) Friction Coefficient

      % Leakage (Poiseuille)
Q=pi*(r0+r1)/(12*v)*dp/(r1-r0)*(sqrt(d)*(b)^3+(1-sqrt(d))*(a+b)^3)*25.4^3;

      % Leakage (Based on Hydrostatic boundary conditions)
Q_dp=pi*(r0+r1)/(12*v*L)*dx*trapz(h(1,:).^3.*Py(1,:))*25.4^3;

```

A.3 REYNOLDS EQUATION (in 2-D)

A.3.1 Continuity Equation

When density, ρ is assumed constant, conservation of mass can be written in terms of volumetric flow, Q . Velocities in the direction of x , y and z are given as U , V and W respectively. The following equations may be formulated from the fluid element, as shown in figure below.

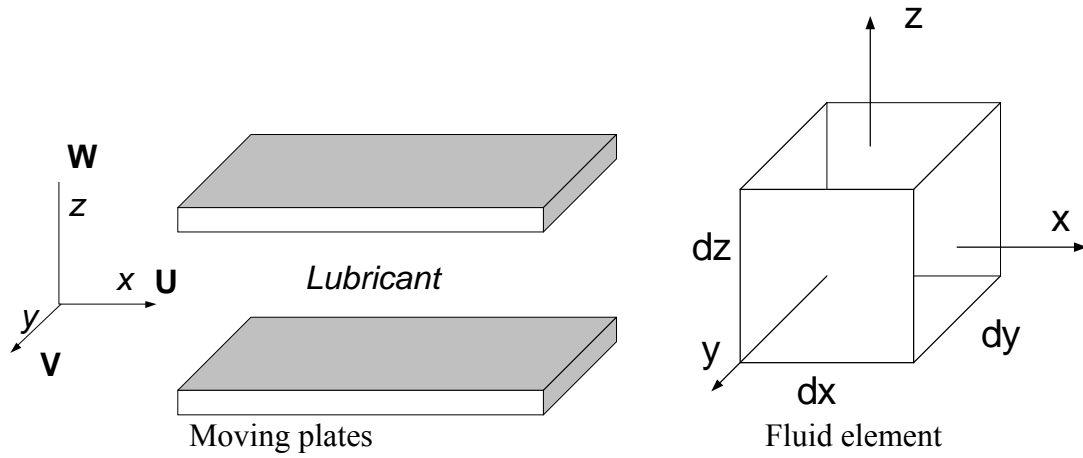


Figure A.1: Continuity of flow in a fluid element

$$[Q]_{+\frac{dx}{2}} + [Q]_{-\frac{dx}{2}} + [Q]_{+\frac{dy}{2}} + [Q]_{-\frac{dy}{2}} + \bar{Q} = 0 \quad (\text{a.1})$$

where $\bar{Q} = -\frac{\partial h(t)}{\partial t} dx dy$ is the rate of change of flow inside the fluid element

$[Q]_{-\frac{dx}{2}} = -\left[Q_x - \frac{\partial Q_x}{\partial x} \frac{dx}{2}\right]$ is the volumetric flow entering at the left face of the fluid element and

$[Q]_{+\frac{dx}{2}} = \left[Q_x + \frac{\partial Q_x}{\partial x} \frac{dx}{2}\right]$ is the volumetric flow exiting at the right face, in the x-direction.

With similar expressions in y-direction, equation (a.1), after substitution and simplification, can be rewritten as;

$$\frac{\partial Q_x}{\partial x} dx + \frac{\partial Q_y}{\partial y} dy + \bar{Q} = 0$$

Let $Q_x = q_x dy$, $Q_y = q_y dx$ and $\bar{Q} = -\frac{\partial h(t)}{\partial t} dx dy$. Substituting these in the above equation gives,

$$\frac{\partial q_x}{\partial x} + \frac{\partial q_y}{\partial y} - W = 0 \quad (\text{a.2})$$

where $W = \frac{\partial h}{\partial t}$

A.3.2 Force equilibrium on a fluid element

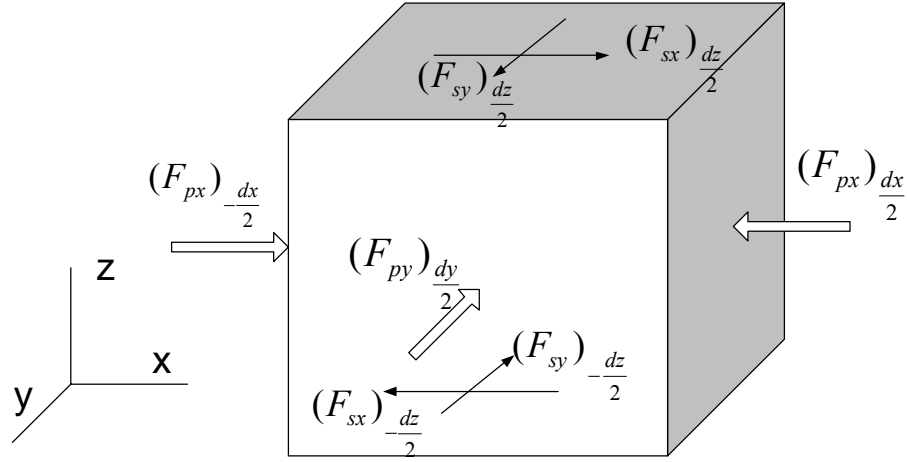


Figure A.2: Normal and shear forces on a fluid element

Neglecting body and inertia forces, as per Newton's second law,

$$\begin{aligned} \sum F_x &= \sum F_y = 0 \\ \sum F_x &= \left[F_{px} \right] \frac{dx}{2} + \left[F_{px} \right] \frac{dx}{2} + \left[F_{sx} \right] \frac{dz}{2} + \left[F_{sx} \right] \frac{dz}{2} \end{aligned} \quad (a.3)$$

where

$$\left[F_{px} \right] \frac{dx}{2} = - \left(P + \frac{\partial p}{\partial x} \frac{dx}{2} \right) dydz; \text{ (acting in the negative x-direction)}$$

$$\left[F_{px} \right] \frac{dx}{2} = \left(P - \frac{\partial p}{\partial x} \frac{dx}{2} \right) dydz$$

$$\left[F_{sx} \right] \frac{dz}{2} = \left(\tau_{zx} + \frac{\partial \tau_{zx}}{\partial z} \frac{dz}{2} \right) dx dy$$

$$\left[F_{sx} \right] \frac{dz}{2} = - \left(\tau_{zx} - \frac{\partial \tau_{zx}}{\partial z} \frac{dz}{2} \right) dx dy; \text{ (acting in the negative x-direction)}$$

Substituting these four equations in equation (a.3) and simplifying, we get:

$$- \frac{\partial p}{\partial x} + \frac{\partial \tau_{zx}}{\partial z} = 0 \quad (a.4)$$

Similarly, we get

$$- \frac{\partial p}{\partial y} + \frac{\partial \tau_{yz}}{\partial z} = 0$$

Since $\frac{\partial \tau_{zx}}{\partial z} = \mu \frac{\partial u}{\partial z}$ equation (a.4) can be written as;

$$- \frac{\partial p}{\partial x} + \frac{\partial}{\partial z} \left(\mu \frac{\partial u}{\partial z} \right) = 0 \quad (a.5)$$

Our assumption that pressure is a function of only x and y implies that $p = p(x, y)$ and $\frac{\partial p}{\partial z} = 0$.

Hence, integrating equation (a.5) with respect to z, we get;

$$\mu \frac{\partial u}{\partial z} = \frac{\partial p}{\partial x} z + C_1(x, y)$$

Integrating again, we get;

$$\mu u(z) = \frac{1}{2} \frac{\partial p}{\partial x} z^2 + C_1(x, y) + C_2 \quad (\text{a.6})$$

Applying boundary conditions for U, i.e. ;

@ $z=0, u=0$ and hence, $C_2=0$

@ $z=h, u=U$ and hence, $C_1 = -\frac{1}{2} \frac{\partial p}{\partial x} h + \mu \frac{U}{h}$

Substituting these values in (a.6), we get;

$$u(z) = -\frac{1}{2\mu} \frac{\partial p}{\partial x} \left(-z^2 + zh\right) + \frac{U}{h} z \quad (\text{a.7})$$

Differentiating this equation w. r. t. z, we get;

$$\frac{\partial u}{\partial z} = \frac{1}{\mu} \frac{\partial p}{\partial x} \left(z - \frac{h}{2}\right) + \frac{U}{h} \quad (\text{a.8})$$

We also know that

$$q_x = \int_0^h u(z) dz$$

Substituting (a.7) into this equation and integrating gives;

$$q_x = -\frac{1}{12\mu} \frac{\partial p}{\partial x} h^3 + \frac{Uh}{2}$$

Similarly, we have

$$q_y = -\frac{1}{12\mu} \frac{\partial p}{\partial y} h^3 + \frac{Vh}{2}$$

Substituting these results in equation (a.2), we get;

$$\frac{\partial}{\partial x} \left(-\frac{h^3}{12\mu} \frac{\partial p}{\partial x} + \frac{Uh}{2} \right) + \frac{\partial}{\partial y} \left(-\frac{h^3}{12\mu} \frac{\partial p}{\partial y} + \frac{Vh}{2} \right) - W = 0$$

For $V=W=0$, the above equation reduces to the well-known 2-D Reynolds equation;

$$\frac{\partial}{\partial x} \left(h^3 \frac{\partial p}{\partial x} \right) + \frac{\partial}{\partial y} \left(h^3 \frac{\partial p}{\partial y} \right) = 6\mu U \frac{\partial h}{\partial x}$$

References

1. Stephens, L., Siripuram, R., Hayden, M. and McCartt, B., “Deterministic Micro Asperities on Bearings and Seals Using a Modified LIGA Process”, *ASME/IGTI Conference*, Amsterdam, June 2002.
2. Ronen, A., Etsion, I, and Kilgerman, Y., “Friction-Reducing Surface-Texturing in Reciprocating Automotive Components”, *Tribology Transactions*, 44(3), 2001, pp.359-366.
3. Etsion, I., Kligerman, Y., and Halperin, G., “Analytical and Experimental Investigation of Laser-Textured Mechanical Seal Faces”, *Tribology Transactions*, 42(3), 1999, pp511-516.
4. Etsion, I., Halperin, G., and Greenberg, Y., “Increasing Mechanical Seals Life with Laser-Textured Seal Faces”, *Proc., 15th Int'l. Conference on Fluid Sealing*, BHR, 1997, pp3-11.
5. Hamilton, D. B., Walowit, J.A., & Allen, C.M., “A Theory of Lubrication by Microirregularities”, *Journal of Basic Engineering, Trans ASME*, Ser. D., March 1966, pp177-185.
6. Anno, J.N., Walowit, J.A., & Allen, C.M., “Microasperity Lubrication”, *Journal of Lubrication Technology, Trans ASME*, Ser. F, April 1968, pp351-355.
7. Anno, J.N., Walowit, J.A., & Allen, C. M., “Load Support and Leakage from Microasperity-Lubricated Face Seals”, *Journal of Lubrication Technology, Trans ASME*, Ser. F, October 1969, pp726-731.
8. Etsion, I., and Burstein, L., “A Model for Mechanical Seals with Regular Microsurface Structure”, *Tribology Transactions*, 39(3), 1996, pp677-683.
9. Holinski, R., “Fundamentals of Dry Friction and Some Practical Examples”, *Industrial Lubrication and Tribology*, Vol. 53, Number 2-2001, pp61-65, MCB University Press – ISSN 0036-8792.
10. Evans, C.J. and Bryan, J.B., “Structured, Textured or Engineered Surfaces”, *Annals of the CIRP*, Vol. 48; 2; 1999.
11. Young, L.A., and Lebeck, A.O., “The Design and Testing of a Wavy-Tilt-Dam Mechanical Face Seal”, *Lubrication Engineering*, 45(5), 1989, pp322-329.
12. Shellef, R.A., Johnson, R.P., “A Bi-Directional Gas Face Seal”, *Tribology Transactions*, 35(1), 1992, pp53-58.
13. Burstein, L., and Ingman, D., “Effects of Pore Ensemble Statistics on Load Support of Mechanical Seals with Pore-Covered Faces”, *ASME Journal of Tribology*, 121, October, 1999, pp927-932.
14. Wang, X., Kato, K., Adachi, K., and Aizawa, K., “The Effect of Laser Texturing of SiC Surface on the Critical Load for the Transition of Water Lubrication Mode from Hydrodynamic to Mixed”, *Tribology International*, 34, 2001, pp703-711.
15. Davies, M. G., “The Generation of Lift by Surface Roughness in a Radial Face Seal”, *International Conference on Fluid Sealing, British Hydromechanics Research Association*, Harlow, Essex, England, 1961.
16. Ishiwata, H., Hirabayashi, H., “Friction and Sealing Characteristics of Mechanical Seals”, *Proceedings of the International Conference of Fluid Sealing 1961* (British Hydromechanics Research Association, Cranfield, Bedford).

17. Fogg, A., "Fluid Film Lubrication of Parallel Thrust Surfaces", *Proceedings of the Journal of Mechanical Engineering*, Vol 155, 1946, pp49-60.
18. Salama, M.E., "The Effect of Macro-roughness on the Performance of Parallel Thrust Bearings", *Proceedings of the Institution of Mechanical Engineers*, vol.163, 1952, pp149-158.
19. Key, W.E., Salant, R.F., Payvar, P., Gopalakrishnan, S., Vaghasia, G., "Analysis of a Mechanical Seal with Deep Hydropads", *Tribology Transactions*, vol.32, 1989, pp481-489.
20. Salant, R.F., "Stiffness and Leakage in Spiral Groove Upstream Pumping Mechanical Seals", *Tribology Transactions*, vol.36, 1993, pp55-60.
21. Gardner, J.F., "Combined Hydrostatic and Hydrodynamic Principles Applied to Non-Contacting Face Seals", *Fourth International Conference on Fluid Sealing (ASLE)*, Philadelphia, 1969, pp88-98.
22. Moore, D.F., "Principles and Applications of Tribology", *Pergamon Press Inc.*, New York, 1975.
23. Ludema, K.C., "Friction, Wear and Lubrication", *CRC Press*, 1996.
24. Szeri, A.Z., "Fluid Film Lubrication, Theory and Design", *Cambridge University Press*, Cambridge, U.K., 1998.
25. Cameron, A., "Basic Lubrication Theory", *Oxford University Press*, 1969.
26. Burr, A.H., Cheatham, J.B., "Mechanical Analysis and Design", *Prentice Hall*, NJ, 1995.
27. Chapra, S.C. and Canale, R.P., "Numerical Methods for Engineers and Scientists", *McGraw Hill Inc.*, New York, 1988.
28. Jones, J.R., "Lubrication, Friction, and Wear", *NASA SP-8063*, 1971.
29. Stephens, L.S., "Advanced Machine Design Class Notes", ME-699, Spring 2001. *University of Kentucky*, Lexington.
30. Lebeck, A.O., "Principles and Design of Mechanical Seals", *John Wiley and Sons*.
31. Lay, D.C., "Linear Algebra and its applications", *Addison Wesley*, Reading, MA, 2000.
32. Kortikar, S.N., et. al., "Manufacturing of Micro-asperities on Thrust Surfaces using Ultraviolet Photolithography", *ASPE Conference*, Gainsville, Florida, Jan 2003.
33. Pinkus, O., and Sternlicht, B., "Theory of Hydrodynamic Lubrication", *McGraw Hill Inc.*, 1961.
34. Elrod, H.G., "A Cavitation Algorithm", *Transaction of the ASME*, vol.103, July 1981, pp350-354.
35. Basu, P., "Analysis of a Radial Groove Gas Face Seal", *Tribology Transactions*, vol.35, 1992, pp 11-20.
36. Findlay, J.A., "Cavitation in Mechanical Face Seals", *Transactions of the ASME*, April 1968, pp356-364.
37. Findlay, J.A., "Measurement of Leakage in Mechanical Face Seals", *Journal of Lubrication Technology*, October 1969, pp687-694.

Vita

DATE AND PLACE OF BIRTH

- b. 1962, Karimnagar, Andhra Pradesh, India.

EDUCATION

- Bachelor's Degree in Mechanical Engineering (B.E.), Osmania University, Hyderabad, AP, INDIA (1983).

WORK EXPERIENCE

- Worked as a research assistant at the University of Kentucky (2000-2002).
- Worked as an engineer at Hindustan Petroleum Corporation Limited in India (1983-1999).

PUBLICATIONS

- Stephens, L., Siripuram, R., Hayden, M. and McCartt, B., "Deterministic Micro Asperities on Bearings and Seals Using a Modified LIGA Process", *ASME/IGTI Conference*, Amsterdam, June 2002.
- Kortikar, S.N., Stephens, L.S., Hadinata, P.C., Siripuram, R.B., "Manufacturing of Micro-asperities on Thrust Surfaces Using Ultraviolet Photolithography", *ASPE Conference*, Gainesville, Florida, January 2003.